

NANOCRYSTALLINE PIEZORESISTIVE POLYSILICON FILM OBTAINED BY
ALUMINUM INDUCED CRYSTALLIZATION FOR
PRESSURE SENSING
APPLICATIONS

by

SURAJ KUMAR PATIL

Presented to the Faculty of the Graduate School of
The University of Texas at Arlington in Partial Fulfillment
of the Requirements
for the Degree of

DOCTOR OF PHILOSOPHY

THE UNIVERSITY OF TEXAS AT ARLINGTON

December 2010

Copyright © by Suraj Kumar Patil 2010

All Rights Reserved

ACKNOWLEDGEMENTS

I would like to sincerely thank my advisor Dr. Zeynep Çelik-Butler from the bottom of my heart for her constant encouragement and backing throughout my Ph.D work. Without her overall support and guidance my attainment of a Ph.D would have been a distant dream. Her thought process and work ethics greatly influenced me during my formative years as a researcher, and I am greatly indebted to her for that. During my research work she always made herself readily accessible for discussions and was very patient. I had a wonderful opportunity to learn a great deal from her.

I would also like to thank Dr. Donald P. Butler for taking his time and having several informative discussions whenever I was stuck with some problem during my research. I really admire his knowledge in various fields. His guidance was very crucial in my current work. Additionally, I would like to take this opportunity to thank my other committee members Dr. Seong Jin Koh, Dr. Yaowu Hao and Dr. Fuqiang Liu. Their graduate courses at UTA especially *Phase Transformations* and *Solid State Physics and Thermodynamics* have greatly helped me to better understand some of the most critical concepts behind the current research work.

I would like to thank my past group members especially Vinayak Shamanna, Dr. Yu Wang, Dr. Siva Devireddy, Dr. Mukti Rana, and Dr. Tanvir Morshed for all their help during the course of my research. I would also like to thank my current group members Late. Vijayakrishnan A, Rohit Kilaru, Clement Jacob, Gaviraj Nadvi, and Dr. Erkin Gonenli for all their help. I would like to thank ex-staff of NanoFAB Center Dr. Nasir Basit, Eduardo Maldonado, Dr. Fatima Amir, and current staff member Dennis Bueno for their help in training and in repairing of equipments. A special mention to members of Dr. Koh's group Dr. Visva Ray, Pradeep Bhadrachalam, Dr. Ramkumar Subramanian and Liang-Chieh Ma for their help in the cleanroom and other times.

I would like to thank all my other friends in UTA for a wonderful time. Finally, I would like to thank my parents and brother for their incessant love and care. This work is dedicated to my parents.

November 19, 2010

ABSTRACT

NANOCRYSTALLINE PIEZORESISTIVE POLYSILICON FILM OBTAINED BY ALUMINUM INDUCED CRYSTALLIZATION FOR PRESSURE SENSING APPLICATIONS

Suraj Kumar Patil, PhD

The University of Texas at Arlington, 2010

Supervising Professor: Zeynep Çelik-Butler

The overall objective of our research was to integrate various sensors on to a single flexible substrate for multi-sensory information gathering. Additional capabilities could be incorporated towards the realization of '*smart skin*' for simultaneous and real time sensing of various mechanical, biological and chemical stimuli. Recent research venues are dictated by the trend of shifting from conventional silicon (Si) substrates to lower weight, low profile, structurally robust and lower cost flexible substrates. These flexible substrates easily conform to non-planar objects, could be batch fabricated at lower cost and enable multilayer construction. This would eventually evolve into seamless assimilation of sensors for various stimuli onto a single flexible substrate for plethora of applications in consumer electronics, robotics, medical prosthetics, surgical instrumentation, structural health monitoring and industrial diagnostics to name a few.

Pressure sensors currently find numerous applications in the field of automobiles (airbag deployment, tire pressure monitoring systems (TPMS), fuel systems etc.), smart cell phones (microphones, touch screens etc.) and various biomedical devices. The pressure

sensor selection criterion is strictly based on the requirements of specific pressure range and resolution. It is also dependent on the environment (temperature, medium etc.) the sensor would be deployed in. Some commonly used pressure sensor designs include absolute, gauge and differential/tactile types. All of the above sensors could either employ piezoresistive, piezoelectric, capacitive or optical readout methodologies for sensing applied pressure.

Piezoresistor-based, differential pressure sensor designs are most commonly used because of their (i) versatility, (ii) relatively simple construction, (iii) linear responsivity with applied pressure, (iv) long-term stability, and (v) maturity of the technology. There has been a growing interest in the development of various sensors that often require deployment of planar micro to nano-scale sized sensors on flexible substrates such as polyimide, polyethylene terephthalate (PET), polyethylene naphthalate (PEN), and stainless steel (SS).

Current work describes the use of piezoresistive-based differential pressure sensors on a flexible polyimide substrate. Our design uses a suspended diaphragm with piezoresistive sensing based on a Wheatstone bridge circuitry. The measurement resolution can be effectively controlled by the diaphragm geometry and size, whereas the diaphragm thickness and the micromachined gap under the diaphragm determine the range. The surface micromachining used here would also facilitate stacking of different sensors (viz. infrared, pressure, chemical, biological) on a single flexible substrate, conforming to the underlying object. For our current application, the aim was to measure low pressure changes ranging from few tens of a pascal (Pa) to few tens of kPa.

Fabrication processes on a wide variety of flexible substrates are dictated by their lower glass transition temperatures (T_g). This critical restriction more often requires low temperature film deposition and device fabrication techniques in order to use them as substrates. Polysilicon being CMOS compatible is used both as a mechanical and an electrical material in many sensor designs, as it makes the integration of the sensor with read-out circuitry readily feasible. Since polysilicon also exhibits a relatively high piezoresistive gauge factor, it is

also preferred over its metal counterparts. However, conventional polysilicon deposition techniques typically require high temperatures, which are incompatible with polyimide substrates. The work presented here is a low temperature method for obtaining polysilicon piezoresistive thin films using aluminum-induced crystallization (AIC) of amorphous silicon (a-Si) film. A very important step involving the curing of polyimide PI-2611 was successfully developed to withstand AIC annealing temperatures in excess of 500 °C for couple of hours. This facilitated the use of multilayer PI-2611 as our substrate and sacrificial material. We have obtained nanocrystalline polysilicon films with average grain sizes of 45-55 nm at temperatures ranging from 400 °C to 500 °C with annealing time of 60 minutes, and an average grain size of 50 nm at 500 °C for a shorter annealing time of 30 minutes. An additional advantage of this process is that the polysilicon films are simultaneously doped p-type, thereby eliminating any additional doping step. By varying the aluminum (Al) and a-Si layer thicknesses, annealing temperature and duration, the growth of polysilicon grains ranging from few tens of nanometers to tens of microns in diameter can be effectively obtained.

Additionally, exploring the piezoresistive properties of the above mentioned low temperature nanocrystalline polysilicon thin films deposited on polyimide substrate for pressure sensing applications was another vital aspect of this research. In order to achieve this firstly, arrays of MEMS based pressure sensors were successfully fabricated on polyimide substrate. Secondly, an atomic force microscope (AFM) in contact mode with a modified probe-tip was used to apply differential pressures. Low pressures (lesser than atmospheric pressure) were successfully applied onto the sensors using AFM. Thirdly, higher pressures (greater than 4 times the atmospheric pressure) were applied onto the sensors by using a load-cell coupled with a nano-positioner. The design of the pressure sensor characterization set-ups and subsequent experimental procedures are described in this work. Finally, experimental characterization of fabricated MEMS pressure sensors on polyimide substrate employing

polysilicon resistors obtained by AIC were performed to measure their pressure sensitivity responses.

TABLE OF CONTENTS

ACKNOWLEDGEMENTS	iii
ABSTRACT	v
LIST OF ILLUSTRATIONS.....	xiii
LIST OF TABLES	xvii
LIST OF SYMBOLS	xviii
Chapter	Page
1. INTRODUCTION.....	1
1.1 Flexible Electronics - Evolution	1
1.1.1 Flexible Substrates - Properties	2
1.1.2 Various Flexible Substrates	2
1.1.3 Sensors on Flexible Substrates	4
1.1.4 Pressure Sensors - Applications	4
1.1.5 Pressure Sensing Mechanisms	5
1.2 Piezoresistance	6
1.2.1 Various Piezoresistive Materials	7
1.2.2 Piezoresistance in Semiconductors	8
1.2.3 Advantages of Using Polysilicon	13
1.2.4 Polysilicon Thin Film as Piezoresistive Material	13
1.3 Piezoresistive Pressure Sensor Design Specs and Material Selection Criteria - Overview.....	14
1.4 Summary.....	16
2. POLYSILICON THIN FILM DEPOSITION	18
2.1 Applications and Advantages	18
2.2 Conventional Polysilicon Deposition Methods	19

2.2.1 Physical Vapor Deposition (PVD)	19
2.2.2 Atmospheric Pressure Chemical Vapor Deposition (APCVD)	21
2.2.3 Low Pressure Chemical Vapor Deposition (LPCVD)	22
2.2.4 Plasma Enhanced Chemical Vapor Deposition (PECVD)	23
2.2.5 Hot-Wire Chemical Vapor Deposition (HWCVD)	24
2.2.6 Laser Ablation (LA)	24
2.3 Crystallization of Amorphous Silicon (a-Si)	25
2.3.1 Solid Phase Crystallization (SPC)	25
2.3.2 Excimer Laser Crystallization (ELC)	26
2.4 Aluminum Induced Crystallization (AIC)	26
2.4.1 Mechanism	30
2.4.2 Crystallization Process	33
2.4.3 Silicon Grain Growth	35
2.4.4 Factors Affecting AIC	35
2.5 Aluminum-Induced Crystallization Process Development and Analysis	37
2.5.1 Scanning Electron Microscopy	38
2.5.2 Energy Dispersive Spectroscopy	40
2.5.3 X-Ray Diffraction	40
2.5.4 Sheet Resistance Measurements	44
2.6 Summary	45
3. FABRICATION OF PRESSURE SENSORS ON FLEXIBLE SUBSTRATES	47
3.1 Pressure Sensor Fabrication Steps	48
3.1.1 Preparation of Flexible Substrate	48
3.1.2 Preparation of Polyimide as Sacrificial Layer	49

3.1.3 Diaphragm Layer Deposition and Etching	50
3.2 Polysilicon Piezoresistors by AIC.....	51
3.2.1 Polysilicon Film by AIC.....	52
3.2.2 Aluminum Interconnects.....	54
3.2.3 Sacrificial Polyimide Layer Removal by Ashing	55
3.3 Summary.....	59
4. CHARACTERIZATION AND ANALYSIS	60
4.1 Introduction.....	60
4.1.1 Various Low Pressure Application Methods and Challenges	61
4.1.2 Atomic Force Microscope (AFM) as Pressure Sensor Characterization Tool	63
4.1.3 Load-Cell as Pressure Sensor Characterization Tool.....	63
4.2 AFM Based Characterization Set-up	64
4.2.1 Effective Spring Constant (k_{eff})	64
4.2.2 Contact Force.....	66
4.2.3 Contact Area and Tip-Sample Interactions	67
4.2.4 Experimental Procedure.....	68
4.2.5 AIC Polysilicon Film Characterization	70
4.2.5.1 Experiment #1 - Gauge Factor.....	70
4.2.5.2 Experiment #2 - Modes of Operation	75
4.2.5.3 Experiment #3 - Anneal Temperatures	76
4.2.6 Advantages of using AFM and Challenges.....	79
4.3 Pressure Sensor Characterization	80
4.3.1 VI Characteristics	81
4.3.2 Characterization using AFM.....	82
4.3.3 Characterization using Load-Cell.....	84

4.3.4 Non-Linearity	86
4.3.5 Hysteresis.....	87
4.4 Summary.....	87
5. SUMMARY	89
6. CONCLUSIONS	96
APPENDIX	
A. GRAIN SIZE ESTIMATION FROM XRD MEASUREMENTS.....	97
B. PRESSURE SENSOR DESIGNS.....	101
C. PROCEDURE FOR PRESSURE SENSOR CHARACTERIZATION USING ATOMIC FORCE MICROSCOPE (DEVELOPED BY: SURAJ KUMAR PATIL)	106
D. RESISTANCE CALCULATIONS FROM WHEATSTONE BRIDGE.....	110
E. PROCEDURE FOR PRESSURE SENSOR CHARACTERIZATION USING LOAD-CELL (DEVELOPED BY: SURAJ KUMAR PATIL)	113
REFERENCES	118
BIOGRAPHICAL INFORMATION	127

LIST OF ILLUSTRATIONS

Figure	Page
1.1 Change in resistance of a metal block when acted by uniaxial stress σ_x along X-axis	7
1.2 CoventorWare TM model of (a) pressure sensor build-up, (b) suspended Si ₃ N ₄ diaphragm, and (c) equivalent half-Wheatstone bridge circuit.	15
2.1 Phase-diagram for Al-Si binary system	27
2.2 Ni/Si compound forming (CF) system describing metal induced crystallization process (a) initially, (b) during transformation.....	28
2.3 Metal induced crystallization process for Al/Si binary system (SE)	29
2.4 SEM image of the final polysilicon film obtained by AIC at 500 °C, for 90 minutes and subsequently etched in Al-etch	39
2.5 SEM image of (a) as-deposited a-Si film sectioned with FIB, (b) polysilicon film annealed at 400 °C and subsequently etched in Al-etch solution.....	39
2.6 XRD plots for (a) as-deposited a-Si film and the films annealed at 500 °C, (b) for 90 minutes, (c) for 45 minutes and (d) for 30 minutes in forming gas and subsequently etched in Al-etch	41
2.7 XRD plots for polysilicon film obtained by annealing at 500 °C, 475 °C, 450 °C and 400 °C for 60 minutes in forming gas and subsequently etched in Al-etch	42
2.8 Measured sheet resistance for polysilicon films of thickness ~ 0.5 µm obtained (a) by annealing at 500 °C for anneal times of 30, 45 and 60 minutes, and (b) with constant anneal time of 60 minutes and for anneal temperatures of 400 °C, 450 °C, 475 °C and 500 °C.....	44
3.1 Cross-sectional schematic showing step by step fabrication process flow for pressure sensor	49
3.2 Schematic showing step by step fabrication process flow for pressure sensor.....	51
3.3 SEM images after patterning and RIE of Si ₃ N ₄ diaphragm layer	51

3.4 Schematic diagram after deposition of Al and a-Si and subsequent lift-off to obtain piezoresistors	53
3.5 Optical microscope images of the pressure sensors corresponding to schematic of Figure 3.4	53
3.6 Schematic cross-sectional diagram after AIC of a-Si and subsequent etching in Al-etch solution to obtain polysilicon piezoresistors	54
3.7 Schematic diagram after formation of Al metal interconnects.....	55
3.8 Optical microscope images of pressure sensor corresponding to the schematic of Figure 3.7	55
3.9 Schematic view after etching of sacrificial polyimide layer by ashing in O ₂ plasma to suspend the Si ₃ N ₄ diaphragm layer	56
3.10 SEM images of pressure sensors with polysilicon piezoresistors covered with a thin Au film before ashing.	57
3.11 Optical microscope images of pressure sensors after 15 hours and 25 hours of ashing in O ₂ plasma	57
3.12 SEM images of the pressure sensor with sacrificial polyimide being ashed away..	58
3.13 Array of piezoresistive pressure sensors of different diaphragm dimensions and piezoresistors shapes..	59
4.1 Piezoresistor dimensions.	61
4.2 Pressure sensor characterization set-up (a) load-cell, and (b) XYZ stage.	63
4.3 Modified AFM probe-tip with (a) spherical particle of radius 25 μm attached to the rectangular cantilever, (b) area of contact estimation between the probe-tip and the diaphragm surface	65
4.4 Force plot for AFM in contact mode. The slope gives S _v (nm/V)	67
4.5 SEM image of Device#1 with 80 x 80 μm^2 Si ₃ N ₄ diaphragm, showing active resistors and passive resistors connected in a half-Wheatstone bridge configuration.....	68
4.6 (a) Device packaged and placed under the AFM probe-tip for pressure characterization, (b) Schematic of the I-V setup for 4-wire resistance measurements for resistor R ₂ across device contact pads B and C corresponding to Figure 1.2 (a)	69
4.7 IV Characteristics for active resistor R2 of Device #1 and Device #2 using Agilent 4155C for no applied pressure.....	71

4.8 Plot of % $[\Delta R/R_0]$ versus applied pressure, P (kPa) for non-continuous engagement case for Device#1 and Device#2	72
4.9 Different regions of the piezoresistor used for average strain computation.....	73
4.10 COVENTOR™ simulation showing Mises stress distribution for (a) Device#1 and (b) Device#2 when a uniform pressure of 70 kPa is applied at the center of each diaphragm	74
4.11 Plot comparing % $[\Delta R/R_0]$ versus applied pressure, P (kPa) for Device#1 for continuous engagement and non-continuous case	75
4.12 SEM image of pressure sensor Device#3 with Si ₃ N ₄ diaphragm size of 80 x 80 μm^2	77
4.13 IV characteristics for the R ₂ polysilicon piezoresistor obtained by annealing for 90 minutes at 400 °C and 500 °C.....	77
4.14 % $[\Delta R/R]$ with applied pressure, P (kPa) for R ₂ polysilicon films obtained by AIC with annealing temperatures of 400 and 500 °C, compared to the passive resistor R ₃	78
4.15 (a) An array of pressure sensors with AIC polysilicon resistors on suspended 80 x 80 μm^2 Si ₃ N ₄ diaphragms, (b) a half-Wheatstone bridge electrical circuit for measuring ΔV_{OUT} versus P	80
4.16 Individually wire-bonded pressure sensor device on a package ready to be characterized using AFM and load-cell set-up.....	81
4.17 VI characteristics for R ₁ , R ₂ , R ₃ and R ₄ for the device in Figure 4.15	82
4.18 Schematic of pressure sensor characterization set-up using AFM.....	83
4.19 Pressure sensor response ΔV_{OUT} versus P using AFM	84
4.20 Schematic of pressure sensor characterization set-up using load-cell.....	85
4.21 Pressure sensor response ΔV_{OUT} versus P using load-cell	86
A.1 <111> plot from θ -2 θ measurements for polysilicon film obtained by AIC of a-Si at 475 °C and 60 minutes	98
B.1 Mask layout for various pressure sensors	102
B.2 Pressure sensors TM#4, TM#5 and R#5 corresponding to Device#1, Device#2 and Device#3 respectively (Not to scale)	103
B.3 Various pressure sensors structures with different diaphragm shapes, sizes and piezoresistors (Not to scale)	104
B.4 Piezoresistors with different shapes and sizes (Not to scale)	105

D.1 Wheatstone bridge circuit and corresponding equivalent circuit for measurement of individual resistance R_4	111
E.1 Load-cell pressure sensor characterization set-up	114

LIST OF TABLES

Table	Page
1.1 Piezoresistive Coefficients for <100> Si- wafer ($\times 10^{-11} \text{ Pa}^{-1}$) with $N_a, N_d < 10^{18} \text{ cm}^{-3}$	12
2.1 Metal/Si systems with their corresponding T_E and T_C	28
2.2 Crystallization, surface and interface energies for Al/Si system	32
2.3 EDS profile for samples at polysilicon obtained at 400 °C, 90 minutes	40
2.4 XRD Analysis of polysilicon films obtained at different annealing temperatures and times with grain size ranges (* Gaussian Fit)	43
4.1 Comparison of S_v values for Device#1 for continuous and non-continuous tip engagement	76
5.1 Comparisons of some recent pressure sensor designs with present work	94
A.1 Gaussian fit parameters obtained from ORIGIN™ software for <111> peak using θ -2 θ measurements for polysilicon film obtained by AIC of a-Si at 475 °C, 60 minutes	99
A.2 Lorentzian fit parameters obtained from ORIGIN™ software for <111> peak using θ -2 θ measurements for polysilicon film obtained by AIC of a-Si at 475 °C, 60 minutes	100
E.1 Various components and their resolutions for load-cell set-up	116

LIST OF SYMBOLS

T_g	Glass Transition Temperature
GF	Gauge Factor
R	Resistance
R, R_0	Initial Resistance
R_f	Final Resistance
ΔR	Change in Resistance ($R_f - R_0$)
ϵ	Strain
ϵ_{avg}	Average Strain
ϵ_{xx}	Strain along X-direction
ϵ_{yy}	Strain along Y-direction
N_a	Acceptor Impurity Concentration
N_d	Donor Impurity Concentration
ρ	Resistivity
ρ_g	Grain Resistivity
ρ_b	Barrier Resistivity
$\Delta\rho$	Change in Resistivity
K	Wave Number
eV	Electron Volt
e	Unit Charge
p_{hh}	Heavy-Hole Concentration
p_{lh}	Light-Hole Concentration
τ_{hh}	Heavy-Hole Relaxation Time
τ_{lh}	Light-Hole Relaxation Time
m_{hh}	Effective Mass of Heavy-Hole

m_{lh}	Effective Mass of Light-Hole
E	Electric Field
i	Current
π	Piezoresistive Coefficient
π_l	Piezoresistive Coefficient along Longitudinal Direction
π_t	Piezoresistive Coefficient along Transverse Direction
π_g	Piezoresistive coefficient for Grain
π_b	Piezoresistive coefficient for Grain Boundary
L_c	Polysilicon Grain Size
w	Barrier Width inside Polysilicon Grain
σ	Stress
σ_l	Stress in Longitudinal Direction
σ_t	Stress in Transverse Direction
ν	Poisson's ratio
S'_{jk}	Compliance Coefficient
δ_{jk}	Kronecker Delta Function
K_{IC}	Fracture Toughness
ΔV_{OUT0}	Output Voltage at No Applied Pressure
ΔV_{OUT}	Differential Sensor Output Voltage (After applied pressure)
P	Pressure
T_E	Eutectic Temperature

T_C	Crystallization Temperature
$\{A\}$	Denotes Amorphous State of Material
$\langle A \rangle$	Denotes Crystalline State of Material
d_{Si}	Thickness of $\{Si\}$ As -Deposited
d_{Al}	Thickness of $\langle Al \rangle$ As-Deposited
$d^{crit.}$	Critical Thickness
G	Gibbs Energy
H	Enthalpy
ΔH	Excess Molar Enthalpy
S	Entropy
ΔS	Excess Molar Entropy
$\Delta G_{\langle Si \rangle - \{Si\}}$	Gibbs energy difference per unit volume between $\langle Si \rangle$ and $\{Si\}$
$\Delta G_{\langle Al \rangle}$	Gibbs Energy Difference per unit volume between annealed $\langle Al \rangle$ and as deposited $\langle Al \rangle$ layer
γ^S	Surface Energy of Phase
γ^{int}	Interface Energy
μ	Chemical Potential
n_A	Number of Moles of Material A
R_G	Gas Constant
a	Activity
N_A	Avogadro's Number
x	Depth
t	Time
C	Concentration

D	Diffusion Coefficient
L_D	Diffusion Length
J	Flux Density
v_g	Growth Velocity
K	Grain Shape Factor ($K=0.9$)
θ_B	Bragg's Diffraction Angle
$\lambda_{Cu-K\alpha}$	Wavelength of Cu-K α X-ray source
F_c	Contact Force
A_c	Probe contact Area with the diaphragm
f_{r0}	Resonant Frequency of the rectangular cantilever with no particle attached
f_{r1}	Resonant Frequency of the rectangular cantilever with particle attached
M	Mass of the cantilever
k	Spring Constant
k_{eff}	Effective Spring Constant
S_v	Deflection Sensitivity of the probe-tip
V_t	Applied Trigger Voltage
d	Displacement of the diaphragm
R_{Loaded}	Resistance of the piezoresistor after loading (experiencing strain)

CHAPTER 1

INTRODUCTION

1.1 Flexible Electronics - Evolution

The development and usage of flexible electronics dates back to 1960s when arrays of solar cell were first fabricated by thinning down the silicon wafer followed by bonding them to a plastic substrate for flexibility [1]. During the course of next decade, the maturity and feasibility of depositing hydrogenated amorphous silicon thin films (a-Si:H) at low temperatures enabled several researchers to use thin flexible stainless steel [2], and organic polymers [3,4] as substrates for solar cell applications. 1980s saw the arrival of thin film transistors (TFT) on wide variety of flexible substrates such as mylar, polyethylene, and anodized aluminum (Al) wrapping foil [5] which were used for active matrix displays and solar cells. Constant et al. [6] demonstrated a-Si:H TFT based electronic circuit on flexible polyimide substrate in 1994. In 1996, a-Si:H TFTs were demonstrated on stainless steel substrates [7] followed by polycrystalline silicon (polysilicon) TFTs on flexible plastic substrates [8,9] in 1997. The current decade saw an explosion in development of flexible substrate electronic products. Applications involving novel thin film structures (eg: cadmium indium gallium selenide (CIGS), cadmium telluride (CdTe), low temperature a-Si:H and polysilicon etc.) for solar cells, liquid crystal displays (LCDs) and lately organic light emitting diodes (OLEDs) are being extensively used in consumer electronics industry today [10]. Currently, with the maturing of fabrication process technology various sensors and actuators than never before have been employed in radio-frequency identification tags (RFID), smart-phones, automobiles, human health monitoring, industrial robotics, and homeland security to name a few.

The development of any flexible electronic system can be broadly divided into *post – process integration* and *direct integration*. In post-process integration case, the semiconductor devices are first fabricated on conventional silicon (Si) or any rigid substrate and later *bonded*

onto the flexible substrates. Alternatively, in direct integration case as the name suggests the semiconductor devices are directly fabricated on flexible substrates which has opened numerous new research venues for process integration.

1.1.1 Flexible Substrates – Properties

Some important properties governing the flexible substrate selection are as follows [10, 11]:

1. **Thermal** – A mismatch between device thin film and flexible substrate film would result in unwanted stress leading to possible cracks and de-lamination of thin film layers during thermal cycling or deposition steps. Thus, the coefficient of thermal expansions (CTEs) of adjacently deposited films must be carefully matched. A tolerable mismatch can be achieved if $|\Delta\text{CTE} \cdot \Delta T| \leq 0.3\%$ where ΔCTE is the difference in CTEs of the substrate and device films and ΔT is the maximum temperature difference experienced by the structure during processing.
2. **Chemical** – An ideal substrate film should be inert or less reactive to some commonly used processing chemicals such as acids and bases during cleaning, etching and photolithography steps.
3. **Mechanical** - The substrate film should be able to retain its desired mechanical properties such as elastic modulus, thickness etc. during various device processing steps.
4. **Surface Roughness** - This property of the flexible substrate film should be in spec to achieve good planarization and lithography definitions.

1.1.2 Various Flexible Substrates

Some commonly used flexible substrate materials are as follows:

1. **Glass** – Thinned glass of thickness ranging from few tens of μm to hundreds of μm are used as flexible substrates [12]. These are used in applications requiring very high optical transmittance properties and from medium to high temperature processing steps ($\sim 600^\circ\text{C}$). Thin glass substrates are additionally inert to water, air and oxygen

environment and are chemically resistant to most acids and bases. Their CTEs are also comparable to that of silicon (Si) so there is very small thermal mismatch and they show good adhesion properties with other deposited thin films. However, one drawback is that they are hard to handle as they are fragile.

2. **Plastics** – Some common materials that fall into this category are polyethylene terephthalate (PET), polyethylene naphthalate (PEN), polycarbonate (PC), polyethersulphone (PES), polyimide (PI), polyarylates (PA), polycyclic olefin (PCO) [10]. These substrates are inexpensive, light weight and allow roll-to-roll process. However, considerable care must be taken while trying to match their glass-transition temperatures (T_g) with maximum process temperatures to be experienced, in order to reduce thermal mismatch. Another advantage is that depending on specific requirements, plastics can be effectively altered to achieve different thicknesses and transmittance properties. However, most of these substrates react to strong acids and bases and often require passivation layer to protect them. They also require an extra buffer layer for enhanced adhesion purposes. Additionally, the usage of plastic substrates is limited to relatively lower processing temperature ranging from 100 °C - 400 °C.

3. **Metal Foils** – Stainless steel (SS) foils of thickness $\sim 125 \mu\text{m}$ are commonly used as flexible substrates. These substrates have the advantage of handling very high processing temperatures in excess of 1000 °C. However, they have relatively higher surface roughness when compared to glass and plastics substrates, so they often require surface planarization step. They also require surface coatings of thin silicon nitride (SiN_x) or silicon oxide (SiO_2) films as passivation layers to provide barrier against some process chemicals. Adhesion is also poorer when compared with glass substrate but metal substrates are mechanically very robust so can be employed in a rugged environments [13, 14].

1.1.3 Sensors on Flexible Substrates

The overall objective of our research was to integrate various sensors on to a single flexible substrate for multi-sensory information gathering. Additional capabilities could be incorporated towards the realization of '*smart skin*' for simultaneous and real time sensing of various mechanical, biological and chemical stimuli. Our first step towards this approach was to design and fabricate a surface micromachined Yttrium Barium Copper Oxide (YBaCuO) infrared sensors on a flexible polyimide substrate [15]. Our next step was to integrate a pressure sensor with the infrared sensor (microbolometer) [16].

Some important advantages of using flexible substrates over conventional silicon (Si) wafer are as follows [17]:

1. The fabrication processes can be made compatible with current CMOS process technology thereby enabling heterogeneous integration of novel semiconductor devices.
2. The fabricated structures can easily conform to base objects and can have lower form factors.
3. It can facilitate multilayer applications for stacking thereby saving on the real estate.
4. Lighter weight and lower cost than conventional Si substrates.

Targeted applications areas of these fabricated sensors are in the fields of consumer and aeronautical electronics, medical prosthetics, industrial robotics and wearable health monitoring systems.

1.1.4 Pressure Sensors - Applications

Pressure sensors currently find numerous applications in the field of automobiles (airbag deployment, tire pressure monitoring systems (TPMS), fuel systems etc.), smart cell phones (microphones, touch screens etc.) and various biomedical devices. The pressure sensor selection criterion is strictly based on requirements of specific pressure range and resolution and is greatly dependent on the environment (temperature, medium etc.) the sensor would be deployed. Some commonly used pressure sensor designs include absolute, gauge

and differential/tactile types. At the heart of every pressure sensor there is a suspended structure such as a diaphragm which deflects or moves as pressure is applied on it. These sensors could employ capacitive, piezoelectric, piezoresistive, optical or resonance readout methodologies for sensing applied pressure.

1.1.5 Pressure Sensing Mechanisms

Sensing pressure using capacitive transduction is the simplest form of pressure sensor structure. A movable suspended diaphragm forms a parallel plate capacitor with a fixed metal plate beneath it with a small separation between them. As the pressure is applied, the diaphragm displaces thereby changing the capacitance between the plates. This relative change in capacitance can be measured and is proportional to the applied pressure. Such a read-out has the advantage of being highly sensitive to low pressures and has lower power consumption and lower temperature output dependence compared to its piezoelectric and piezoresistive counterparts. However, it has the disadvantage of requiring a very stringent calibration standard and signal loss due to parasitic capacitances [18,19].

Piezoelectric-based pressure transduction scheme consists of a suspended diaphragm made up of a piezoelectric material. When pressure is applied, the deflection of the diaphragm brings about changes in internal stresses of the piezoelectric material film thereby generating electric output voltage. The advantage of this scheme is that the sensor shows a very good linearity with applied pressure. However, it has relatively lower sensitivity when compared to the capacitive readout [20,21,22]. It also has the disadvantage of a low dc response due to charge leakage of the piezoelectric material. Moreover, fabrication issues specifically related to obtaining the right texture and stoichiometric composition can be a problem during deposition of the piezoelectric thin films on a wide variety of substrates. The deflection of the diaphragm due to the applied pressure can also be measured using optics based on Mach Zender [23] and Fabry Perot [24] interferometers. This read-out mechanism has the advantage of being accurate with a good linearity. However, its sensitivity is susceptible to variations in temperature and often requires very precise alignment and calibration of the optical setup [25].

Resonance frequency transduction mechanism, on the other hand, is based on measuring the change in resonant frequency of the suspended diaphragm or beam with applied pressure. This type of mechanism has the advantage of being more immune to noise compared to its piezoresistive and capacitive counterparts and it displays very good pressure sensitivity and low temperature dependence [26].

In piezoresistive-based pressure sensing, resistors are embedded into or in regions near the suspended diaphragm. As the diaphragm deflects due to applied pressure, the internal stresses bring about a change in strain in the resistors which in turn varies their resistances. This changes the measured output voltage. Some advantages of using this kind of transduction are ready integration with other CMOS read-out circuitry which greatly eases the fabrication process. Additionally, due to its low output impedance its better immune to other noise interferences [27, 28]. It also has an added advantage of being effective for both absolute and tactile pressure sensing applications. However, as any variations in operating temperature affect the piezoresistors due to TCR effects it has a disadvantage of its sensitivity being highly temperature dependent.

1.2 Piezoresistance

Piezoresistance property was first discovered by Lord Kelvin in 1856. It is a material property where the bulk resistivity of the material is affected when acted upon by mechanical stresses. In case of metals, this change in resistivity is only due to the change in length of the sensing element during deformation. To better illustrate the point, we consider a rectangular block of metal with resistivity, ρ and initial length, area and resistance as l_0 , A_0 and R , respectively. When a uniaxial stress σ_x is applied on it as shown in Figure 1.1, the stress brings about a relative change in its resistance, ΔR due to change in its area, ΔA and change in its length, Δl . Thus we can now define gauge factor, GF [29] of the material given by Eq. 1.1 as follows

$$GF = \frac{\Delta R}{R \varepsilon_{avg}} \quad (1.1)$$

where ε_{avg} is the average strain experienced by the test structure. Usually for metals, $GF \approx 2$.

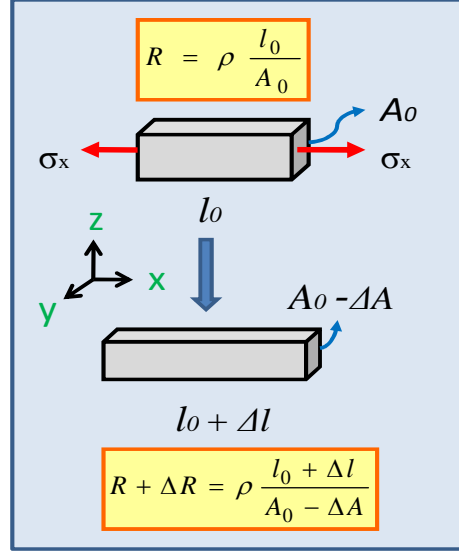


Figure 1.1 Change in resistance of a metal block when acted by uniaxial stress σ_x along X-axis.

1.2.1 Various Piezoresistive Materials

Various metals, alloys, semiconductors and certain ceramics have been successfully employed for piezoresistive sensing. For example platinum (Pt) resistors have been placed in series with Indium Tin Oxide (ITO) as a piezoresistive material, achieving GF of 20.9, designed for elevated temperature sensors operating up to 1560 °C [30]. Thin gold (Au) films of thickness 40 nm have also been employed as piezoresistors with a GF of 2 - 4 on a SU-8 based mechanical sensor [31]. In addition, thick film resistors comprising of ruthenium oxide (RuO_2) powder and glass frit in paste form have been used as a piezoresistive sensing material and GF of 2-30 have been achieved [32].

For nickel-silver ($\text{Ni}_x\text{-Ag}_{1-x}$) thin films, a GF of 2.2-2.4 was demonstrated when $x = 0.35$ [33]. Nichrome ($\text{Ni:Cr} = 80:20$) thin film resistors embedded on polyimide showed a lower GF of

1.3 [34]. GF of 4-5 have been realized by tantalum nitride - copper (TaN-Cu) nanocomposite thin film resistors with a near zero temperature coefficient of resistance [35].

Strained $\text{Si}_{0.9}\text{Ge}_{0.1}$ resistors of thickness of 200 nm deposited by Molecular-Beam Epitaxy (MBE) showed 30% increase in their piezoresistive coefficient π_{66} compared to π_{44} of silicon for the doping concentration of $N_A = 10^{18} \text{ cm}^{-3}$, thus making it more sensitive than silicon thin film piezoresistors [36]. Single crystal diamond shows a very high GF of 2000 but for most applications it is prohibitively expensive. Alternatively, polycrystalline diamond thin films deposited by chemical vapor deposition showed GF of 100. In a particular case, 0.5 μm thick boron doped polycrystalline diamond resistors were implemented to achieve a GF of 22 [37]. Thin germanium (Ge) films were evaporated on Kapton as a substrate at low temperatures to achieve a GF of 33-42 and as high as 100 [38]. Amorphous carbon (a-C) layers sputter-deposited at low temperatures ($< 150^\circ\text{C}$) have also been used as strain gauges with a GF between 36-46 [39]. Giant piezoresistance effect has been observed in p-type Si nanowires grown along $\langle 111 \rangle$ and $\langle 110 \rangle$ directions compared to bulk p-type Si enabling its use in nano-electromechanical systems on flexible substrates [40]. Since semiconductors tend to display an order of magnitude higher piezoresistivity than their metal and ceramics counterparts, they are the most widely used and studied piezoresistive materials.

1.2.2 Piezoresistance in Semiconductors

The piezoresistive effect in semiconductor materials is due to the deformation of energy bands as result of applied stress. Piezoresistivity in semiconductors (esp. Ge, Si) was first discovered by Smith in 1954 [41]. The valence band structure of Si generally comprises of heavy hole, light hole and spin-orbit split-off bands. From the energy band – wave number (K) diagram of Si the heavy hole and light hole bands are degenerate at $K = 0$ with an empty split-off band slightly shifted downwards by few hundredth of eV. When a uniaxial stress is applied to Si, its cubic symmetry is changed due to the tensile or compressive action thereby removing the degeneracy at $K = 0$. This further leads to splitting of the heavy and light hole bands into a pair of degenerate doublets. The spin-orbit split-off band gets populated with holes thereby resulting

in the net change in the hole concentration with applied stress. The energy levels associated with split-off bands are different from the heavy and light hole bands due to the difference in their effective masses. Additionally, the relaxation times for both heavy and light holes vary with applied stress as it directly depends on their corresponding hole band energies. Thus, the resistivity for a p-type Si, $\rho_{p\text{-type}}$ is given [42] as:

$$\rho_{p\text{-type}} = \frac{1 / e^2}{\left(\frac{\tau_{hh} p_{hh}}{m_{hh}} + \frac{\tau_{lh} p_{lh}}{m_{lh}} \right)} \quad (1.2)$$

where e is the unit charge, p_i is the hole concentration, m_i is the effective mass, τ is the relaxation time in band i , heavy hole (hh) or light hole (lh) band. The deformed bands change the effective mass and concentration of the charge carriers (hole), hence modifying resistivity.

The resistivity ρ can be further represented in a matrix form by considering a 3-D anisotropic crystal. The electrical field vector, E is related to current vector, i as [29]:

$$\begin{bmatrix} E_1 \\ E_2 \\ E_3 \end{bmatrix} = \begin{bmatrix} \rho_1 & \rho_6 & \rho_5 \\ \rho_6 & \rho_2 & \rho_4 \\ \rho_5 & \rho_4 & \rho_3 \end{bmatrix} \bullet \begin{bmatrix} i_1 \\ i_2 \\ i_3 \end{bmatrix} \quad (1.3)$$

Since Si has a cubic crystal structure, for $\langle 100 \rangle$ crystal orientation and unstressed case, the resistivity's along the three axes X, Y and Z directions can be represented as $\rho_1 = \rho_2 = \rho_3 = \rho$ and cross resistivities as $\rho_4 = \rho_5 = \rho_6 = 0$ (for an isotropic conductor). For the stressed case, the change in resistivities is given by [29]:

$$\begin{bmatrix} \rho_1 \\ \rho_2 \\ \rho_3 \\ \rho_4 \\ \rho_5 \\ \rho_6 \end{bmatrix} = \begin{bmatrix} \rho \\ \rho \\ \rho \\ 0 \\ 0 \\ 0 \end{bmatrix} + \begin{bmatrix} \Delta \rho_1 \\ \Delta \rho_2 \\ \Delta \rho_3 \\ \Delta \rho_4 \\ \Delta \rho_5 \\ \Delta \rho_6 \end{bmatrix} \quad (1.4)$$

Eq. 1.4 can further be decomposed into three normal stress components σ_1 , σ_2 , σ_3 and shear stress components τ_1 , τ_2 , τ_3 . Therefore, the fractional change in resistivity due to applied

stress is given by $(\Delta\rho_i / \rho) = \pi_{ij}\sigma_{ij}$, where π is the piezoresistive coefficient. Due to symmetry property of the cubic crystal we obtain [29]:

$$\frac{1}{\rho} \begin{bmatrix} \Delta\rho_1 \\ \Delta\rho_2 \\ \Delta\rho_3 \\ \Delta\rho_4 \\ \Delta\rho_5 \\ \Delta\rho_6 \end{bmatrix} = \begin{bmatrix} \pi_{11} & \pi_{12} & \pi_{12} & 0 & 0 & 0 \\ \pi_{12} & \pi_{11} & \pi_{12} & 0 & 0 & 0 \\ \pi_{12} & \pi_{12} & \pi_{11} & 0 & 0 & 0 \\ 0 & 0 & 0 & \pi_{44} & 0 & 0 \\ 0 & 0 & 0 & 0 & \pi_{44} & 0 \\ 0 & 0 & 0 & 0 & 0 & \pi_{44} \end{bmatrix} \bullet \begin{bmatrix} \sigma_1 \\ \sigma_2 \\ \sigma_3 \\ \tau_1 \\ \tau_2 \\ \tau_3 \end{bmatrix} \quad (1.5)$$

For randomly oriented poly-crystals, $\pi_{44} = \pi_{11} - \pi_{12}$. Therefore, from Eqs. 1.3, 1.4 and 1.5 we get the electric field components for a cubic lattice under stress given as [29]:

$$\begin{aligned} E_1 &= \rho i_1 + \rho\pi_{11}\sigma_1 i_1 + \rho\pi_{12}(\sigma_2 + \sigma_3)i_1 + \rho\pi_{44}(i_2\tau_3 + i_3\tau_2) \\ E_2 &= \rho i_2 + \rho\pi_{11}\sigma_2 i_2 + \rho\pi_{12}(\sigma_1 + \sigma_3)i_2 + \rho\pi_{44}(i_1\tau_3 + i_3\tau_1) \\ E_3 &= \rho i_3 + \rho\pi_{11}\sigma_3 i_3 + \rho\pi_{12}(\sigma_1 + \sigma_2)i_3 + \rho\pi_{44}(i_1\tau_2 + i_2\tau_1) \end{aligned} \quad (1.6)$$

In Eq. 1.6 [29], the first term is due to the contribution of the unstressed conduction. The second term represents the piezoresistance effect due to change in potential in the direction of current flow and the third term is due to the piezoresistive behavior of stressed semiconductor lattice [29]. All the piezoresistance properties of silicon aligned to the <100> axes of the silicon crystal can be calculated from π_{11} , π_{12} and π_{44} . In order to calculate the stresses and electric field for an arbitrary Cartesian system, the <100> axes can be transformed into the given coordinate system. If k_1 , k_2 and k_3 are the unity vectors of the <100> axes system, and a_1 , a_2 and a_3 are the unit vectors of the new axes system. We can express the relation between the two systems as given by [42]:

$$\begin{aligned} k_1 &= l_1 a_1 + l_2 a_2 + l_3 a_3 \\ k_2 &= m_1 a_1 + m_2 a_2 + m_3 a_3 \\ k_3 &= n_1 a_1 + n_2 a_2 + n_3 a_3 \end{aligned} \quad (1.7)$$

If (l_1, l_2, l_3) , (m_1, m_2, m_3) and (n_1, n_2, n_3) are the coordinates in the new system. A vector (x, y, z) referred to crystal axes is then transformed into a vector (x^*, y^*, z^*) in the new system using [29,42,45]:

$$\begin{bmatrix} x^* \\ y^* \\ z^* \end{bmatrix} = \begin{bmatrix} l_1 & m_1 & n_1 \\ l_2 & m_2 & n_2 \\ l_3 & m_3 & n_3 \end{bmatrix} \bullet \begin{bmatrix} x \\ y \\ z \end{bmatrix} \quad (1.8)$$

For an isotropic material, GF is given by [42]:

$$GF = 1 + 2\nu + \frac{\Delta\rho}{\rho\varepsilon} \quad (1.9)$$

where ν is the Poisson's ratio, and ε is the strain. For anisotropic homogeneous material, on the other hand, GF can be expressed as [42]:

$$GF = 1 - \sum_j \frac{S_{kj}}{S_{kk}}(1 - \delta_{kj}) + \frac{\pi_d}{S_{kk}} \quad (1.10)$$

Here S_{kj} is the compliance coefficient and π_d is the piezoresistance coefficients and δ_{kj} is the Kronecker delta function. For longitudinal strain $k=1$ and $d=l$ and for transverse strain $k=2$ and $d=t$. The compliance and piezoresistive coefficients are calculated using Eq. 1.8 [42] as

$$\begin{aligned} S_{kj} &= S_{12} + (S_{11} - S_{12} - \frac{1}{2}S_{44})(l_k^2 l_j^2 + m_k^2 m_j^2 + n_k^2 n_j^2) \\ S_{kk} &= S_{11} - (2S_{11} - 2S_{12} - S_{44})(l_k^2 m_k^2 + l_k^2 n_k^2 + m_k^2 n_k^2) \\ \pi_l &= \pi_{11} + 2(\pi_{44} + \pi_{12} - \pi_{11})(l_1^2 m_1^2 + l_1^2 n_1^2 + m_1^2 n_1^2) \\ \pi_t &= \pi_{12} + (\pi_{11} - \pi_{12} - \pi_{44})(l_1^2 l_2^2 + m_1^2 m_2^2 + n_1^2 n_2^2) \end{aligned} \quad (1.11)$$

The piezoresistive coefficients obtained experimentally have found to be largest for π_{11} ($\approx -102 \times 10^{-11} \text{ Pa}^{-1}$) in n-type silicon and π_{44} ($\approx -138 \times 10^{-11} \text{ Pa}^{-1}$) in p-type Si [36,42,43]. The

relative change in resistance of a material as a function of applied stress can then be calculated from the longitudinal (σ_l) and transverse (σ_t) stresses with respect to the current flow [43]:

$$\frac{\Delta R}{R} = \frac{\Delta \rho}{\rho} = \sigma_l \pi_l + \sigma_t \pi_t \quad (1.12)$$

where π_l is the longitudinal and π_t is the transverse piezoresistance coefficients. For (100) plane Si –wafer and for <110> direction oriented piezoresistor, the piezoresistance coefficients reduce to [43]:

$$\begin{aligned} \pi_l &= \frac{1}{2}(\pi_{11} + \pi_{12} + \pi_{44}) \\ \pi_t &= \frac{1}{2}(\pi_{11} + \pi_{12} - \pi_{44}) \end{aligned} \quad (1.13)$$

Table 1.1 gives the piezoresistivity coefficients at room temperature for a <100> Si wafer and doping level less than 10^{18} cm^{-3} [43]. We can hence approximate the relative change in resistance for p-type and n-type Si piezoresistors directly from Eq. 1.12. Mono-crystalline Si exhibits GF of around 100 and its piezoresistance can be explained by the means of many-valley model [29].

Table 1.1 Piezoresistive Coefficients for <100> Si- wafer ($\times 10^{-11} \text{ Pa}^{-1}$) with $N_a, N_d < 10^{18} \text{ cm}^{-3}$ [41,43]

Type	π_{11}	π_{12}	π_{44}	π_l	π_t
p-Si	+6.6	-1.1	+138.1	72	-66
n-Si	-102.2	+53.4	13.6	-31	-18

Considering an example of n-type Si, piezoresistance can be accounted due to the deformation of conduction band minima under applied stress. If n-type Si is acted upon by a tensile stress along [100] direction, the conduction band energies along [100] and $[\bar{1}00]$ directions increase and the electrons move to bands having lowest energies i.e. along [010], $[0\bar{1}0]$, [001] and $[00\bar{1}]$ valleys. Therefore, the change in piezoresistive coefficients and the electron mobilities along the longitudinal and transverse direction of the ellipsoids in k-space

due to applied axial stress brings about a change (in this particular case reduction) in the resistivity of the semiconductor material [25, 29]. It was observed that for both n-type and p-type Si, the value of piezoresistive coefficients decreases with increasing temperature and doping concentrations [41]. However, Richter et al. [36] found that the π_l and π_t values for p-type doped Si were actually lower by 30% than the values reported in Table 1.1 from [41,43]. Nevertheless, Si still exhibits considerably higher piezoresistivity than its metal counterparts.

1.2.3 Advantages of Using Polysilicon

The use of mono-crystalline Si is hindered by its inability to be deposited on wide variety of insulating substrates. Its deposition process is expensive, time consuming and requires high temperature processing steps (especially during doping and dopant activation). Hence, p-type or n-type polycrystalline silicon is actively employed as structural, electrical and piezoresistive material in lieu of single crystalline Si. The deposition temperatures for polysilicon is around 550-600 °C using low-pressure chemical vapor deposition (LPCVD) and around 350-450 °C using plasma-enhanced chemical vapor deposition (PECVD). Alternatively RF sputtering in presence of hydrogen (H₂) and hot-wire chemical vapor deposition (HWCVD) are also used to obtain polycrystalline silicon. The piezoresistivity coefficients for polysilicon are approximated at 70 % of mono-crystalline Si [25].

1.2.4 Polysilicon Thin Film as Piezoresistive Material

Polysilicon is one of the most widely used piezoresistive thin film materials. In particular, its relatively high gauge factor (GF) value compared to metals, combined with its CMOS process compatibility and availability at a reasonable cost makes it very attractive as a piezoresistive material for force and pressure sensing applications. For polysilicon, as the grains are randomly oriented, the piezoresistance coefficient is an average over all orientations. The gauge factor which is defined by Eq. 1.10 is about a factor of 5-10 times smaller than in single crystal Si. However, polysilicon tends to exhibit lower TCR values compared to crystalline Si for increased doping [43].

Since polysilicon film is constituted of grains of various sizes separated by grain boundaries, P. J. French et al. [42] gave the GF for a single polysilicon grain as follows:

$$GF = 1 - \sum \frac{S'_{kj}}{S'_{kk}} (1 - \delta_{kj}) + \frac{\rho_g \times \pi_g}{\rho_g + (2w + \delta) \rho_b / [L_C - (2w + \delta)]} + \frac{\rho_b \times \pi_b}{\rho_b + [L_C - (2w + \delta)] \rho_g / (2w + \delta)} \quad (1.14)$$

Here, S'_{kj} and S'_{kk} are compliance coefficients for Si obtained from its elastic coefficients; δ is the boundary thickness (nm); δ_{kj} is the Kronecker delta function; ρ_g and ρ_b are grain and barrier resistivities, respectively; π_g and π_b are grain and boundary piezoresistive coefficients; L_C is the grain size and w is the barrier width created due to depletion of carriers inside the grain. Eq. 1.13 thus shows that GF is higher for large grain sizes. Hence the sensitivity of the polysilicon film to applied strain increases with increase in its grain size. The relative change in piezoresistor's resistance with applied pressure is given by Eq. 1.11. Our target was to obtain polysilicon thin films with grain sizes of approximately 1 μm , which would correspond to GF of 50 assumed and used during the model simulation. However, fabrication of piezoresistor-based pressure sensors on flexible polyimide substrates is limited by T_g of the specific polyimide used (in our case PI-2611), which sets the value for the maximum deposition and/or annealing temperature of the piezoresistive thin film (in this case polysilicon) such that the integrity of flexible polyimide substrate is maintained.

1.3 Piezoresistive Pressure Sensor Design Specs and Material Selection Criteria – Overview

The pressure sensor consisted of a suspended silicon nitride (Si_3N_4) diaphragm design as shown in Figure 1.2 [44] based on ref. [16]. The sensor was designed to sense lower pressures typically in the range of 0-50 kPa. We chose piezoresistive pressure sensor design for obvious reasons as described earlier in Section 1.1.5, which meant the output of the sensor could be easily read, was simple to construct, readily feasible to be integrated with CMOS read-out circuitry (for signal amplification, temperature compensation, voltage offset compensation), was very robust and provided linear response to applied pressure. One important advantage of

using piezoresistive tactile sensors over its piezoelectric counterparts was that it is possible to obtain a d.c response. Si_3N_4 was chosen as a surface micromachined diaphragm material since it has the strongest covalent bond properties next to silicon carbide (SiC) [45]. Due to its superior heat resistance, strength, and hardness it is commonly used as high temperature structural ceramic. It also has excellent wear and corrosion resistance with flexural strength of around 850 MPa at room-temperature and fracture toughness (K_{IC}) between $5\text{-}8 \text{ MPa} \cdot (\text{m})^{1/2}$ [45]. Si_3N_4 film has lower coefficient of linear thermal expansion (CTE) of $3.4 \text{ ppm}/^\circ\text{C}$ with good adhesion to the polyimide layer [45]. Polysilicon was the choice for the piezoresistive material as it exhibited a relatively high gauge factor and exhibited reduced hysteresis and creep when compared to metal thin films [25]. Additionally, polysilicon being a CMOS compatible material would facilitate the matching of piezoresistors with other active and passive elements of read-out circuitry. It has a CTE value of $3 \text{ ppm}/^\circ\text{C}$ which matches with Si_3N_4 [43].

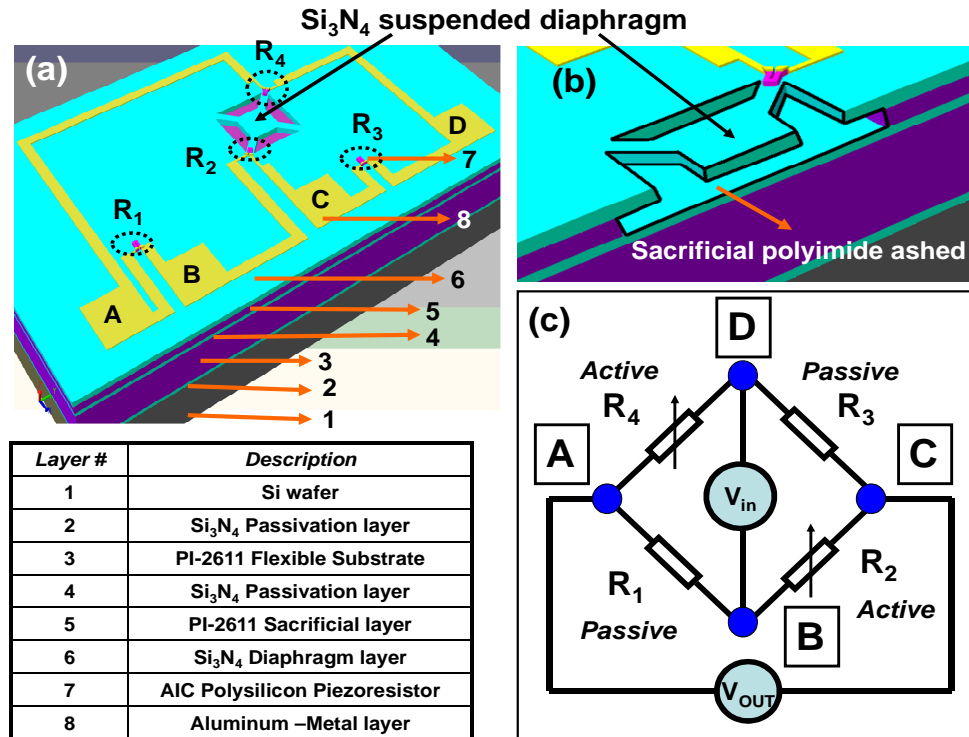


Figure 1.2 CoventorWare™ model of (a) pressure sensor build-up, (b) suspended Si_3N_4 diaphragm, and (c) equivalent half-Wheatstone bridge circuit [44].

PI-2611 (HD Microsystems, Inc., New Jersey, USA) was chosen as a substrate and a sacrificial layer material because of its low-stress properties, compatible CTE of 3 ppm /°C, tensile strength of 350 MPa and a relatively high glass transition temperature (T_g) of 360 °C. The polyimide is bio-compatible enabling various bio-medical applications.

From Figure 1.2 (a) and (c), resistors R_1 and R_3 are passive or reference resistors used for biasing, whereas resistors R_2 and R_4 lie on the bridge arms known as active resistors in half-Wheatstone bridge configuration. The sensor output, V_{OUT0} for certain input bias voltage; V_{in} is given as:

$$V_{OUT0} = \left(\frac{R_4}{R_4 + R_1} - \frac{R_3}{R_3 + R_2} \right) \times V_{in} \quad (1.15)$$

Ideally, when pressure is applied on the diaphragm, only the resistances R_2 and R_4 which lie on the bridge arms get stretched with the pressure, thereby resulting in a change in their resistances, $\Delta R_2 = \Delta R_4 = \Delta R$, due to mechanical stretch and also due to band deformation and the corresponding sensor output voltage is given as:

$$V_{OUT0} + \Delta V_{OUT} = \left(\frac{R_4 + \Delta R}{R_4 + R_1 + \Delta R} - \frac{R_3}{R_3 + R_2 + \Delta R} \right) \times V_{in} \quad (1.16)$$

Here ΔV_{OUT} is the differential sensor output for corresponding applied pressure, P.

1.4 Summary

The advantages of fabricating various MEMS sensors on flexible substrates (polyimide) over conventional Si wafers have been advocated. Different pressure sensing transduction mechanisms are described. Piezoresistive properties of several materials have been given with special emphasis on the theory of piezoresistance with respect to semiconductors. Since main thrust of this dissertation was to develop and employ low-temperature polysilicon films as a piezoresistive sensing element on flexible substrates for pressure sensing applications, the working principle of half-Wheatstone bridge based piezoresistive pressure sensors is described

along with some important mechanical, electrical and piezoresistive properties of the polysilicon films.

CHAPTER 2

POLYSILICON THIN FILM DEPOSITION

2.1 Applications and Advantages

Polysilicon is the most versatile semiconductor material used in plethora of applications such as a gate material in complementary metal-oxide transistor (CMOS) devices; as interconnects in integrated circuits, and more lately in through-silicon vias (TSV). Recently, polysilicon is found to be a very good alternative to mono-crystalline Si in fabrication of low-cost solar cells on glass and plastic substrates. Additionally, polysilicon is an attractive material of choice in the fabrication of TFT's for liquid crystal displays (LCD), and as CMOS based image sensors used in charge-coupled display (CCD) cameras. Additionally, polysilicon has wide spread applications as both a structural and an electrical layer in micro-electromechanical systems (MEMS) - based fabrication of sensors and actuators.

Since the current research work emphasis was on low-temperature deposited polysilicon thin films as piezoresistive material for MEMS-based tactile pressure sensing applications, our selection criteria for using polysilicon film were based on its following advantages [25, 29, 42, 43]:

1. Mechanically similar properties to that of mono-crystalline Si and forms a stable oxide.
2. Good step coverage.
3. Low TCR values compared to mono-crystalline Si.
4. High melting point.
5. Excellent masking material for micro-fabrication as it is resistant with hydrofluoric acid (HF) commonly used for releasing the final MEMS based structures by etching the sacrificial silicon oxide (SiO_2) layer underneath.

6. Excellent electrical properties which could be effectively changed by selectively doping polysilicon (n-type or p-type) to obtain desired electron and hole mobilities which can also be controlled by varying polysilicon grain sizes.
7. GF of polysilicon is higher than metals making it a very attractive material in fabrication of MEMS based strain gauges and pressure sensors.
8. Polysilicon films tend to display reduced hysteresis and creep than metal thin films when used as strain gauges.
9. Its ability of translating the applied strain effectively into change in its film resistance (piezoresistive property) is an important factor for its selection as strain, force and pressure sensing devices.
10. Finally, its fabrication compatibility with conventional CMOS processes and its ability to be deposited at low-temperatures on a variety of substrates enables numerous applications.

2.2 Conventional Polysilicon Deposition Methods

2.2.1 Physical Vapor Deposition (PVD)

Before 1970s, polysilicon thin films with approximate thicknesses less than 0.1 μm were deposited using sputtering, evaporation and molecular beam epitaxy (MBE) at deposition temperatures ranging from room temperatures (RT) to 600 $^{\circ}\text{C}$. This method has the advantage of being a relatively simple low temperature deposition process. However, it does have problems involving non-uniform step coverage, film thickness variations, ion-damage and incorporation of unwanted impurities in the final polysilicon thin films [43, 47].

In the last decade (1995 - 2005), polysilicon thin films obtained by sputtering have gained much research and commercial interests particularly in the field of MEMS and solar cells on plastics. Both direct current (dc) and radio frequency (rf) based sputter deposition techniques have been effectively used to obtain polysilicon thin films.

Pulsed (100 kHz) dc magnetron sputtering was used by P. Reinig et al. to deposit <100> oriented polysilicon thin films at the substrate temperature of 300 $^{\circ}\text{C}$ - 450 $^{\circ}\text{C}$ in argon (Ar)

environment. The maximum polysilicon grain size obtained was 60 nm [48]. K. Xu et al. deposited polysilicon films at a substrate temperature of 200 °C on thin gold-coated glass and at 140 °C on polyethyleneterephthalate (PET) substrate using dc magnetron sputtering with 5% hydrogen (H₂), 10% krypton (Kr), and 85% Ar gas mixture. The polysilicon grain sizes obtained were (95±5) nm [49, 50].

Alternatively, radio frequency (rf) sputtering at 13.56 MHz was used to deposit polysilicon silicon films with grain sizes of 20 nm at the substrate temperature of 100 °C with Ar and with partial pressure of less than 40 % of H₂ gas. However, the final polysilicon film showed incorporation of hydrogen, which would result in considerable deterioration in film electrical properties with time [51]. In another case, polysilicon was also deposited at elevated substrate temperatures of 470 °C- 490 °C using ultra-high vacuum (UHV) sputtering system with rf (100 MHz) and sputter gas mixture of Ar and H₂. Grain sizes of approximately 40 nm were obtained in this case [52]. Lowering the substrate temperature to 300 °C during deposition gave polysilicon films with grain sizes of 26 nm.

Low temperature deposition of polysilicon was also achieved by a bias-sputtering process in presence of Ar gas, in addition to H₂ and mix of water vapor (H₂O), carbon monoxide (CO) and carbon dioxide (CO₂) gases with individual partial pressures of 1.0×10^{-8} Torr or less, and at substrate temperatures ranging from 400 °C-700 °C. The average grain size obtained in this case was 80 nm at the deposition temperature of 550 °C [53]. Y. H. Jang et al. [54] described the deposition of polysilicon at 300 °C using a very high frequency (182.5 MHz) sputtering by capacitively-coupled parallel plate electrodes using Ar and H₂ sputter gases. The polysilicon grain sizes obtained in this case was 20 nm. J. Joo described the use of a 2 MHz ionized magnetron sputtering based on inductively-coupled plasma (ICP) source for polysilicon deposition. In this case Ar:H₂ flow in ratio of 10:6 was used as sputter gas to obtain polysilicon films at a substrate temperature of 250 °C with grain sizes of 50-70 nm [55].

We tried depositing polysilicon films using conventional rf sputtering from a highly p-doped Si target in an Ar environment at the sputtering pressure of 2.8 mTorr, and rf power of

150 watts (W). Since the presence of polyimide restrained us from heating the substrate to elevated temperatures during the film deposition our preliminary XRD characterization on the deposited films displayed amorphous texture. Furthermore, electrical measurements carried out on the above films indicated a very high sheet resistance with resistance values in the range of few tens of M Ω . This deterred us from further pursuing rf sputter as a viable direct deposition method for obtaining polysilicon films.

2.2.2 Atmospheric Pressure Chemical Vapor Deposition (APCVD)

CVD gained immense popularity between the years 1970-1976. It is the process whereby constituents of the vapor phase react chemically to form a solid product (thin or thick film) at the substrate surface maintained at elevated temperatures. CVD processes are basically surface-catalyzed reactions where in the reactants from the precursor gases are adsorbed on the heated substrate surface due to heterogeneous reactions occurring between the reactants and the surface. This is followed by surface diffusion and subsequent ad-atoms nucleation occurring at the surface forming thin film. Since this process is carried out at pressures ranging from 10 - 101 kPa, it is called APCVD [43]. It is thus a preferred method of deposition for obtaining thick epitaxial films.

Typically for polysilicon film deposition, substrate temperatures ranging from 850 °C-1300 °C are generally used with silane (SiH₄), di-chloro silane (SiH₂Cl₂), tri-chloro silane (SiHCl₃) and silicon tetra-chloride (SiCl₄) as precursor gases [43, 47, 56, 57]. Each of these precursor gases has a different decomposition temperature and results in different film deposition rates. Among them SiH₄ has the lowest dis-association temperature in the range of 630 °C - 850 °C and a high deposition rate. Grain sizes ranging from 1- 50 μ m are reported and the polysilicon films obtained by APCVD are generally used in solar-cells and CMOS devices [47]. In-situ doping of polysilicon film can be carried out by introducing the desired doping (n-type or p-type) gas during the deposition process. APCVD has the disadvantage of producing very high thickness variations in final films leading to poor step coverage and particle contamination [43]. Additionally, since APCVD is a mass-transport controlled process, batch

processing of wafers cannot be effectively done because more amounts (mass) of reactant species (from decomposition of precursor gas) is generally required with increased wafer surface area. APCVD deposition of polysilicon thin films could not be used for our work because of the obvious reasons stated earlier and most importantly as the deposition temperatures exceeded the T_g of the polyimide substrate being used.

2.2.3 Low Pressure Chemical Vapor Deposition (LPCVD)

LPCVD of polysilicon film layers was introduced in 1976. As the name suggests the deposition is carried out at low pressures ($\sim 1 - 100$ Pa). The use of low pressure facilitated lower decomposition temperatures of SiH_4 , SiH_2Cl_2 and SiHCl_3 precursor gases. Thus enabling relatively lower deposition temperatures needed when compared to APCVD. Typically, temperatures ranging from $550^\circ\text{C} - 850^\circ\text{C}$ are used for polysilicon film deposition [43, 58, 59, 60, 61, 62]. The polysilicon grain sizes obtained in this case are between $0.05\ \mu\text{m}$ to $1\ \mu\text{m}$ [47]. In situ doping of polysilicon film can also be carried out by introducing different doping gases during the deposition step. Alternatively, post deposition polysilicon film doping can be performed through ion-implantation or diffusion, to achieve specific resistivity. However, annealing at high temperatures is carried out to activate the dopant, stabilize the polycrystalline material by increasing the grain size and removing lattice damage during doping [61]. LPCVD has been the most widely used deposition technique for polysilicon films with numerous applications in solar-cells, CMOS devices and MEMS technology. Since LPCVD process is surface–reaction controlled, batch processing of wafers is possible thus making it an inexpensive deposition method with an excellent yield. Moreover, the films obtained are of high quality and stoichiometric. Other important film properties related to microstructure, stress, density, optical etc. measured experimentally are in accordance with theoretical estimated values, and are very well controlled. Additionally, polysilicon films obtained by LPCVD have excellent uniformity, conformity and purity [47] as no diluting gases are used unlike APCVD. However, due to thermal budget restrictions of the flexible substrate material and the possibility

of contamination of the furnace tube from volatile species due to vaporization of organics from the polyimide substrate, LPCVD could not be used for our research work.

2.2.4 Plasma Enhanced Chemical Vapor Deposition (PECVD)

In this method, polysilicon and hydrogenated amorphous Si (a-Si:H) thin films are obtained at deposition temperatures between 150 °C – 350 °C with typical pressures between 200 – 700 Pa [43, 63, 64]. RF glow discharges producing weakly ionized plasmas are commonly used in PECVD. The electrons present in the plasma collide with and provide the necessary energy to disassociate the precursor gas into reactant species, thereby, reducing the deposition temperatures considerably when compared to APCVD and LPCVD. SiH₄ and Si₂H₆ are commonly used as precursor gases. Simultaneously, like other deposition methods, doping gases can be introduced in the reaction chamber to obtain either n-type or p-type doped polysilicon or amorphous Si films. Polysilicon grain sizes in the range of 0.05 µm to 0.1 µm are typically obtained [47]. The PECVD-obtained thin films are uniform and have good step coverage. Typically, these polysilicon thin films are used in applications involving solar cells and TFTs. However, one serious drawback of using PECVD-obtained polysilicon films is that they have hydrogen incorporated in them (> 10 % at.). This results in degassing of hydrogen from the film surface at elevated temperatures creating bubbles which lead to formation of pin-holes and other macroscopic defects [47]. The resultant films require an additional silicon dehydrogenation step and re-crystallization at higher temperatures to increase their grain sizes. In-situ doping of the hydrogenated amorphous silicon (a-Si:H) is required to obtain conductive layers, followed by annealing at temperatures around 750 °C for electrical activation [65]. These conditions restricted us from using PECVD for deposition of polysilicon on flexible substrates. Another alternative was to use a rf-biased, inductively coupled PECVD tubular system for depositing polysilicon films with grain sizes up to 80 nm without any post deposition heat treatment and at temperatures as low as 77 °C [66]. The above tubular PECVD configuration though an attractive option for low-temperature deposition of polysilicon, was however, custom

designed by authors in [66]. This approach was beyond the scope of our present research as it required an extensive equipment design procedure and expensive modifications.

Electron Cyclotron Resonance CVD (ECRCVD) is an extension of the PECVD system that uses cyclotron to produce a highly dense rf plasma. This enables even lower polysilicon deposition temperatures between 100 °C- 400 °C with high deposition rates between 5-50 $\mu\text{m}/\text{min}$. The grain sizes typically vary between 0.05 μm - 0.1 μm . The deposition pressures are very low between 0.1 -1 Pa. Polysilicon films obtained by ECRCVD show relatively less (< 2 - 4 % at.) [43] incorporation of hydrogen when compared to films obtained from PECVD. High densities of plasma are attained by a very high magnetic field coupled with microwave power generator which increases the cost of operation considerably [43, 47, 67].

2.2.5 Hot-Wire Chemical Vapor Deposition (HWCVD)

This method uses pyrolysis reaction between SiH_4 / Si_2H_6 and H_2 on a filament catalyzer which is heated to 1300 °C - 2000 °C and is located several centimeters away from the substrate at pressures around 10 Pa. The substrate surface experiences temperatures between 150 °C- 450 °C [47, 68, 69]. The hot filament decomposes the precursor gases into its constituent species and the rest of the nucleation and film growth steps are similar to that in LPCVD or PECVD. HWCVD even though being a low temperature polysilicon deposition process has a very high deposition rate of 50 - 200 $\mu\text{m}/\text{min}$ when compared with APCVD, LPCVD, and PECVD (1-20 $\mu\text{m}/\text{min}$). Polysilicon grain sizes ranging from 0.05 μm to 1 μm are typically obtained [47]. These films find applications in solar-cell fabrication and for epitaxial growth. HWCVD is a simple and low cost procedure with provisions for in-situ doping and large area depositions.

2.2.6 Laser Ablation (LA)

Another method of low-temperature deposition of polysilicon is by LA [70, 71]. It involves a laser incident on the target to physically remove part of the material from target and to transfer onto the substrate placed centimeters away. We performed preliminary tests using pulsed laser deposition system (PLD) with Class IV excimer KrF laser, and highly p-type doped Si wafer as

target. Our trials with LA resulted in relatively low grade polycrystalline Si films. Other disadvantages included the final film surface being riddled with clusters of Si islands, making its surface profile highly non-uniform which made patterning of structures (in our case piezoresistors) quite difficult [72]. Furthermore, the polysilicon deposition area was limited to the center of the substrate as it was highly dependent on the shape of the laser plume incident on it. IV measurements on the piezoresistors comprising of LA polysilicon typically indicated the resistance values in the range of few tens of megaohms (M Ω), which made the use of our LA polysilicon film not an attractive option. More information regarding laser ablation of polysilicon, process and characterization can be found in [72].

2.3 Crystallization of Amorphous Silicon (a-Si)

Crystallization of a-Si provides a post film deposition alternative for obtaining polysilicon films on flexible plastics and a wide variety of unconventional substrates. It also enhances the quality of deposited polysilicon film with respect to changes in its grain size, electrical activation of dopants, elimination of lattice and surface defects and stress in the layers. Thin films of a-Si can be deposited either by sputtering, evaporation or PECVD and then be re-crystallized either by a high temperature process (~ 1000 $^{\circ}\text{C}$) and low temperature process (≤ 600 $^{\circ}\text{C}$).

High temperature re-crystallization process of a-Si is favored when expensive, high temperature sustaining substrates such as quartz, graphite, high temperature ceramics are used. Zone-melt re-crystallization is one such method which involves actual physical melting of a-Si before crystallization. Grain sizes in the order of several millimeters (mm) can be obtained [47]. However, this technique does not favor the use of plastics as substrates. Low temperature re-crystallization of a-Si is particularly favored when dealing with lower cost, relatively lower melting substrates. This technique also allows polysilicon films with grain sizes in the range of several tens of micrometers.

2.3.1 Solid Phase Crystallization (SPC)

SPC is a simple and cost effective technique which involves isothermal anneal of a-Si thin films at temperatures around 600 $^{\circ}\text{C}$ with anneal times ranging from couple of hours to

several tens of hours [47]. The films could be simultaneously doped by annealing the a-Si films in a closed chamber with n-type or p-type doping gas ambience. Polysilicon films with grain sizes of several micrometers are thus formed. However, this method suffers from the obvious disadvantage of long processing times and high crystallization temperatures. Pulsed rapid thermal processing (PRTP) is one of the other alternatives to SPC [73] which considerably reduces anneal times to obtain crystalline silicon films. Since the temperature required for SPC is higher than the T_g of polyimide substrates used we were forced to look for options.

2.3.2 Excimer Laser Crystallization (ELC)

Excimer laser crystallization or annealing (ELA) of a-Si films results in defect free polysilicon films with large grains with sizes of few micrometers [74, 75, 76, 77, 78]. The first step involves melting of a-Si by excimer laser pulses of extremely short duration of less than 100 ns. This allows a-Si to melt rapidly and solidify instantaneously without considerable heating or damage to the substrate. Another advantage of using pulsed laser is that it creates a large temperature gradient which allows nucleation to occur near the melting point of Si. Sequential lateral solidification (SLS) is an extension of ELA wherein the a-Si thin film is irradiated by an excimer laser through a patterned mask and the same process is sequentially repeated to cover the whole sample [79]. This technique mostly eliminates the non-uniformity of the melt and produces uniform polysilicon grains with sizes up to 200 μm [47]. The above techniques find their applications extensively in area of fabrication of TFTs.

Although this technique is compatible with low-temperature substrates, it has the disadvantages of being expensive, and highly susceptible to variations in the laser beam, which affect the film quality. It also has a narrow operating area dependent on the laser beam spot-size [78] which reduces throughput, and possibly introduces contamination due to the molten silicon layer from the substrate [80, 81].

2.4 Aluminum Induced Crystallization

Metal induced crystallization of a-Si employing different metals such as nickel (Ni), aluminum (Al), gold (Au), silver (Ag), copper (Cu), chromium (Cr), and palladium (Pd) to obtain

large grained, high quality polysilicon thin films at low temperatures was considered [82] due to the fact that the above metals in contact with a-Si layer induce phase transformation processes from amorphous to crystalline form at anneal temperatures well below the eutectic temperature (T_E) of the metal/Si system. Figure 2.1 shows the phase-diagram of a simple Al/Si binary system [83]. Table 2.1 lists some metal/Si systems with their eutectic temperatures (T_E) and crystallization temperatures (T_C).

Table 2.1 lists some metal/Si systems with their eutectic temperatures and crystallization temperatures. Al, Au, and Ag form simple eutectic (SE) systems with Si, in which there is no formation of stable silicides in thermodynamic equilibrium [90,91]. However, metastable silicide transition might be involved in the metal-induced crystallization process. Whereas Cu, Ni, Pd metals with Si form compound forming (CF) systems [90,92]. In CF systems there is a stable metal silicide formation at thermal equilibrium and it plays an important role in the crystallization process. In CF systems the stable silicide induces transformation of the amorphous to crystalline phase in Si rather than the metal itself.

Consider the example of Ni/Si system in Figure 2.2 [90]. As the Ni/Si system is annealed, metal silicide (NiSi_2) is either formed at the interface or as precipitate within the Ni implanted a-Si material [92]. The nodular NiSi_2 precipitates migrate through the a-Si crystallizing the traveled region as shown in Figure 2.2 (b).

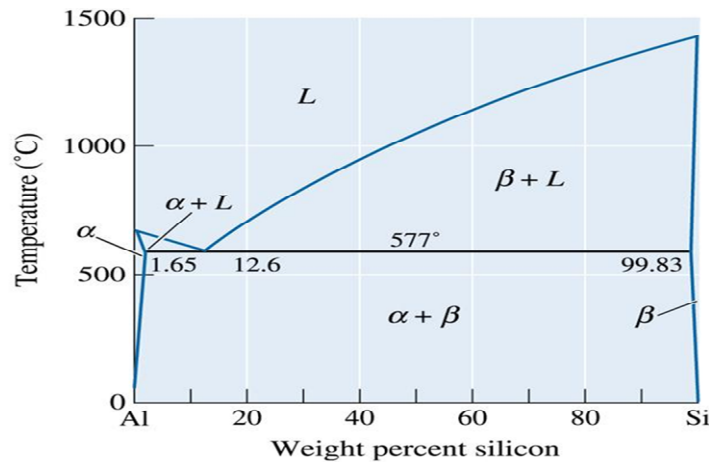


Figure 2.1 Phase-diagram for Al-Si binary system [83].

Table 2.1 Metal/Si systems with their corresponding T_E and T_C

Metal/Si [Ref.]	Eutectic Temperature (T_E) °C	Crystallization Temperature (T_C) °C
Au [84]	360	130
Al [85]	577	150
Ag [86]	830	350
Sb [87]	630	430
Cu [88]	802	485
Ni [89]	964	500

Thus, the metal silicide layer of thickness roughly of few mono-layers 5 nm [92] plays an important role in the phase transformation of a-Si to crystalline Si (c-Si). The individual atoms of Si are first transformed into Ni silicide as it moves through the a-Si region. In the second step the Si is released by the dissociation of NiSi_2 at the $\text{NiSi}_2/\text{c-Si}$ interface and hence gets incorporated into c-Si structure. This mechanism is based on the fact that the chemical potential of Ni (μ_{Ni}) is lower at the $\text{NiSi}_2/\text{a-Si}$ interface, where as the chemical potential of Si (μ_{Si}) is lower at the $\text{NiSi}_2/\text{c-Si}$ interface.

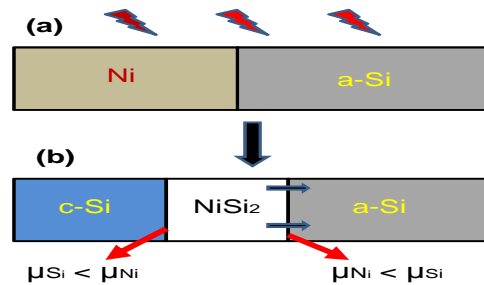


Figure 2.2 Ni/Si compound forming (CF) system describing metal induced crystallization process (a) initially, (b) during transformation [90].

In spite of low-temperature crystallization of a-Si, CF systems have the disadvantage of metal contamination of the c-Si due to the presence of stable silicides and relatively longer time necessary for crystallization [47,90].

In order to avoid possible metal contamination in the final polysilicon film, metals forming SE system with Si are often used. In present work, Al was used for crystallization of a-Si, as it is inexpensive and T_c as low as 150 °C had been reported [82]. By this process, continuous polysilicon films well below the eutectic temperature of 577 °C for Al/Si binary system are obtained. The process basically involves isothermal annealing of adjacent a-Si and Al thin films. First stage of the process starts with dissociation of Si atoms from the a-Si region into the Al region, followed by diffusion of Si atoms through the Al. The final stage involves nucleation of dissolved Si atoms and thus transforming into crystalline phase [82, 90]. The important thing to note in this technique is that Si and Al films exchange layer positions without forming a stable silicide, resulting in a relatively large grained polysilicon film [93]. Figure 2.3 illustrates the various steps involved in metal (Al) induced crystallization of a-Si. TEM investigations by Konno and Sinclair [94] prove that Al is ejected from its original position when the Si nucleation and growth occur within the Al layer.

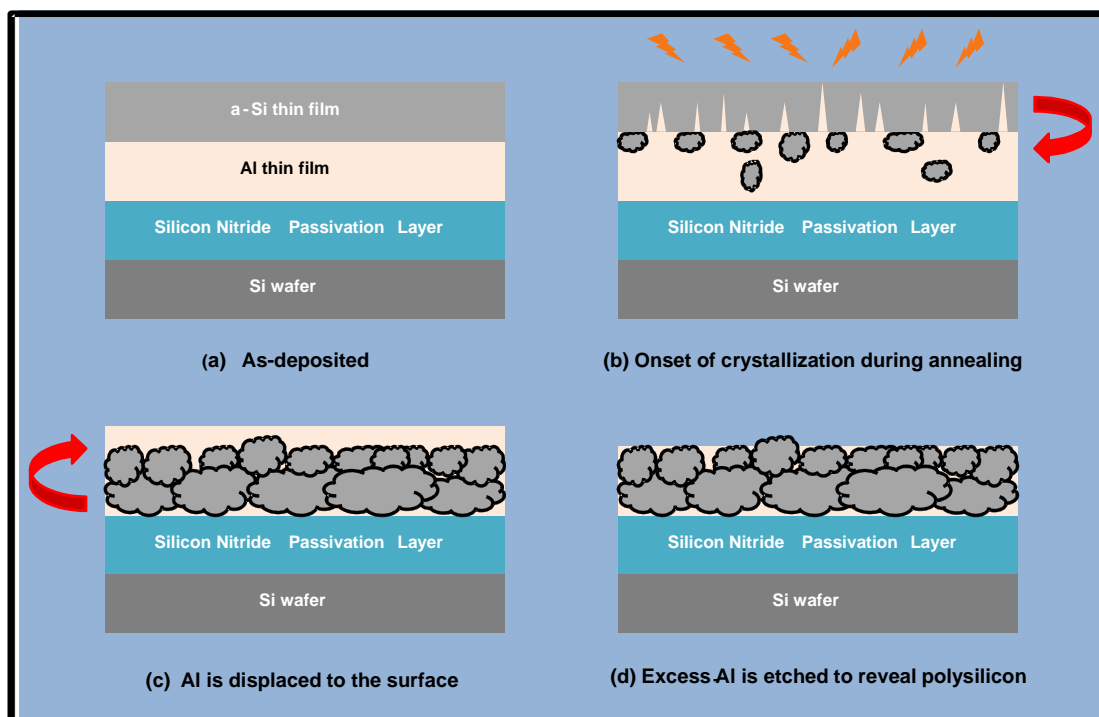


Figure 2.3 Metal induced crystallization process for Al/Si binary system (SE).

For SE system, the solid solubility of the Au and Al metal in the c-Si phase is about 10^{-4} at. % and 10^{-2} at. % respectively from [95]. By comparing the energy levels of incorporated metal impurities in c-Si caused by different metals, we can predict the nature of doping occurring. Ni and Au introduce deep states in the energy band gap of Si, whereas Al impurity state is only 60 meV above the valence band [96]. Such a shallow impurity state caused by Al gives rise to p-type doping when the Al atoms occupy the Si lattice sites, which indicates significant amount of doping by substitution. Thus, the polysilicon films obtained by AIC process have an advantage of being simultaneously p-type doped without the need for an extra post-deposition doping step.

2.4.1 Mechanism

The actual phenomenon occurring during the AIC of a-Si is still controversial and is topic of further study. Researchers are fairly equally divided into two groups based on the model they support. To explain the AIC of a-Si occurring below the crystallization temperature (T_c) of bulk a-Si, two possible mechanisms have been considered primarily as to how the metal (Al in our case) is instrumental in reducing the energy required to break the Si-Si covalent bonds to enable the diffusion process.

Tu's Interstitial Model – This model is based on the intermixing of Al and a-Si at the interface forming Al interstitials [97]. These interstitials change the nature of covalent bonding of neighboring a-Si lattice. The Si-Si bonds are no longer in their localized state and a transition occurs from a stronger covalent bond to a relatively weaker Si-Si bond resulting in Si atoms breaking away from their lattice, forming '*free Si*' and diffusing into Al as their activation energy is reduced. This model generally holds well for silicide forming metal/Si interfaces. However, some authors have adapted it for SE systems of Au/a-Si and Al/a-Si explaining crystallization with the formation of metastable silicide at the interface [82, 84]. Some authors have reported that this metastable silicide gradually decomposes at the temperatures above 300 °C [91, 98].

Hiraki's Screening Model – This model is based on the tendency of Al to 'screen' the Coulomb interaction by its mobile free electrons [99]. This leads to weakening of Si-Si bonds at

the Al/Si interface by the transition of non-metal to metal like bonding of the adjacent semiconductor material over the region of 2 monolayers (ML) at the interface [98] (1 ML of Si = 0.22 nm). This region is characterized by the formation of nearly uniform electron gas. The valence electrons of the Si in this region are not associated with specific atoms anymore and are free to move. The mobility in a covalent semiconductor is low compared to mobility in metals, thus the electron gas of a metallic like compound does not restrict the atomic motion as strongly as the electron configuration of a covalent semiconductor material. The atoms of a metallic-like, transformed semiconductor region near the metal interface are therefore more mobile than atoms of the bulk areas resulting in formation of *free Si*. The free Si can diffuse into Al along grain boundaries (GB). Other authors have shown by high-resolution TEM (HRTEM) studies on annealed a-Si/Al system that nucleation of single phase c-Si (<Si>) occurs at Al GBs. [98, 100]. Thus GBs in Al act as possible nucleation sites. More GBs result in more nucleation sites and thus smaller grain size (as in our case) and vice versa. Free Si atoms can diffuse into GBs of adjacent Al because there exists a thermodynamic driving force for this GB wetting. Subsequent crystallization of the Si occurs at Al GBs when the Si layer thickness exceeds the critical thickness (5 ML) [98]. The thermodynamic driving force for wetting of GBs, or the change in Gibbs free energy (ΔG) occurring after the annealing process at a particular anneal temperature (T_{anneal}) for an *immiscible bulk* alloy system case is given by the following Eq. (2.1) [101]:

$$\Delta G = d_{\{Si\}}\Delta G_{<Si>- \{Si\}} + d_{<Al>}\Delta G_{<Al>} + (\gamma_{<Al>}^S - \gamma_{\{Si\}}^S) + (\gamma_{<Al>-<Si>}^{int} - \gamma_{<Al>- \{Si\}}^{int}) \quad (2.1)$$

where { } - denotes amorphous state

< > - denotes crystalline state

d_{Si} = thickness of {Si} as -deposited,

d_{Al} = thickness of <Al> as-deposited,

$\Delta G_{<Si>- \{Si\}}$ – is the Gibbs energy difference per unit volume between <Si> and {Si} at T_{anneal} . Therefore, the first term on the right hand side of Eq. (2.1) represents the change in Gibbs free energy per unit area parallel to the surface between <Si> and {Si}.

$\Delta G_{<Al>}$ – is the Gibbs energy difference per unit volume between annealed <Al> and as deposited <Al> layer at T_{anneal} . The second term on the right hand side of Eq. (2.1) represents the change in Gibbs free energy per unit area parallel to the surface between annealed and as-deposited <Al> layer.

γ^S – represents corresponding surface energies of phase. The third term in the Eq. (2.1) represents the difference in surface energy between <Al> and {Si} layers.

γ^{int} – represents the interface-energy. The fourth term in Eq. (2.1) gives the interface energy difference between <Al>/ <Si> layer and <Al>/ {Si}.

Further analysis involving crystallization by wetting of a-Si film at Al GBs is carried out by authors in [98, 100, 101]. They give the total change in Gibbs free energy per unit length along Al GB parallel to the surface to be as [98]:

$$\Delta G = d_S^{crit.} d_{Al} \Delta G_{<S>- \{S\}} + d_{Al} (\gamma_{<S>/<Al>}^{int} - \gamma_{\{S\}/<Al>}^{int}) + d_S^{crit.} (\gamma_{<S>}^S - \gamma_{\{S\}/<Al>}^S + \gamma_{<S>/\{S\}}^{int}) \quad (2.2)$$

where $d^{crit.}$ is the critical thickness of the wetting a-Si layer for initiation of crystallization of a-Si at the Al GBs.

Table 2.2 gives experimental values of crystallization, surface and interface energies in Al/Si layer system at T_{anneal} of 400 °C and 200 °C. As seen by the $\Delta G_{<Si>- \{Si\}}$ in the following table, the crystallization of Si is favored along the Al GB during the AIC.

Table 2.2 Crystallization, surface and interface energies for Al/Si system [98]

T_{anneal} (°C)	$\Delta G_{<Si>- \{Si\}}$ (J/m ³)	$\gamma_{<Si>}^S$ (J/m ²)	$\gamma_{\{Si\}}^S$ (J/m ²)	$\gamma_{<S>/<Al>}^{int}$ (J/m ²)	$\gamma_{\{S\}/<Al>}^{int}$ (J/m ²)	$\gamma_{<Si>/\{Si\}}^{int}$ (J/m ²)
400	-8.4 x 10 ⁸	1.35	0.96	0.42	0.10	0.10
200	-8.9 x 10 ⁸	1.37	0.98	0.45	0.07	0.08

2.4.2 Crystallization Process

From Figure 2.1, we see that 1.5 at. % of Si atoms can dissolve in Al at temperatures below T_E (~577 °C). Additionally, the solid solubility of Si in evaporated Al was found to be around 0.2 at. % and 0.8 at. %, at crystallization temperatures of 400 °C and 500 °C respectively [90, 102]. Since Al in contact with a-Si is not in state of thermal equilibrium, a solid Al solution with Si solute is formed during the annealing process. For a system in thermal equilibrium, the chemical potential (μ) of one component is same in all phases. If we assume that each of the Al/a-Si and Al/c-Si system are in thermal equilibrium it follows that the chemical potentials of the Si atoms (μ_{Si}) in each phase of the individual systems are equal. We can write it as following [90]:

$$\mu_{<Si>} = \mu_{Al/<Si>} \quad (2.3)$$

$$\mu_{\{Si\}} = \mu_{Al/\{Si\}} \quad (2.4)$$

where $\mu_{Al/\{Si\}}$, $\mu_{Al/<Si>}$ denote the chemical potential of Si in Al when in contact with a-Si and c-Si, respectively. The excess molar Gibbs energy (ΔG) is then given by [90, 103]:

$$\Delta G = \mu_{Al/\{Si\}} - \mu_{Al/<Si>} \quad (2.5)$$

For a two-component system, the chemical potential for component A, (μ_A) can be represented as [103]:

$$\mu_A = \left(\frac{\partial G}{\partial n_A} \right)_{T, P, n_B} \quad (2.6)$$

where G is the Gibbs energy of the entire system, T is temperature, P is pressure, n_A and n_B are the number of moles of components A and B respectively. Therefore, ΔG is given as [103]:

$$\Delta G = \Delta H - T \Delta S = R_G T \ln a \quad (2.7)$$

where ΔH is the excess molar enthalpy, ΔS is the excess molar entropy, R_G is gas constant and a is the activity. From [104], the excess molar enthalpy can also be assumed as the enthalpy of

crystallization and is measured as 11.9 kJ/ mol. From [105], the excess molar entropy is measured as 1.66 J/ (mol- K). Using the above values, the activity, a of a-Si relative to c-Si can be estimated to be 6 at 475 °C [90]. This activity was used by Nast [90] to estimate the supersaturation of Al with Si solute when in contact with a-Si. Considering Al/a-Si in thermal equilibrium and no Si nucleation occurring before annealing, we can further represent as follows [103]:

$$\mu_{\{Si\}} = G_{Si} + R_G T \ln X_{\{Si\}} \quad (2.8)$$

$$\mu_{<Si>} = G_{Si} + R_G T \ln X_{<Si>} \quad (2.9)$$

where G_{Si} is the Gibbs energy of Si, mole fraction $X_i = N_A n_i$. Here, N_A is the Avogadro's number and n_i is the number of moles for $i = \{Si\}$ and $<Si>$. From Eq. (2.5) through (2.9) we can represent the activity, a as follows:

$$a = \frac{X_{\{Si\}}}{X_{<Si>}} \quad (2.10)$$

When the Al/c-Si system is in thermal equilibrium, Figure 2.1 determines the Si concentration in Al. The solid solubility of Si in Al at 475 °C is about $X_{<Si>} = 0.5$ at. % [90]. From Eq. 2.10, we get a value of $X_{\{Si\}} = 3$ at. % for $a = 6$. Therefore, it shows that if Al was not subject to solid solubility limit (no nucleation occurring), the Si concentration of Al in contact with a-Si would be 3 at. % when brought in thermal equilibrium at 475 °C. This Si concentration exceeds the maximal solubility of Si in Al as seen from phase diagram from Figure 2.1. Thus, in the Al/c-Si system, Al with such a high concentration of Si can be viewed as a super-saturated state. This super-saturation state is stabilized by further nucleation and growth of c-Si phase within the Al. Therefore, the crystallization process involves the a-Si phase adding Si atoms to the Al solution to increase the chemical potential of the Si solute while the growing c-Si phase is extracting Si to decrease this chemical potential. The Al is therefore in state of under-saturation in relation to a-Si and a state of super-saturation in relation to the c-Si. For the reduced anneal temperature of 400 °C, we obtain activity value of 7 with corresponding $X_{Al/\{Si\}}$ and $X_{Al/<Si>}$ of 1.4

at. % and 0.2 at. %, respectively [90]. This shows that the extent of super-saturation of Al solution in Si solute and corresponding activity increase with lower anneal temperatures.

2.4.3 Silicon Grain Growth

The starting point of crystallization of a-Si is nucleation at GBs followed by grain growth as discussed earlier in Section 2.4.1. For given T_{anneal} , a-Si atoms dissolve and diffuse into Al matrix. The concentration profile $C(x,t)$ of the Si solute from the interface into the Al, is dependent on the position x from the Al/a-Si interface, and time t is given by [103]:

$$C(x,t) = C_s - (C_s - C_0) \operatorname{erf} \left(\frac{x}{2\sqrt{Dt}} \right) \quad (2.11)$$

where C_0 (at $x=\infty$) is the Si concentration far away from the interface, C_s (at $x=0$) is the Si concentration at the interface, D is the diffusion coefficient and erf is the error function. In the vicinity of the grains, the Si solute is therefore depleted and the concentration C_i of the Si atoms at the Si grain/ Al interface is lower than C_s . Consequently, a concentration gradient establishes from the c-Si/Al interface extending into the Al matrix. The Si solute concentration decreases from C_s and C_i over a distance of the effective diffusion length L . From Fick's first law, the concentration gradient is related to flux, J of Si atoms, given by [90, 103]:

$$J = -Dg \frac{\partial C}{\partial x} = -Dg \frac{C_s - C_i}{L} \quad (2.12)$$

The Si grain growth velocity, v_g is related to J as [90]:

$$J = C_g v_g \quad (2.13)$$

where C_g is the atomic density of c-Si. From [90, 106], for $T_{\text{anneal}} = 475^\circ\text{C}$, and $C_s = 3$ at. %, $C_0 = 0$, $C_i = 0.5$ at. %, $D_{\text{Si}} = 10^{-8} \text{ cm}^2/\text{s}$, C_g for Si is $6 \times 10^{22} \text{ cm}^{-3}$, v_g of 4.7 nm/s is calculated.

2.4.4 Factors Affecting AIC

The important factors affecting AIC process are (i) annealing temperature, (ii) anneal time, (iii) layer thickness ratio, (iv) Al metal grain structure, (v) Al/a-Si interface layer, and (vi) annealing environment.

Lower annealing temperatures results in longer crystallization times, lower nucleation density, lower grain growth velocity and larger polysilicon grain sizes [107]. Longer anneal time increases the degree of crystalline nature of the final polysilicon film. Higher anneal temperature, however, results in shorter crystallization times [90,108]. Therefore, an optimum anneal profile must be selected for AIC as it greatly varies with the structure's layer hierarchy [109] and specific design requirements. Equal Al/a-Si layer thicknesses ratios are preferred to form good quality continuous polysilicon films under steady anneal conditions. If a-Si layer is thinner than Al layer, clusters of Si islands or crystallites on the surface of the polysilicon film are common and also the final polysilicon film is non-continuous [109, 110]. On the other hand, thinner Al layer results in relatively lower rate of crystallization and there is no added advantage of higher a-Si/Al ratios as the thickness of the final polysilicon film primarily depends only on the Al layer thickness. The excess Si gets accumulated on top of the polysilicon film as a porous Si network [90, 109].

The variations in Al grain structures due to films obtained by different deposition techniques viz. thermal evaporation, e-beam evaporation, sputtering play an important role during the polysilicon grain nucleation at GBs of Al film, and eventually the Si diffusion and the polysilicon grain growth steps. Thermal evaporation gives larger Al grains which eventually results in large grain polysilicon film as the distance between adjacent GBs is larger. However, the final polysilicon suffers from non-smooth surface, relatively poor reproducibility and longer crystallization times. E-beam evaporation of Al results in the smallest grain polysilicon film because of smaller grain texture of Al film obtained. However, it provides good reproducibility and shorter crystallization times. Present work uses sputtering as it results in a good compromise between the crystallization times and final polysilicon grain sizes. Moreover, sputtering process is simpler and has good reproducibility.

The interface layer between Al/a-Si layers also affects the final polysilicon film grain size, and crystallization times [90, 109, 110]. For example, presence of aluminum oxide (Al_2O_3) on the interface layers results in larger polysilicon grain growth. However, it slows down the

crystallization process due to increase in the activation energy needed for the Si nucleation process. Few authors [90, 99, 108] have intentionally oxidized Al metal prior to a-Si deposition by exposing it to air, and in a furnace for a period ranging from two hours to several weeks, and then performing the crystallization process. Present work, however, does not incorporate Al_2O_3 interface layer thereby reducing processing times considerably. Few studies suggest that the presence of an oxide layer is not a requirement for the crystallization of a-Si, but it acts as a physical barrier to restrict the vertical growth of Si grains and hence result in films with larger grains [90]. The annealing environment at which crystallization is carried out determines the texture of the final polysilicon film and possibly enhances the electrical characteristics [90,108 110]. Typically, annealing is performed in vacuum, nitrogen (N_2), forming gas (98 % N_2 + 2 % H_2), and H_2 atmosphere. Annealing performed in presence of H_2 results in smooth surface and uniform polysilicon films. AIC performed in presence of forming gas resulted in relatively larger grain sizes and shorter crystallization times even with Al_2O_3 present as an interface layer [111, 112]. Present work uses forming gas as it provided us with a good compromise between grain size, and crystallization time. Furthermore, H^+ effectively passivates any dangling Si-Si bonds.

2.5 Aluminum-Induced Crystallization Process Development and Analysis

To determine the feasibility of obtaining polysilicon thin films by AIC on flexible polyimide substrates and its subsequent use as a piezoresistive material, we wanted to investigate polysilicon film's structural and electrical properties. In order to do that, a clean p-type Si <100> wafer was taken and a passivation layer of rf sputtered Si_3N_4 of thickness 1 μm was deposited. Subsequently, a 0.5 μm thick Al thin film was deposited using dc sputtering at power of 150 W, and sputter pressure of 2.8 mTorr. This was immediately followed by a 0.5 μm thick deposition of a-Si layer by rf sputtering at a power of 150 W and sputter pressure of 2.8 mTorr, without breaking the sputter chamber vacuum. All of the sputter depositions were carried in ATC Orion UHV Sputter System (by *AJA International Inc., USA*). This sample was to undergo different anneal profiles, i.e. with respect to anneal temperature and time in order to determine optimal conditions for successful AIC process. JetFirst 150 (by *Jipelec, France*)

Rapid Thermal Annealer (RTA) was used so that we could easily control the anneal profiles, and switch the gas-lines for obtaining different annealing ambience. Annealing was done in presence of forming gas. Initially the RTA chamber was purged with N_2 with flow of 250 sccm for 120 s. Later, the sample was placed inside the RTA chamber again followed by N_2 purge. Vacuum was pulled for 1200 s with sample inside the chamber. Later forming gas was flowed in the chamber at the flow of 50 sccm for 120 s. The anneal temperature was ramped up from room temperature to target anneal temperature at the rate of 40-45 °C/ min with a gas flow rate of 150 sccm. The anneal was performed at the target temperature for times ranging from 30 minutes to 90 minutes in continuous gas flow. After the end of the dwell cycle, the temperature was ramped down at the same rate as ramp –up cycle. This was followed by chamber cooling by purging in N_2 for 1200 s. Later, the sample was removed from the RTA chamber for further analysis. In order to etch the excess Al from the surface, the samples were selective treated in Al-etch solution maintained at 55 °C for 90-120 s, thereby exposing final polysilicon film obtained by AIC.

In another set of experiments, several clean p-type Si <100> wafers were taken with a passivation layer of rf sputtered Si_3N_4 of thickness 0.5 μm deposited on them. Subsequently, multiple layers of polyimide PI 2611 (by *HD Microsystems, USA*) were spin-coated on individual wafers to obtain a 40 μm thick flexible substrate layer and 3 μm thick sacrificial layer, and cured at curing temperatures ranging from 350 °C - 550 °C in N_2 environment in Blue M Oven. The curing profile was varied from dwell time of 1 sec to 2 hours at the maximum curing temperature. This experiment was carried out to study the survivability of the polyimide layer as a substrate and a sacrificial layer at high anneal temperatures and look for any de-lamination or cracks in subsequent layers. A detailed curing profile is described in Chapter 3 in the section dealing with fabrication of pressure sensors on flexible substrates.

2.5.1 Scanning Electron Microscopy (SEM)

The SEM analysis was carried out using Zeiss Supra 55 VP Scanning Electron Microscope. Figure 2.4 illustrates the SEM image of a polysilicon film obtained by AIC at 500 °C

for 90 min and subsequent etching in Al-etch solution. As seen from the SEM image, the polysilicon grains tend to have an average size between 150 nm and 200 nm. Focused-Ion Beam (FIB) milling of sample as shown in Figure 2.5 was done by Zeiss 1540XB Cross-Beam E-Beam Writer. This was done to compare the cross-sections of the as-deposited and final polysilicon films obtained by AIC at 400 °C for 90 minutes. From Figure 2.5 (a), Al film can be clearly seen under equally thick a-Si film. In Figure 2.5 (b) following the AIC process, the a-Si and Al film exchange layer positions and excess Al accumulates at the surface which is later etched away by Al-etch solution to reveal polysilicon film.

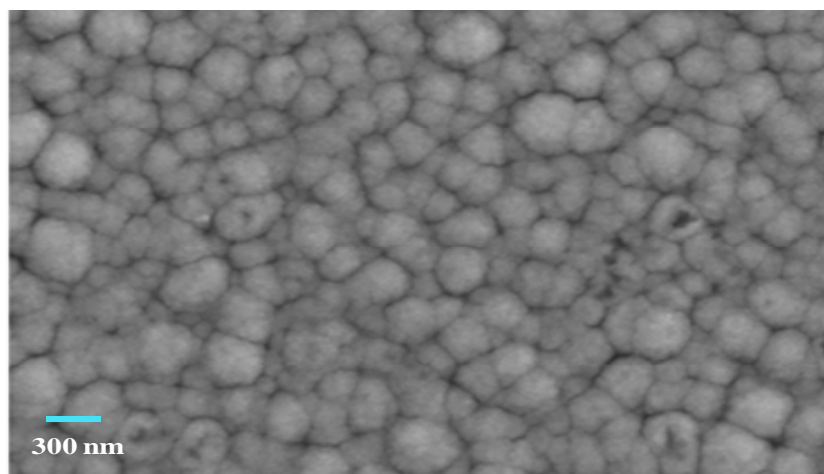


Figure 2.4 SEM image of the final polysilicon film obtained by AIC at 500 °C, for 90 minutes and subsequently etched in Al-etch [17].

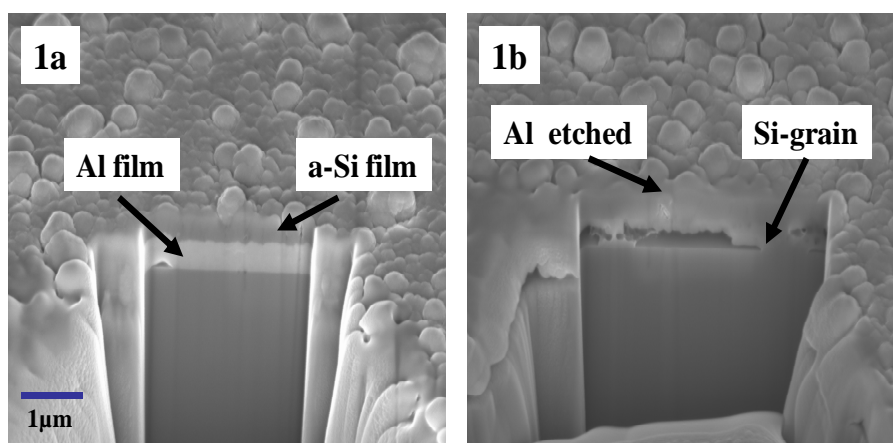


Figure 2.5 SEM image of (a) as-deposited a-Si film sectioned with FIB and (b) polysilicon film annealed at 400 °C and subsequently etched in Al-etch solution [17].

2.5.2 Energy Dispersive Spectroscopy (EDS)

EDS analysis was done in a Zeiss Supra 55 VP Scanning Electron Microscope. As given in Table 2.3 at. % of different elements present in the sample for three different conditions: (i) as-deposited, (ii) after AIC process, and (iii) after Al-etch were obtained. These measurements clearly substantiated with the FIB cross-sectional analysis. It could be seen that a small amount of Al was embedded in the final crystallized film which acts as a p-type dopant in the polysilicon film. This eliminated the need for an additional doping step. However, it was observed that a small amount of oxygen (O₂) is incorporated in the film which may be during the anneal step or due to the formation of a thin native oxide on the surface.

Table 2.3 EDS profile for samples at polysilicon obtained at 400 °C, 90 minutes

Sample	Element	Wt. %	At. %
As-deposited	O	5.73	9.63
	Al	5.46	5.44
	Si	88.8	84.93
After annealing at 400 °C for 90 minutes	O	12.39	19.28
	Al	84.12	77.62
	Si	3.49	3.09
After annealing and etching in Al-Etch	O	18.78	28.85
	Al	1.90	1.70
	Si	79.31	69.42

2.5.3 X-Ray Diffraction (XRD)

To ensure that the final film obtained by AIC of a-Si is polycrystalline in nature, XRD measurements were carried out for samples annealed at different temperatures ranging from 400 °C to 500 °C with annealing times of 30 to 90 minutes. Siemens D500 X-Ray Diffractometer was used to perform XRD analysis. The samples were annealed in a forming gas ambient. The presence of H₂ results in a smooth surface and a uniform polysilicon film with minimal residual stress. In addition, the anneal time to achieve crystallization was found to be much shorter than the case with pure N₂ since H₂ aids the diffusion of Si and Al [113].

The voltage was set to 40 kV and current was set to 30 mA. X-ray was generated from $\text{Cu K}\alpha$ source of wavelength 1.54 Å. The peak for <100> plane for silicon was obtained for 2θ value of 69.13°. Then, scan measurements were performed by selecting a 2θ range from 20° to 60°. In the first set of experiments, the annealing temperature was kept constant at 500 °C and the time was varied from 30 to 90 minutes in 15 minute intervals. Figure 2.6 compares the XRD plots of the films annealed at 500 °C with anneal times of 45-90 minutes to the as-deposited amorphous film.

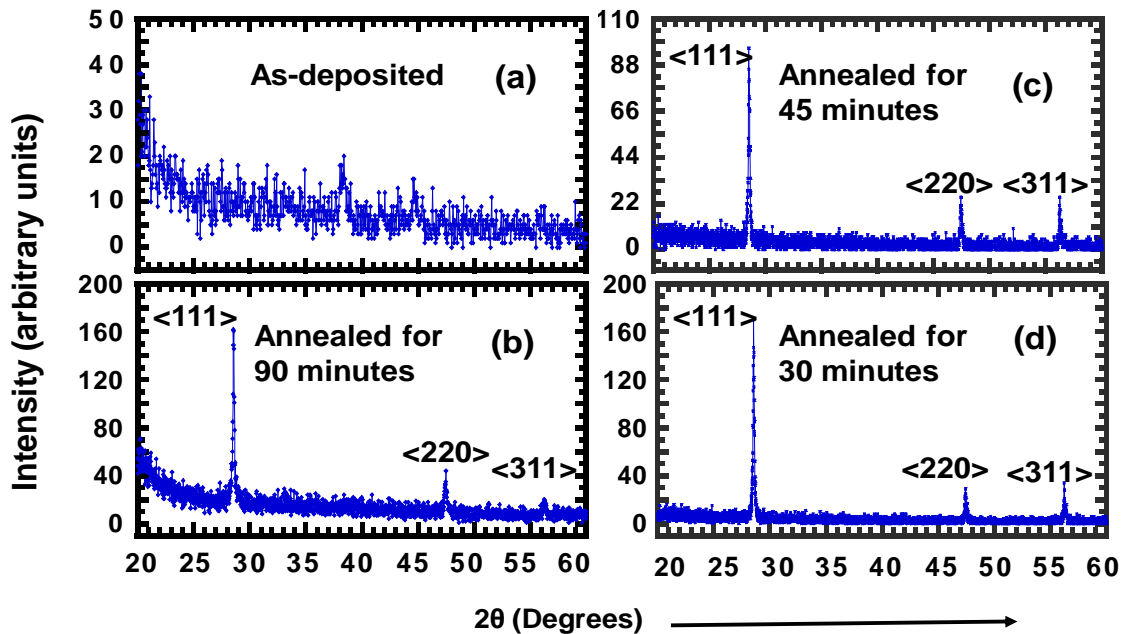


Figure 2.6 XRD plots for (a) as-deposited a-Si film and the films annealed at 500 °C (b) for 90 minutes, (c) for 45 minutes and (d) for 30 minutes in forming gas and subsequently etched in Al-etch.

In the second set, the annealing time was kept constant at 60 minutes and only the annealing temperature was varied from 400 °C to 500 °C. Figure 2.7 shows the XRD plots for polysilicon films obtained at a constant annealing time of 60 minutes for annealing temperatures of 400 °C, 450 °C, 475 °C and 500 °C. These experiments were aimed to help us study the surface morphology of the final polysilicon film and variations in grain sizes with different anneal profile (i.e. temperatures and time).

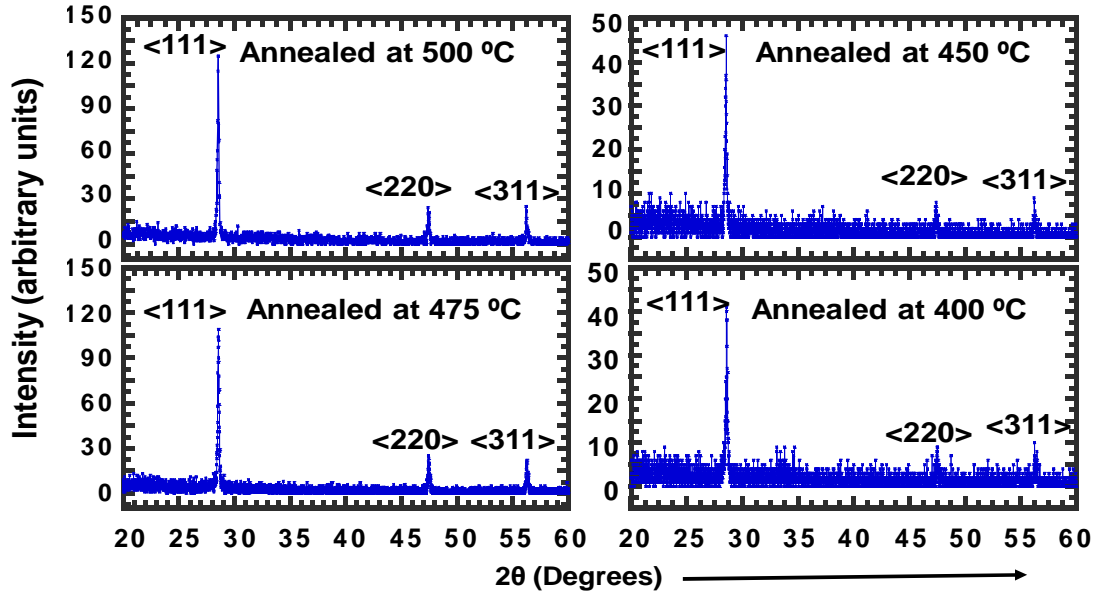


Figure 2.7 XRD plots for polysilicon film obtained by annealing at 500 °C, 475 °C, 450 °C and 400 °C for 60 minutes in forming gas and sub sequently etched in Al-etch.

Table 2.4 gives the location of corresponding <111>, <220> and <311> peaks for different annealing temperatures and times described above. These measurements validate the polycrystalline nature of the resultant film obtained by AIC of a-Si. Debye-Scherrer's formula was used to estimate the grain sizes, L_c (nm) of the films [114]:

$$L_c = \frac{K * \lambda_{Cu-\alpha}}{B * \cos(\theta_B)} \quad (2.14)$$

where, K (= 0.9) is the grain shape factor, θ_B is the Bragg's angle where the maximum peak value occurs and $\lambda_{Cu-\alpha}$ (= 1.54 Å) is the wavelength of Cu- α source. Peak <111> was considered for estimating the grain sizes of the polysilicon film obtained by AIC with different annealing profiles. Estimated polysilicon grain sizes for films annealed at different temperatures and for varying duration are shown in Table 2.4, calculated using Eq. (2.14) by Gaussian fitting to determine the Full Width at Half Maximum (FWHM), B from the observed peaks (refer to APPENDIX A).

Table 2.4 XRD Analysis of polysilicon films obtained at different annealing temperatures and times with grain size ranges (* Gaussian Fit)

Anneal Temperature (°C)	Anneal Time (minutes)	Location of Peaks			Estimated Grain Size Ranges* (nm)
		<111>	<220>	<311>	
475	90	28.48°	47.34°	56.20°	60
500	90	28.54°	47.48°	56.28°	65
550	90	28.70°	47.58°	56.42°	35
500	60	28.50°	47.32°	56.15°	53
475	60	28.52°	47.41°	56.23°	51
450	60	28.48°	47.37°	56.17°	49
400	60	28.48°	47.36°	56.18°	47
500	45	28.47°	47.33°	56.15°	54
500	30	28.50°	47.39°	56.20°	51

The difference in grain sizes estimated from SEM micrograph and from XRD measurements are accounted to certain percentage of machine calibration error introduced during the measurement of B from XRD peaks which leads to peak widening thus increasing B . This results in underestimation of the grain size. On the other hand, the inability of an SEM image to reveal all grains comprising of various small-angled grain boundaries results in overestimating the grain sizes.

We see that for a constant annealing temperature of 500 °C, the grain size increases somewhat with increasing annealing time. Table 2.4 also shows that for a constant annealing time of 60 minutes, lower anneal temperatures result in smaller grain sizes, also reported by Y. Matsumoto et al. [115].

The authors in [115] treated a-Si:H film obtained by PECVD with 10% HF solution to remove any native SiO₂ prior to Al evaporation. However, to obtain large polysilicon grains from AIC, lower temperatures are preferred [90,108]. One of the possible reasons for this observed

anomaly could be the absence of any interfacial oxide layer on the Al/Si interface, as in our case. The Si film was deposited immediately after Al film sputtering without breaking the chamber vacuum, which was maintained at 1.33×10^{-6} to 13.3×10^{-6} Pa range. Earlier works on AIC stated that when Al layer was intentionally oxidized by exposing to air for a few minutes to a couple of weeks to grow Al_2O_3 on the interface, larger grains resulted, however, at the expense of increased required crystallization times [90].

2.5.3 Sheet Resistance Measurements

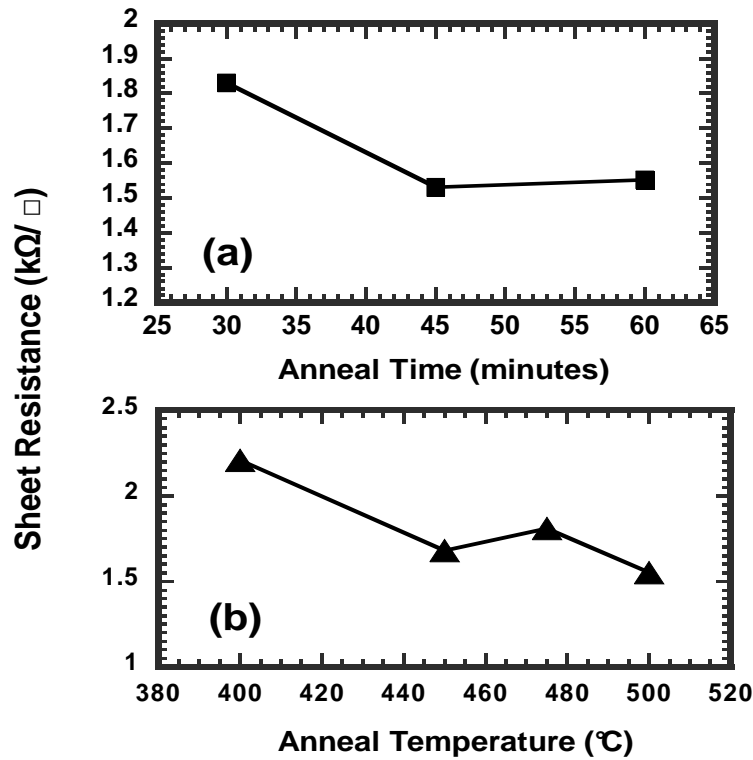


Figure 2.8 Measured sheet resistance for polysilicon films of thickness $\sim 0.5 \mu\text{m}$ obtained (a) by annealing at 500°C for anneal times of 30, 45 and 60 minutes, and (b) with constant anneal time of 60 minutes and for anneal temperatures of 400°C , 450°C , 475°C and 500°C .

The sheet resistance of the polysilicon films obtained at different annealing conditions was measured using a Jandel 4-Point four-point probe. Figure 2.8 illustrates the variation of sheet resistances for different annealing profiles and shows that the obtained polysilicon films exhibit good electrical characteristics with Al as the dopant, which makes it a p-type polysilicon

film. The Al occupies the vacant lattice positions left behind by the migrating Si and results in substitutional diffusion making it a p-type doped polysilicon [90]. In addition the polysilicon thin film obtained as described above possesses grains being preferentially oriented in $\langle 100 \rangle$ direction [112, 116].

2.6 Summary

In this chapter, some commonly used polysilicon thin film deposition methods are introduced. Post deposition techniques for crystallization of a-Si using solid phase crystallization and excimer laser annealing to obtain polysilicon films are described. AIC crystallization technique is explained for obtaining uniform polysilicon films at low temperatures for flexible substrate applications. Since Al/Si form simple eutectic system they are assumed not to form stable silicides during transformation unlike some other metals such as Ni, Cu etc. which form stable silicides (CF system) with Si. A corresponding explanation describing the AIC of a-Si using Hiraki's screening model is given. The aluminum induced crystallization process steps, and the transformation of a-Si into c-Si has been explained using some basic thermodynamic principles. Various factors such as anneal temperature, anneal time, Al/Si layer thickness ratios, Al film grain structure, Al/a-Si interface layer and anneal environment affecting AIC are explained. This is followed by the development of AIC process for obtaining polysilicon thin films on flexible polyimide substrates. The processing conditions involving anneal profile, anneal conditions, Al/a-Si layer thickness ratios, method of depositions of Al/a-Si to obtain relatively large grained polysilicon film with good uniformity, texture and electrical characteristics optimized. This was done by carrying out several experiments to determine the survivability of polyimide substrate at higher temperatures ($\geq T_g$) during annealing and involved subjecting multiple samples to varied anneal profiles.

SEM/EDS experiments concurred that the layer exchange process occurs even without the presence of Al_2O_3 as interface layer, thereby, reducing the crystallization times. Our XRD experiments confirmed good crystalline nature of the final polysilicon film obtained by AIC at various anneal profiles. The electrical measurements using four point probe method clearly

established the p-type nature of resultant polysilicon film and also showed that films have comparable sheet resistance values to polysilicon films as obtained from other conventional deposition methods.

CHAPTER 3

FABRICATION OF PRESSURE SENSORS ON FLEXIBLE SUBSTRATES

After successfully obtaining a low-temperature polysilicon film by AIC of a-Si on polyimide substrates as described in Chapter 2, we proceeded with the fabrication of pressure sensors. Their design was based on the work in [16,72]. The pressure sensor basically comprised of a micromachined Si_3N_4 shuttle plate, which connects to the flexible substrate through bridge arms where the polysilicon piezoresistors were placed. The shuttle plate and the connecting arm to the substrate make-up the diaphragm or the membrane layer, released by surface micromachining of the sacrificial polyimide layer underneath. Piezoresistors were deposited using AIC technique and were patterned on the bridge arms of the diaphragm layer. They were later connected to each other using Al interconnects to form a half-Wheatstone bridge circuit. These sensors were made to target for low pressure sensing applications in the range of 0-50 kPa.

Several designs with different diaphragm dimensions and shapes were fabricated on a die. Alternatively, the shapes and sizes of the piezoresistors were also varied to study their effects on the sensitivity (S) of the pressure sensor. Appendix B gives the mask layout of different pressure sensors in a die. Their diaphragm sizes varied from $40 \times 40 \mu\text{m}^2$ to $80 \times 80 \mu\text{m}^2$. Additionally, different piezoresistors namely U-shaped, UY-shaped, I-shaped, long U-shaped were considered. Individual dimensions of these piezoresistors are added in Appendix B for further reference. A schematic of one such half-Wheatstone Bridge pressure sensor is depicted in Figure 1.2, together with the cross-section view. Here, the two resistors R_2 and R_4 on the micromachined diaphragm form the active piezoresistors, whereas the resistors R_1 and R_3 which lie outside the diaphragm area on the membrane layer make the passive resistors of the Wheatstone bridge. In the subsequent sections of this Chapter, fabrication of pressure

sensors on the flexible substrate will be described, starting with flexible polyimide substrate preparation and subsequent layer build-up.

3.1 Pressure Sensor Fabrication Steps

3.1.1 Preparation of Flexible Substrate

This was a very important step in fabrication of our pressure sensors because of an inherent requirement for the polyimide substrate to survive high temperature anneal cycles during AIC of a-Si for obtaining polysilicon films. During this stage improper substrate preparation and curing profile would have resulted in de-lamination and flaking of the polyimide layers from the base Si wafer which was exclusively used for providing structural support during the build-up of subsequent layers. Polyimide PI-2611 was used as a flexible substrate material as described earlier in Chapter 1. Since PI-2611 is a highly viscous liquid, in order to obtain it as a solid substrate, we had to first spin-coat it on a Si wafer. In the final stage, the whole flexible substrate with completed devices could be easily peeled off from the base Si wafer thus revealing successful fabrication of sensors on flexible polyimide substrate.

The preparation of flexible substrate started with cleaning a <100> p-type Si wafer with trichloroethylene (TCE), followed by acetone and methanol dip, and finally by DI water rinse. The wafer was treated in piranha solution followed by treatment in 10:1 HF solution to remove any residual organics and native oxide on the wafer surface. The wafer was subsequently rinsed in DI water to remove any residual acids and dehydrated at 120 °C for 5 minutes. After letting the wafer to cool down at room-temperature. It was transferred into the sputter system chamber for deposition of Si₃N₄ layer deposition. This layer has advantages by serving as passivation layer on the Si wafer and by providing good adhesion of the flexible polyimide substrate layer.

ATC Orion UHV Sputter System was used to sputter a 0.5 µm thick Si₃N₄ film as shown in Figure 3.1 (a) for passivation at rf power of 150W and sputter pressure of 2.8 mTorr. This was followed by spin-coating PI-2611 on the passivated wafer. The spin-coat was carried out in gradual increment of spin-speeds for film uniformity. Initially, PI-2611 is spun at 500 rpm for 5

seconds, then at 1000 rpm for 5 seconds followed by 2000 rpm for 5 seconds and final spin of 3000 rpm for 30 seconds. The ramp-up rate of spin was kept constant at 250 rpm/ second. After the spin-coat, the wafer was baked at 130 °C on a hot plate for 4 minutes. The same procedure was repeated for 5 times to obtain a thick polyimide substrate on the Si wafer. Later, the wafer was cured in Blue M oven in the presence of N₂ flow at temperatures of 450 °C for 2 hours. The thickness of final cured polyimide substrate film was around 40 - 45 µm as shown in Figure 3.1 (b).

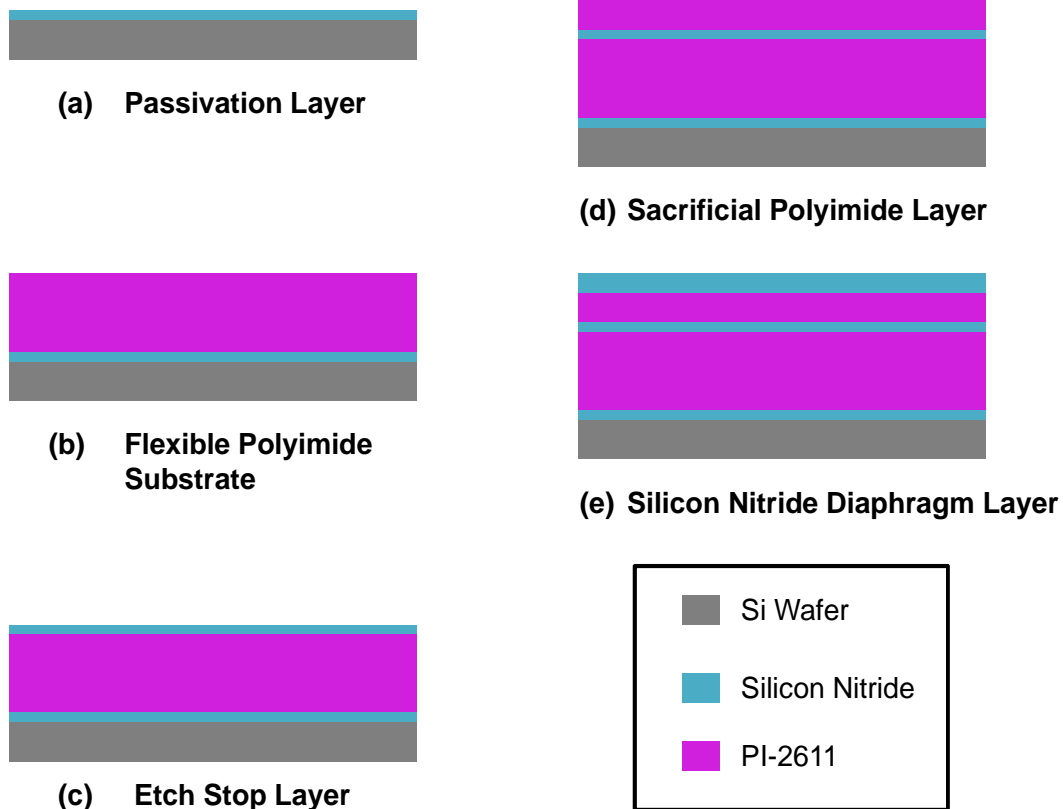


Figure 3.1 Cross-sectional schematic showing step by step fabrication process flow for pressure sensor.

3.1.2 Preparation of Polyimide as Sacrificial Layer

PI-2611 was again used as a sacrificial layer which would be eventually etched away (by ashing) in the final step to suspend the Si₃N₄ diaphragm and thereby resulting in the

completion of fabrication process for the pressure sensor. The use of the polyimide as sacrificial layer facilitated dry etch in O_2 plasma. This was a clean process which eliminated the stiction problem commonly experienced during the release of MEMS structures by wet-etch procedure. To enable this, a $0.5\text{ }\mu\text{m}$ thick Si_3N_4 film as shown in Figure 3.1 (c) was deposited at the rf power of 150W and sputter pressure of 2.8 mTorr. This layer acted as an etch-stop while dry-etching of sacrificial polyimide layer. This ensured that only the sacrificial polyimide layer underneath the diaphragm layer was etched leaving the polyimide substrate layer unharmed. The spin-coat of polyimide PI-2611 was carried out as described earlier in Section 3.1.1. However, only a single coat was needed in this case. The sample was later cured in the oven at $450\text{ }^\circ\text{C}$ for 2 hours to obtain the final thickness of $3.0 - 3.3\text{ }\mu\text{m}$ polyimide film as illustrated in Figure 3.1 (d).

3.1.3 Diaphragm Layer Deposition and Etching

A $1.5\text{ }\mu\text{m}$ Si_3N_4 film was deposited by rf sputtering as the diaphragm layer as shown in Figure 3.1 (e). In order to suspend this layer, windows or openings defining different diaphragm shapes and sizes were needed. This was performed by photolithography using negative resist NR9-3000P (*by Futurrex Inc., New Jersey, USA*). NR9-3000P was spin-coated at 1200 rpm for 40 sec to get a resist film thickness of $5.18\text{ }\mu\text{m}$. The sample was pre-exposure baked at $150\text{ }^\circ\text{C}$ on a hot plate for 75 seconds. The sample was later exposed under the trench mask for 11 seconds under UV light with intensity of 18 mW/cm^2 using Model 806 Front/Back Contact Mask Aligner (*by OAI, California, USA*). This was followed by post-exposure bake of the sample at $120\text{ }^\circ\text{C}$ on a hot plate for 90 sec. The sample was developed in the resist developer RD6 (*by Futurrex Inc., New Jersey, USA*) for 30 seconds. An additional post-develop bake of the sample was carried out at $120\text{ }^\circ\text{C}$ on a hot plate for 5 minutes to harden the photo-resist to use it as a mask during the reactive-ion etch (RIE) step to etch silicon nitride for opening the windows in the diaphragm layer.

Micro-RIE Series 800 Plasma System was used to etch Si_3N_4 using carbon fluoride (CF_4) gas at RIE power of 100 W in steps of 10 minutes to avoid heating of the sample. The total etch

time was around 40 minutes. Later the residual resist was removed by ultrasonic agitation in acetone for 5 minutes. This results in obtaining Si_3N_4 diaphragms of different shapes and sizes as illustrated in Figure 3.2 and from SEM images in Figure 3.3. The average measured thickness of RIE etched Si_3N_4 was around $1.67\text{ }\mu\text{m}$.

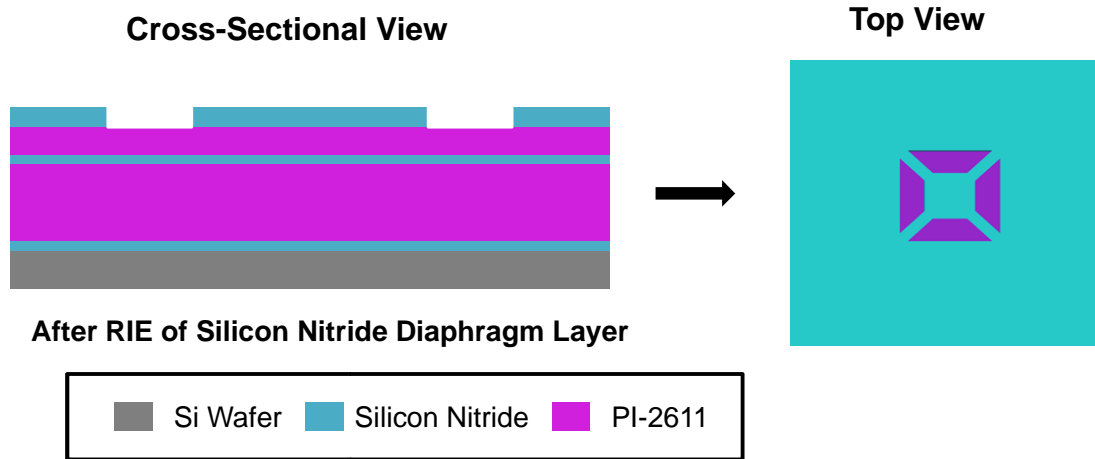


Figure 3.2 Schematic showing step by step fabrication process flow for pressure sensor.

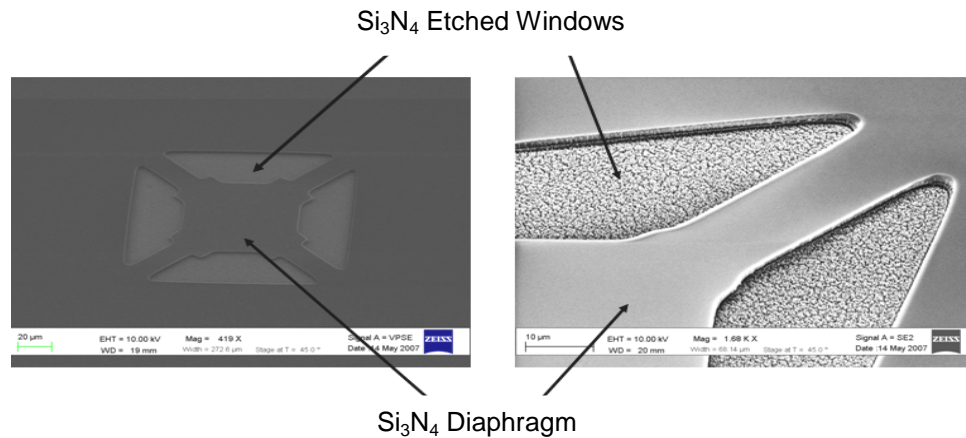


Figure 3.3 SEM images after patterning and RIE of Si_3N_4 diaphragm layer.

3.2 Polysilicon Piezoresistors by AIC

After etching of windows in Si_3N_4 diaphragm layer, we had to deposit polysilicon for piezoresistors and subsequent electrical connections to complete our fabrication of the sensor. Due to the thermal budget constraints of the polyimide substrate, a low temperature polysilicon

film obtained by AIC of a-Si similar to that described in Section 2.5 was used to fabricate the piezoresistors.

3.2.1 Polysilicon film by AIC

In order to define piezoresistors, photolithography was performed using negative resist NR9-3000P. It was spin-coated at 3500 rpm for 40 sec to get an average resist film thickness of 2.5 μm . The sample was pre-exposure baked at 150 °C on a hot plate for 75 seconds. The sample was later exposed under the piezoresistor mask for 9 seconds under UV light with intensity of 18 mW/cm² using Model 806 Front/Back Contact Mask Aligner. This was followed by post-exposure bake of the sample at 120 °C on a hot plate for 60 sec. The sample was developed in resist developer RD6 for 24 seconds. The sample was immediately transferred to the sputter system chamber. Next, a 0.5 μm thick Al was deposited by sputtering at a dc power of 150 W and the sputter pressure of 2.8 mTorr. Subsequently, a 0.5 μm thick a-Si was rf sputtered with power of 150 W at the same sputter pressure without breaking the vacuum. Post deposition, the sample was removed from the chamber and lift-off was performed in acetone without ultrasonic agitation to obtain well defined piezoresistors as shown by the schematic diagram in Figure 3.4 and in optical microscope pictures in Figure 3.5.

The sample is annealed in Jetfirst RTA at 400 °C for 90 minutes in forming gas ambient. The annealing profile is similar to the one described in Section 2.5. The samples annealed are later etched in Al-etch solution maintained at 55 °C for approximately 120 seconds. This results in polysilicon piezoresistors on the bridge arms of the diaphragm as shown in schematic of Figure 3.6.

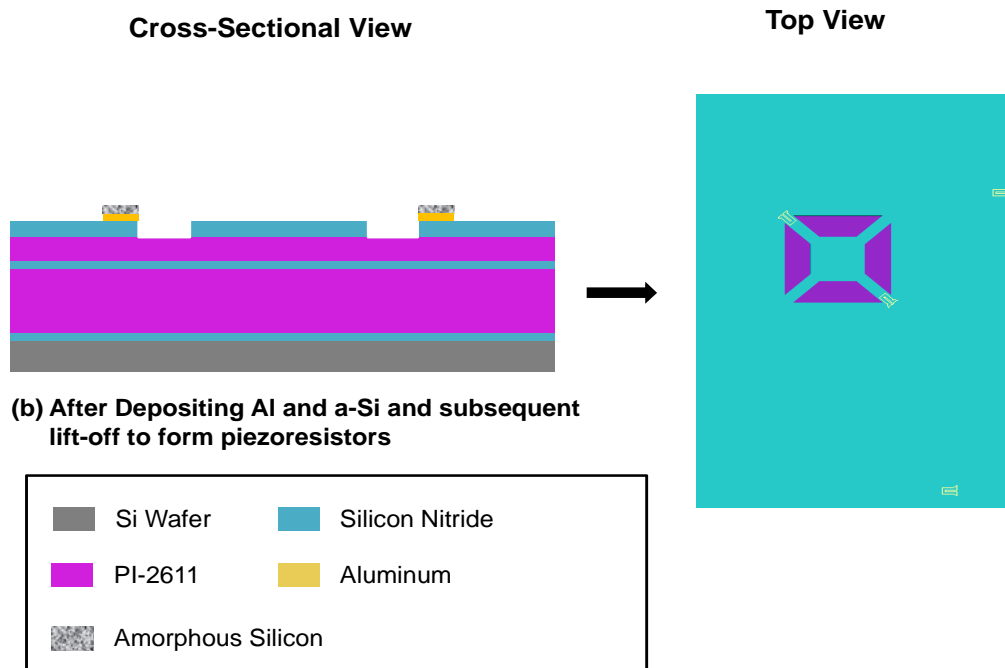


Figure 3.4 Schematic diagram after deposition of Al and a-Si and subsequent lift-off to obtain piezoresistors.

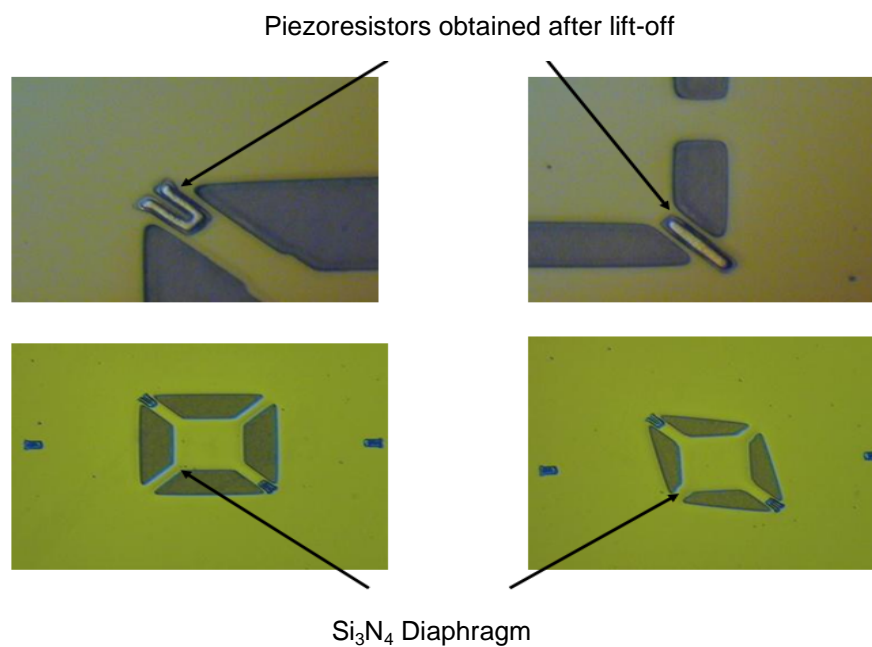


Figure 3.5 Optical microscope images of the pressure sensors corresponding to schematic of Figure 3.4.

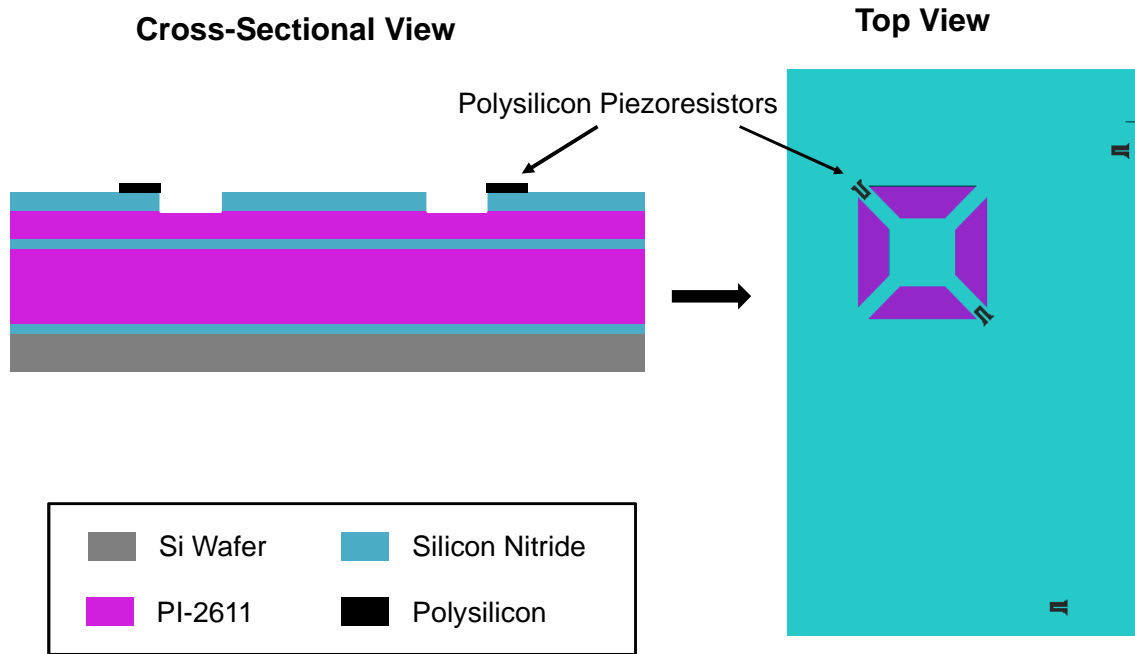


Figure 3.6 Schematic cross-sectional diagram after AIC of a-Si and subsequent etching in Al-etch solution to obtain polysilicon piezoresistors.

3.2.2 Aluminum Interconnects

In order to connect the piezoresistors in half-Wheatstone bridge circuit for measurement of pressure, Al interconnections are needed. This is performed using NR9-3000P photoresist, which was spin-coated at 3000 rpm for 40 sec to obtain an average resist film thickness of 3.14 μm . The sample was pre-exposure baked at 150 °C on a hot plate for 75 seconds, followed by exposure to UV light of intensity 18 mW/cm^2 for 11 sec, using the Al-interconnect mask. Next was the post-exposure bake of the sample at 120 °C on a hot plate for 60 sec. The sample was developed in resist developer RD6 for 28 sec, and immediately transferred to the sputter system chamber. Next, a 1.0 μm thick Al was deposited by sputtering at the dc power of 150 W and sputter pressure of 2.8 mTorr, as shown in Figure 3.7. Post-deposition lift-off in acetone was performed to obtain Al interconnections. In order to form an Ohmic contact between polysilicon and Al metal, the sample was annealed in RTA for 400 °C for 20 minutes in forming gas ambient. Figure 3.8 shows some of the optical microscope images of pressure sensors after Al interconnections.

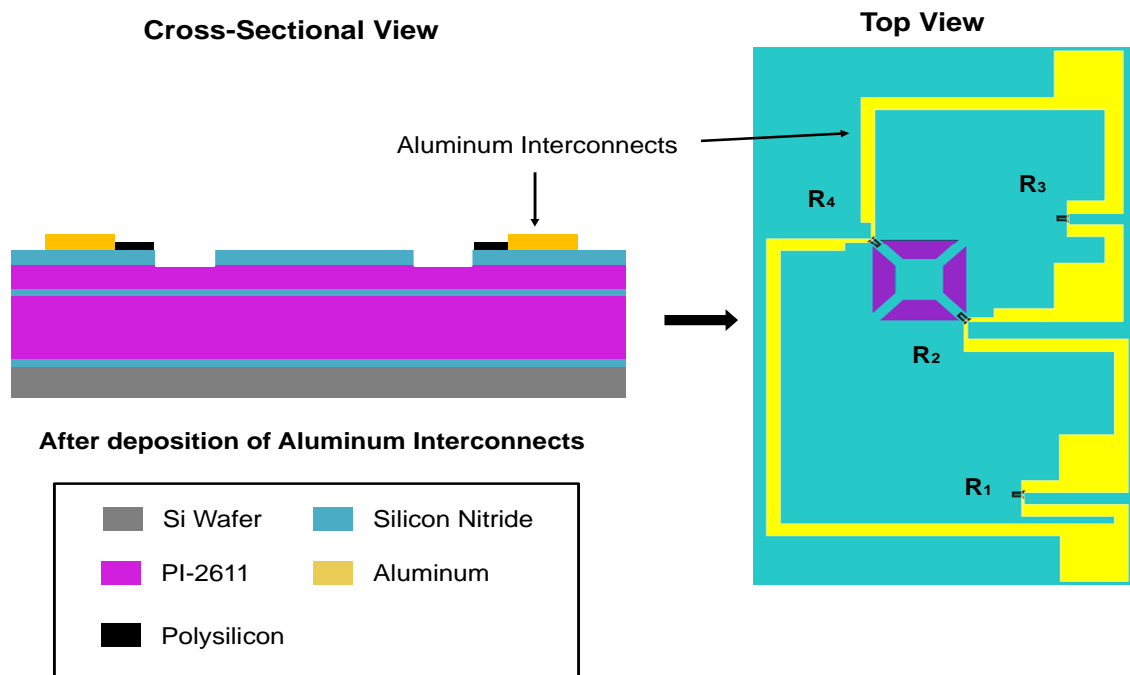


Figure 3.7 Schematic diagram after formation of Al metal interconnects.

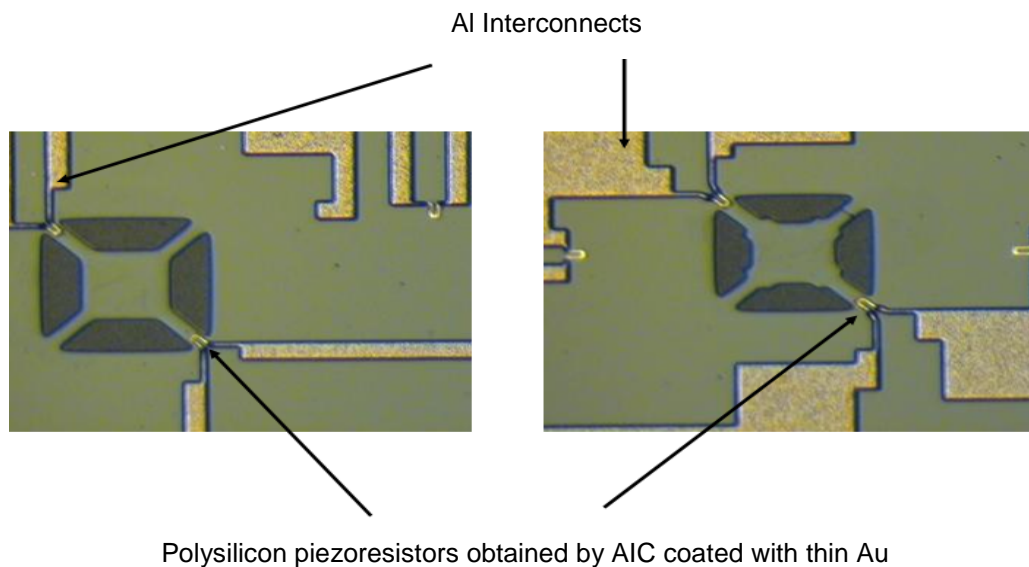


Figure 3.8 Optical microscope images of pressure sensor corresponding to the schematic of Figure 3.7.

3.2.3 Sacrificial Polyimide Layer Removal by Ashing

Ashing was performed on the sample for clean removal of sacrificial polyimide layer as shown in schematic of Figure 3.9. Additionally, to protect the piezoresistors from etching and

oxidation during ashing in O_2 plasma, a thin Au film of thickness $0.05\ \mu m$ was coated on the piezoresistors. This was done by patterning of the piezoresistors as described in Section 3.2.1. Figure 3.8 also shows the optical microscope images of the Au-coated piezoresistors. Figure 3.10 illustrates SEM images of the pressure sensor with the piezoresistors covered with Au before the ashing step.

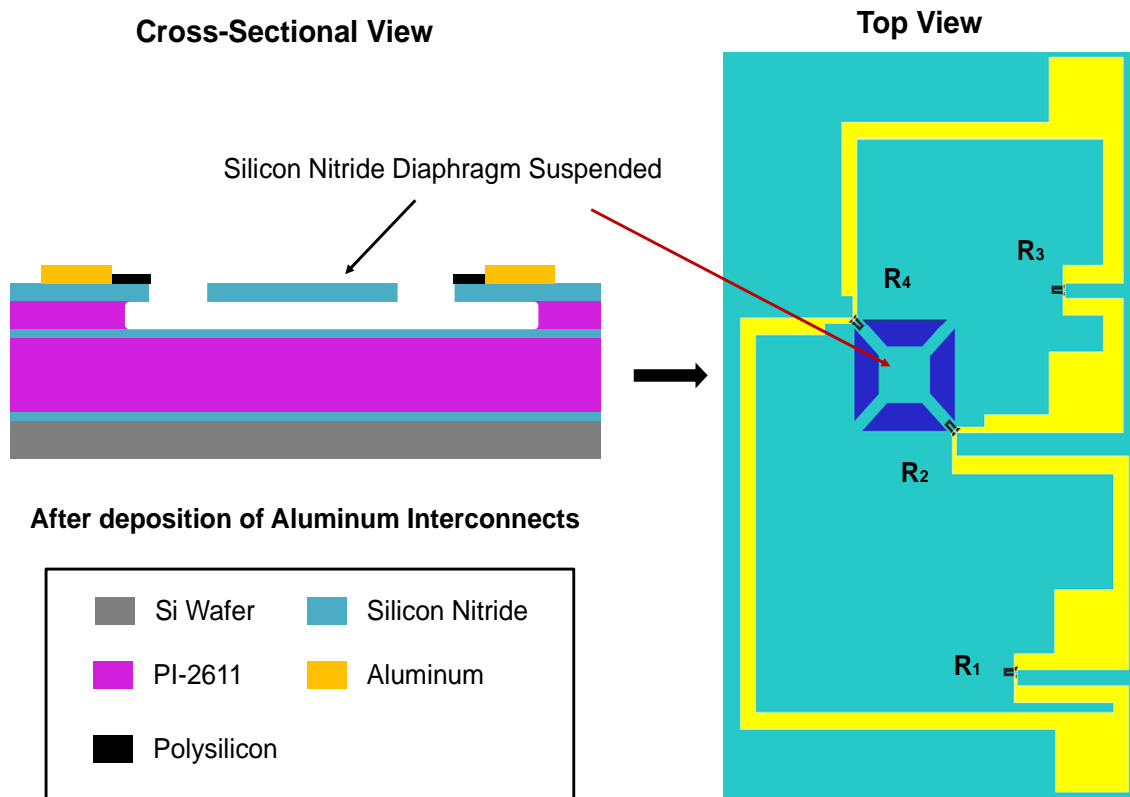


Figure 3.9 Schematic view after etching of sacrificial polyimide layer by ashing in O_2 plasma to suspend the Si_3N_4 diaphragm layer.

Polysilicon piezoresistors obtained by AIC coated with thin Au film

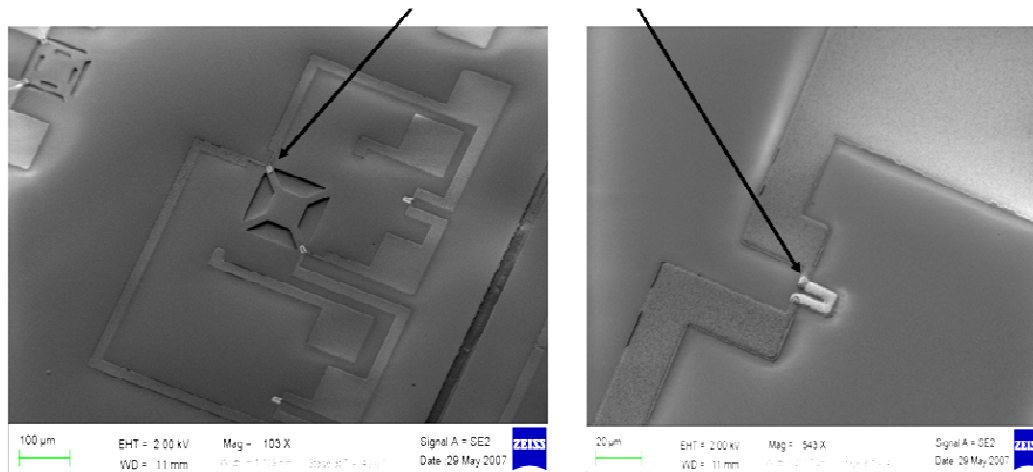


Figure 3.10 SEM images of pressure sensors with polysilicon piezoresistors covered with a thin Au film before ashing.

The sample was later transferred into Diener Asher chamber. Here, the sample was exposed to O_2 plasma at a power of 100 W for several hours. Figure 3.11 displays the optical microscope pictures of some of the pressure sensor structures after ashing for 15 hours and 25 hours respectively.

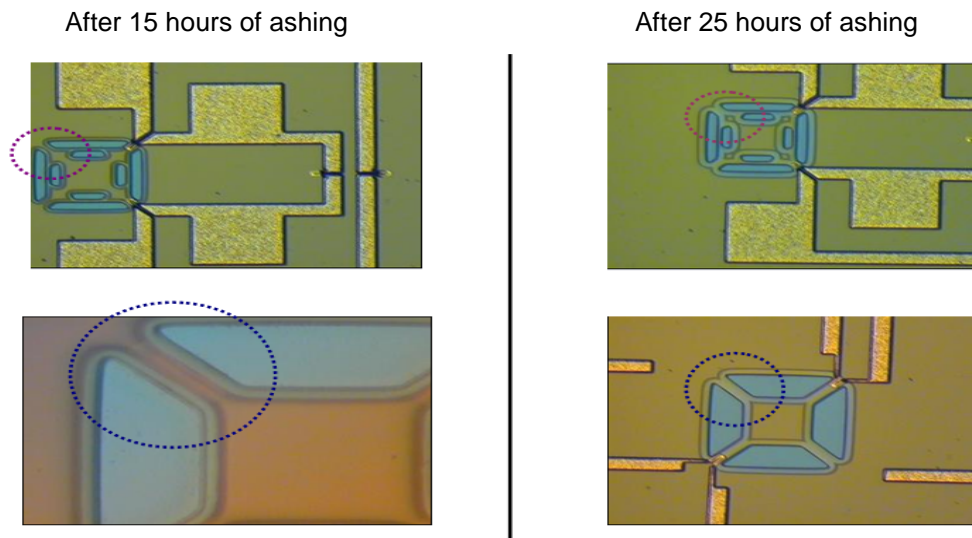


Figure 3.11 Optical microscope images of pressure sensors after 15 hours and 25 hours of ashing in O_2 plasma.

These figures clearly display receding polyimide layer under the Si_3N_4 diaphragm and bridge arm area with increased etch times. However, the etch rates greatly depended on the size and structure of each pressure sensor.

After a total etch time of 45 hours, the sacrificial polyimide layer was completely etched away leaving Si_3N_4 diaphragm layer suspended as shown by the SEM images in Figure 3.12. Here, the removal of sacrificial polyimide layer leads to an undercut as illustrated in the schematic of Figure 3.11. The thin Au layer is subsequently etched in a mixture of dilute $\text{KI}:\text{I}_2$ solution for 10-15 seconds. The sample is held vertically as Au film is etched away in order to prevent any stiction issues. Figure 3.13 shows an SEM image of array of piezoresistive pressure sensors on a flexible substrate after ashing of the sacrificial layer. We observed no stiction issues of the diaphragm in our sensors because of careful designed dimension specs supplemented by a tight process control. The sample is cut into individual dies and bonded onto a chip carrier where individual pressure sensors are wire bonded for extensive electrical and sensor characterization procedures.

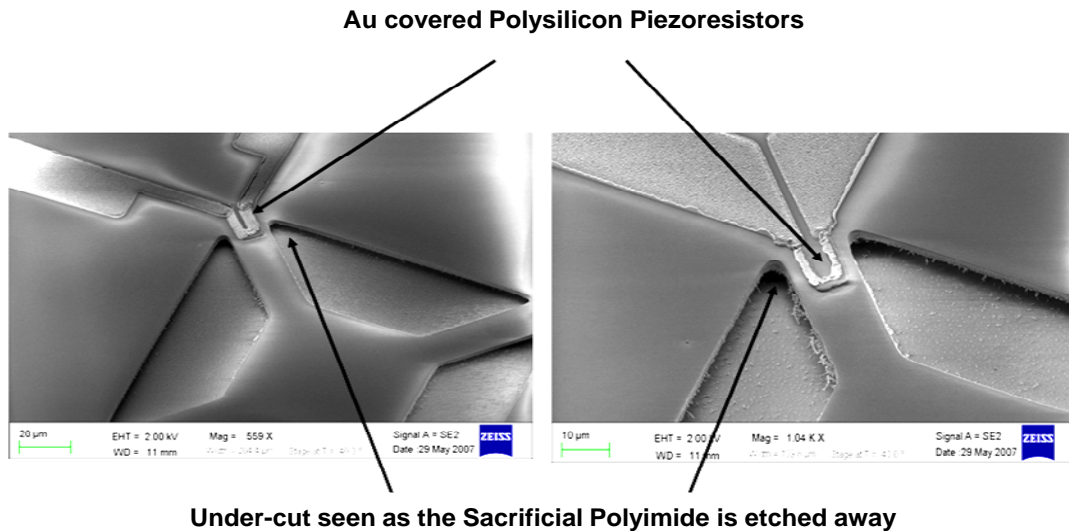


Figure 3.12 SEM images of the pressure sensor with sacrificial polyimide being ashed away.

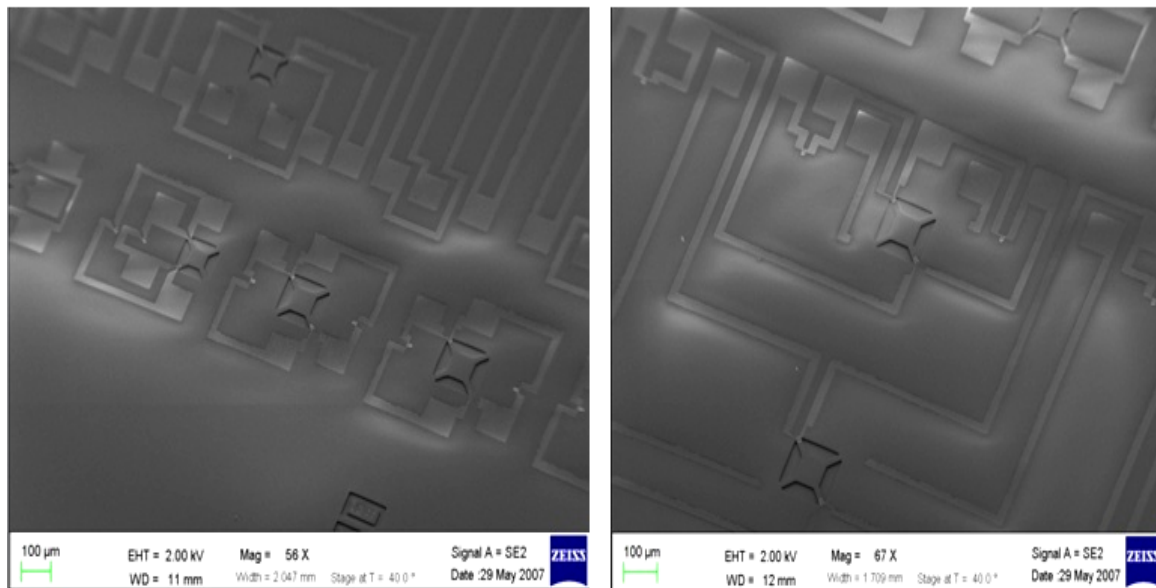


Figure 3.13 Array of piezoresistive pressure sensors of different diaphragm dimensions and piezoresistors shapes.

3.3 Summary

Piezoresistive pressure sensors based on half-Wheatstone bridge circuit were fabricated on flexible polyimide PI-2611 as the substrate layer. Si_3N_4 diaphragm was micromachined using RIE and the resistors were made of polysilicon film obtained by AIC of a-Si at 400 °C. Eventually, the Si_3N_4 diaphragm was suspended by ashing in O_2 plasma of sacrificial polyimide layer thus completing the fabrication process. Various fabrication steps involved in the process were described and illustrated in this Chapter.

CHAPTER 4

CHARACTERIZATION AND ANALYSIS

4.1 Introduction

Piezoresistive pressure sensors fabricated on flexible polyimide substrates employing AIC polysilicon film resistors, as described in Chapter 3 were tested to determine their electrical characteristics and sensitivity (S) with applied pressure, P . The characterization of the sensor was divided into two parts. In the first part, the relative change in resistance ($\Delta R/R_0$) of individual resistors was measured with varying P . This ascertained the piezoresistive property of the polysilicon film obtained by AIC by evaluating its GF. Subsequently, in the second part, ΔV_{OUT} of the half-Wheatstone bridge circuit was measured with applied P . This provided us with the sensitivity values for our fabricated pressure sensors.

The pressure sensor consisted of a suspended Si_3N_4 diaphragm with AIC polysilicon resistors on the bridge arms, connected in half-Wheatstone bridge network, as shown in Figure 1.2 [44]. The dimensions of an individual piezoresistor were as illustrated in Figure 4.1. Change in the applied pressure on the diaphragm brought about a strain change in resistors R_2 and R_4 , the so-called active resistors, which resulted in a change in their corresponding resistances. R_1 and R_3 , the so-called passive resistors, lied outside the diaphragm area and were only used as a reference. Hence, they were unresponsive to the change in pressure. From Eq. (1.15), if all resistors are of equal value, the Wheatstone bridge would be balanced and the output voltage V_{OUT0} would be zero.

Arrays of pressure sensor structures were obtained from the sample in the form of individual dies. These were wire-bonded to electronic chip packages. To obtain S versus P characteristics of the fabricated pressure sensor, all the resistors R_1 , R_2 , R_3 and R_4 were connected electrically in half-Wheatstone bridge configuration as illustrated in Figure 1.2. The schematic and 3-D solid CoventorTM model of one of the sensors is shown in Figure 1.2. When

pressure is applied on the diaphragm, it resulted in a change in strain as experienced by the piezoresistors. This strain was subsequently transformed into a change in resistances (ΔR) of the piezoresistors which were measured by a low-noise, low current I-V measurement setup. The pressure sensor was designed for tactile sensing applications in the range of 0-50 kPa. The change in resistances brings about a change in overall output voltage of the sensor by ΔV_{OUT} given by Eq. (1.16).

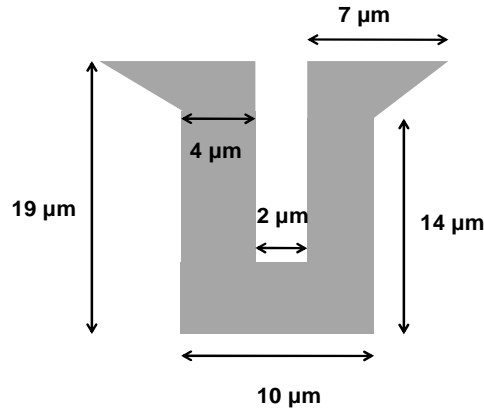


Figure 4.1 Piezoresistor dimensions [16].

4.1.1 Various Low Pressure Application Methods and Challenges

Previous literature on characterization of tactile sensors on micromachined diaphragms focused on the whole sensor or array enclosed by an elastomer mesa structure [34, 118, 119, 120] to ensure uniform application of the load on the whole diaphragm surface. Then, by using a load-cell coupled to a probe-tip, normal forces were exerted on to the diaphragm. The use of an elastomer helps increase the contact surface area of the probe-tip on the sensor diaphragm and transforms the applied load to stress in a homogenous manner. Since the elastomer also absorbs part of the applied load, the elastomer top surface experiences a much larger load when compared to loads experienced by the bare diaphragm surface below. This facilitates the use of a larger load-cell thereby increasing the applied force range and therefore the probe tip radii. Our case, however, differs from these in that the sensor diaphragm cannot be protected

with an elastomer due to the specific use, thus necessitating application of a very small amount of force with high accuracy for sensor calibration.

Valdastri et al. [121] summarized various multi-component force sensors with their dimensions and characterization methods along with their achieved applied force ranges. The sensing element sizes in the above cases were in the range of few hundreds of micrometers to millimeters. Our fabricated sensor structures [17, 46] have diaphragm sizes ranging from $40 \times 40 \mu\text{m}^2$ to $80 \times 80 \mu\text{m}^2$ and a maximum deflection of $1.5 \mu\text{m}$. They consist of a suspended $1.5 \mu\text{m}$ thick silicon nitride (Si_3N_4) diaphragm with piezoresistive polysilicon resistors on the bridge arms connecting the diaphragm to the silicon substrate, in half-Wheatstone bridge configuration [72]. The small size of the sensors together with their very high sensitivity required a new characterization set-up capable of applying small amounts of controlled force at precise locations.

The use of a surface profiler as described in [122] for testing tactile sensors was also considered. Their structure consisted of a square shuttle plate of dimensions $200 \times 200 \mu\text{m}^2$, which was 2.5 times the size of the suspended diaphragm we intended to probe. Linear forces up to $200 \mu\text{N}$ were achieved by the authors, with resolution of $40 \mu\text{N}$. However, issues with smaller structure size and load range (few tens of μN) restrictions inhibited its use as the characterization tool. Another method to measure the applied load is by using electronic weight scale capable of sub-milligram resolution instead of a load-cell. This measures the change in overall weight increase as the sensor is probed in the perpendicular direction.

Consideration was also given to another method using a very sensitive electronic weighing scale described in [123] to probe sensing elements of dimensions $250 \times 250 \mu\text{m}^2$. The force ranges obtained by this method were $0.1\text{-}0.3 \text{ N}$. However, the use of this set-up was again limited by our relatively smaller diaphragm size, and the radius of the probe-tip. It would have also required a very stringent weight calibration step each time the reading is taken in-order to account for any drift and vibrations in the surroundings.

4.1.2 Atomic Force Microscope (AFM) As Pressure Sensor Characterization Tool

Use of AFM in the contact mode and studying of sample / probe-tip interactions through a force plot for sample hardness and indentation have been previously documented [124, 125]. We employed similar principles to characterize our pressure/force tactile sensor. Force plots present a graphical view of the probe tip and sample surface interactions as the tip proceeds to scan the surface. This representation provides a prediction of the sample hardness, elasticity and adhesion characteristics. It is also used to derive and control the contact force between the probe-tip and the sample. The contact force F (N) is given by Hooke's Law in Eq. 4.1 as

$$F = -k \cdot d \quad (4.1)$$

where, k (N/m) is the cantilever spring constant, and d (m) is the deflection of the cantilever. Since the probe-tip deflection can be accurately controlled by the AFM, smaller loads in the range of nN to μ N can be applied [126, 127]. AFM was used to measure:

- (i) Individual piezoresistor's $\Delta R/R_0$ change with applied P , to estimate GF, where R_0 is the original value of resistance for either R_1 , R_2 , R_3 or R_4 .
- (ii) Pressure sensor sensitivity at low pressure ranges.

4.1.3 Load-Cell As Pressure Sensor Characterization Tool

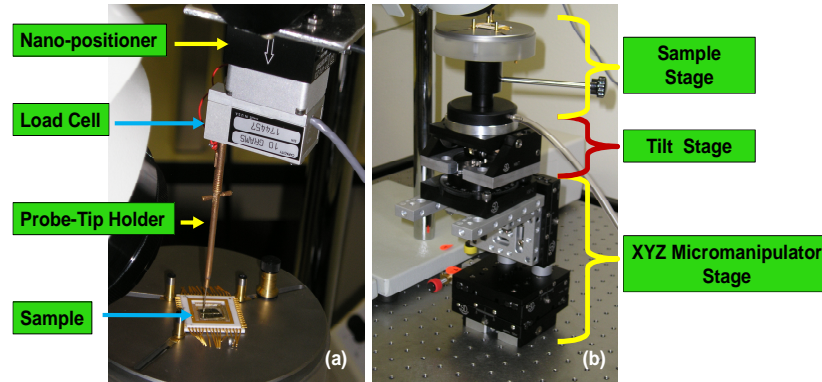


Figure 4.2 Pressure sensor characterization set-up (a) load-cell and (b) XYZ stage.

A test set-up employing a load-cell was also considered as shown in Figure 4.2 (a). It was designed and built, based on [118, 119, 120, 121]. The system consisted of a tensile mono-axial 10 gm load-cell (GSO-10 from Transducers Techniques, Inc., USA) with a resolution of \pm

49 μN , and a customized probe-tip holder to facilitate the use of probe-tips with varying radius. This was attached to a PI-620 ZCD Nano-positioner (Physik Instrumente, GmbH, Germany) with 0-50 μm Z-axis travel and a minimum resolution of 0.2 nm. A micromanipulator stage (Micromanipulator, Inc., USA) capable of moving in X, Y and Z-directions for coarse movement and a rotary tilt stage to tilt the sample from 0° - 45° were utilized to hold the sample as shown in Figure 4.2 (b). In order to achieve pressure values down to the range of 0-50 kPa, the load-cell resolution was required to be approximately between few tens of nN to few mN accuracy. Additionally, in order to apply such low pressures on the diaphragm surface, it was required to use probe-tips with radius greater than 100 μm , as probe-tips with larger radius of curvature (r_p) result in low pressures as their contact area increases.

However, due to the unavailability of an accurate, inexpensive, compact load-cell with a nN range load discernability for low pressure ranges and due to our sensor diaphragm size restrictions, in the present work load-cell was only used for sensor characterization at high pressure ranges.

4.2 AFM Based Characterization Set-up

4.2.1 Effective Spring Constant (k_{eff})

Typically the AFM probe-tip used for surface imaging consists of a micromachined pyramidal shaped tip with a nominal radius of curvature of 10-50 nm [128, 129]. In this case, the probe-tip contact force would be distributed in an area much smaller than the suspended Si_3N_4 diaphragm area of $80 \times 80 \mu\text{m}^2$, as per the design specifications described in [16, 17]. Therefore, to effectively increase the contact area of the probe-tip on the diaphragm surface, the tip was modified by attaching a spherical soda-lime glass particle of radius 25 μm to its end. Since soda-lime glass is a softer material compared to Si_3N_4 , this reduced damage to the diaphragm surface and avoided undesirable indentations during contact. It also ensured uniform application of the load over a larger area of the diaphragm surface.

In order to calculate the contact force accurately from Eq. (4.1), first the effective spring constant of the probe-tip with the attached particle was determined. In our case the probe-tip

consisted of a rectangular silicon cantilever of 90 μm length, 35 μm width and 2 μm thickness, coated with a very thin layer of aluminum (Al) on the backside. The nominal k and resonant frequency, f_{r0} values of 14 N/m and 315 kHz, respectively, were specified by the manufacturer [130]. A spherical borosilicate glass particle with a 50 μm diameter was attached on this cantilever, as shown in Figure 4.3 (a). The particle size selection was based on a compromise between the maximum pressure that can be applied without damage to the diaphragm and the tip-deflection sensitivity required to obtain measurable change in the piezoresistor resistance due to strain induced in the diaphragm.

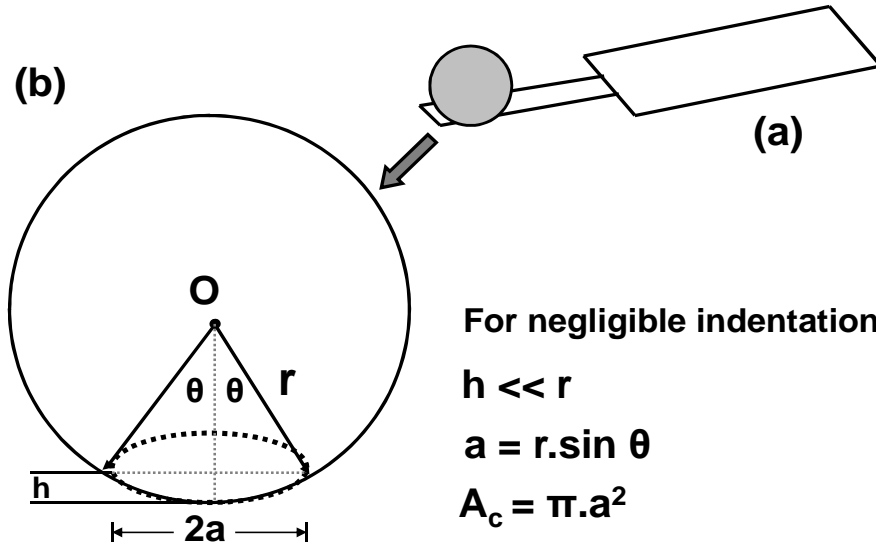


Figure 4.3 Modified AFM probe-tip with (a) spherical particle of radius 25 μm attached to the rectangular cantilever, (b) area of contact estimation between the probe-tip and the diaphragm surface [17].

The modified spring constant, k^1 was calculated using the added mass method [131]:

$$k^1 = \frac{4 \cdot \pi^2 \cdot M}{\left(\left[\frac{1}{f_{r1}^2} - \frac{1}{f_{r0}^2} \right] \right)} \quad (4.2)$$

Here, M (kg) is the mass of the rectangular Si cantilever with no particle attached, f_{r0} (= 315 kHz) is the resonant frequency of the cantilever without the attached particle. f_{r1} (= 209 kHz) is

the resonant frequency for the cantilever with the spherical particle attached, measured by the AFM during tuning in tapping mode. The value of k^l was thus calculated to be 11.01 N/m from Eq. (4.2). The tilt angle of 12° between the probe-tip and the horizontal had to be also taken into account [132], giving the k_{eff} of 11.51 N/m:

$$k_{eff} = \frac{k^l}{\cos^2(12^\circ)} \quad (4.3)$$

This calculation, however, assumed that the particle was a perfect sphere attached to the tip of the cantilever, and any change on the cantilever resonant frequency due to the exact position of the particle on the tip was considered negligible [133, 134]. The f_{r1} value and hence the spring constant was found to be varying from one probe-tip to other as it was greatly sensitive to small variations in the size, shape, mass and placement of the spherical particle on the rectangular cantilever. Additionally, the spherical particle was attached to the cantilever by some kind of epoxy or glue which would also change the resonant frequency due to variation in the amount of glue used from one probe-tip to the other.

4.2.2 Contact Force

Veeco Instruments' Dimension 5000 AFM with NanoScope IIIA controller was used in advanced contact mode to calculate the contact force, F_c (N) [135]:

$$F_c = k_{eff} \cdot S_v \cdot V_t \quad (4.4)$$

where S_v (nm/V) is the deflection sensitivity of the probe-tip on the sample given by the slope of the force-plot as shown in Figure 4.4, and V_t (V) is the applied trigger voltage.

The parameter S_v relates the deflection voltage applied on the tip to the amount of deflection the tip experiences in nanometers. Eq. (4.4) expresses the force applied on the diaphragm as a function of varying trigger voltage.

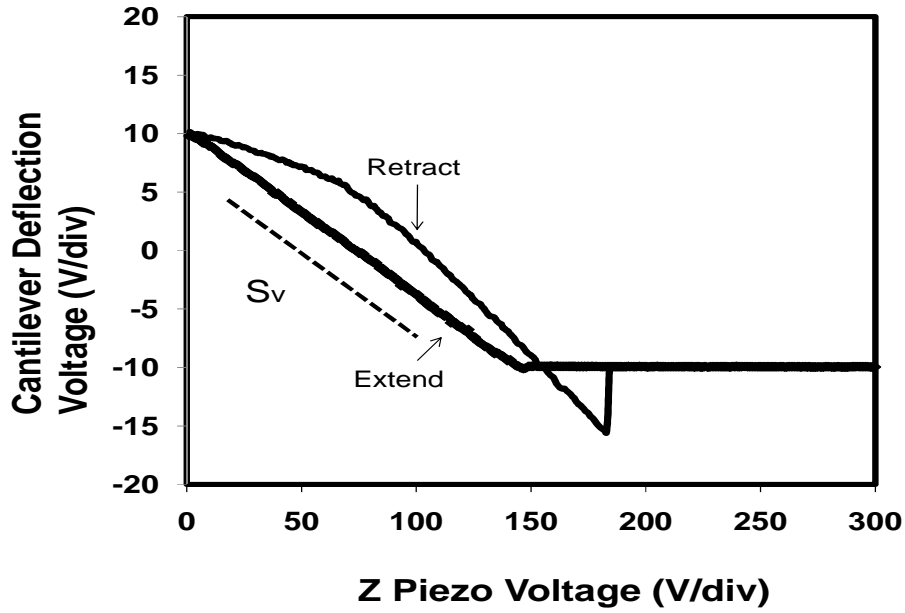


Figure 4.4 Force plot for AFM in contact mode. The slope gives S_v (nm/V).

4.2.3 Contact Area and Tip-Sample Interactions

Figure 4.3(b) is the graphical representation of the assumed contact area, A_c between the probe-tip and the Si_3N_4 diaphragm surface. We assumed that there was negligible indentation occurring at the diaphragm surface due to the probe-tip. In addition, the interactions between the probe-tip and the diaphragm surface were considered as elastic in nature. If d was the maximum deflection of the diaphragm for certain force, we estimated the solid angle at the center O made by the cone as:

$$\cos \theta = \left(\frac{r-d}{r} \right) \quad (4.5)$$

The area of the probe tip, A_c in contact with the diaphragm is then:

$$A_c = \pi \cdot r^2 \cdot \sin^2 \theta \quad (4.6)$$

The pressure, P (Pa) exerted by the probe-tip on the Si_3N_4 diaphragm surface is then given by:

$$P = \frac{F_c}{A_c} \quad (4.7)$$

The fractional change in the resistance of the piezoresistors due to change in applied pressure, $(\Delta R/R_0) \%$ was obtained from an I-V measurement setup during the AFM engage step and was plotted against applied pressure, P (Pa).

4.2.4 Experimental Procedure

A die containing an array of pressure sensor structures (refer to APPENDIX B) shown in Figure 4.5 was diced from the original sample and was wire-bonded to individual chip carrier packages. The resistors were electrically isolated from each other by scratching the Al interconnects between the resistors using a micromanipulator probe-tip. I-V characteristics before pressure application were carried out using a semiconductor analyzer Agilent 4155 C.

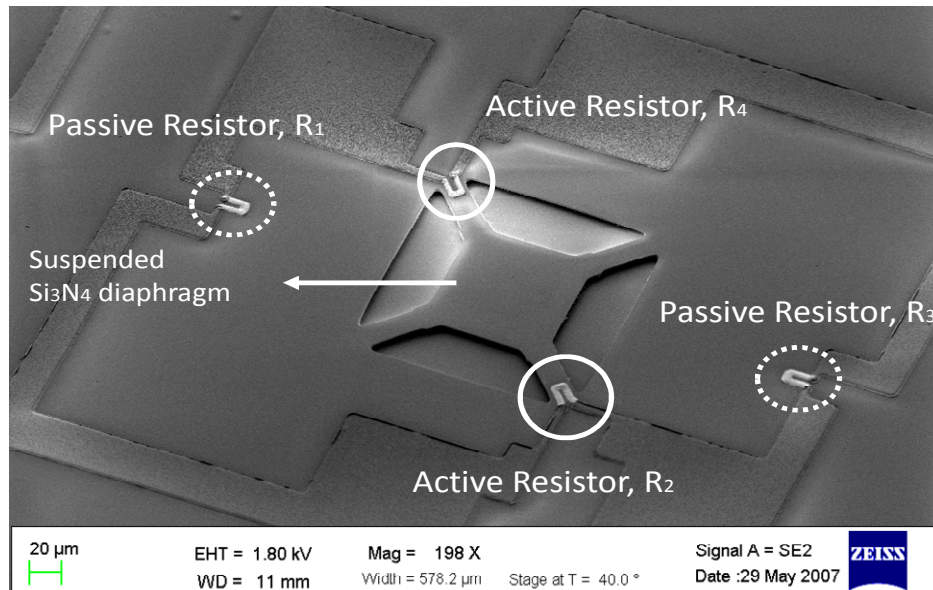


Figure 4.5 SEM image of Device#1 with $80 \times 80 \mu\text{m}^2$ Si₃N₄ diaphragm, showing active resistors and passive resistors connected in a half-Wheatstone bridge configuration.

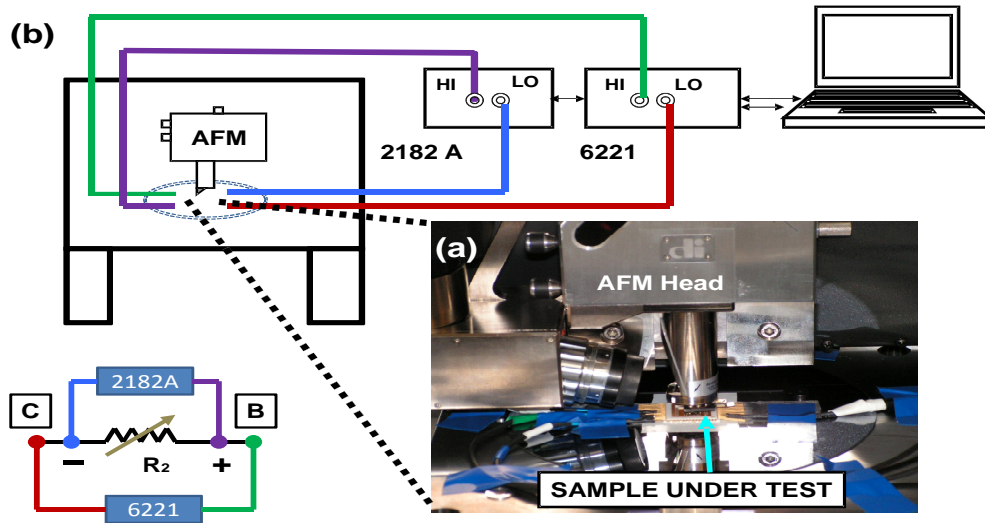


Figure 4.6 (a) Device packaged and placed under the AFM probe-tip for pressure characterization, (b) Schematic of the I-V setup for 4-wire resistance measurements for resistor R_2 across device contact pads B and C corresponding to Figure 1.2 (a).

The bonded package was then glued onto a flat 150 mm bare Si wafer which acted as a base for mechanical support and was held on the AFM stage by vacuum. Care was taken to ensure that the sample was strongly held on to the base wafer restricting any movement as shown in Figure 4.6 (a). The probe-tip was brought close to the diaphragm surface. IV measurements before engaging the probe-tip were taken using the low-noise delta mode IV set-up [136]. The schematic for electrical connections is as shown in Figure 4.6 (b) which consisted of combination of a Keithley low-noise Current Source 6221 and Keithley Nano-Voltmeter 2182A, controlled by a computer. The resistors to be tested for their $(\Delta R/R_0)$ were connected in four-wire resistance measurement set-up as illustrated in Figure 4.6. The current was swept and corresponding voltages were measured. The resistance at zero applied pressure, R_0 of the piezoresistors before engaging the AFM probe-tip was obtained by taking the average of eleven such readings. A trigger voltage, $V_t (= 1V)$ was used for the initial measurement. The probe-tip was then engaged on the center of the sample surface and the scan controlling parameters such as scan size and set-point were adjusted to obtain a force-plot. The sensitivity factor, S was noted down for each trigger voltage value. The corresponding force values were obtained from the force-plot using Eq. (4.4). During the force-plot capture, I-V measurements were

carried out simultaneously to determine the change in the resistance due to applied load. V_t was varied in steps of 1 V for each engagement (non-continuous). Care was taken not to disturb the probe-tip contact location on the diaphragm surface for each engagement step as we wanted to place the probe-tip approximately at the center of each diaphragm. APPENDIX C gives the procedure and settings for AFM used during the characterization.

4.2.5 AIC Polysilicon Film Characterization

In the first set of experiments namely EXPERIMENT #1, % $(\Delta R/R_0)$ was measured on R_2 with varying P for pressure sensor structures named Device#1 and Device#2 (refer to APPENDIX B). These devices employed polysilicon film resistors obtained at annealing temperature of 500 °C and anneal time of 90 minutes. This was done to study the effect of diaphragm area on the $(\Delta R/R_0)$ and to estimate the GF of the polysilicon film obtained by AIC. Additional measurements were performed on R_2 of Device#1, evaluating the effect of probe-tip engagement on the change in its resistance. In the present case namely EXPERIMENT #2, the pressure was applied on the diaphragm without lifting the probe-tip. The probe-tip was engaged only once (continuous case) and the pressure was varied in each step by increasing V_t by 1V without disengaging the AFM. Corresponding force-plots were obtained and relative change in resistance $(\Delta R/R_0)$ was measured.

In the third set of experiments termed as EXPERIMENT #3, pressure sensor structure named Device#3 (refer to APPENDIX B) was used to characterize % $(\Delta R/R_0)$ with P for R_2 with polysilicon films obtained at annealing temperatures of 500 °C and 400 °C for constant anneal time of 90 minutes. This experiment was to compare the effect of anneal profile on the response of the pressure sensor.

4.2.5.1 EXPERIMENT #1 – Gauge Factor

Two fabricated pressure sensor structures, referred to as Device#1 and Device#2 here [17], were considered with varying Si_3N_4 diaphragm sizes of 80 x 80 μm^2 and 70 x 70 μm^2 , respectively. The pressure sensor consisted of a suspended Si_3N_4 diaphragm with AIC polysilicon [117] resistors on the bridge arms, connected in half-Wheatstone bridge network, as

shown in Figure 4.5. The dimensions of an individual piezoresistor are as illustrated in Figure 4.1. Only resistor R_2 in each of pressure sensor structure was considered for current analysis.

The dc current was swept from $-0.5 \mu\text{A}$ to $+0.5 \mu\text{A}$ using Agilent 4155C and corresponding voltages were plotted as in Figure 4.7. Average resistance value of $17.6 \text{ k}\Omega$ and $10.772 \text{ k}\Omega$ were measured, respectively. Before proceeding to pressure characterization using an AFM, a DC current in the range of $-0.1 \mu\text{A}$ to $+0.1 \mu\text{A}$ was applied with the Keithley Delta-Mode System described earlier. The measured resistance with no applied pressure was $R_{0(\text{Device}\#1)}=18.465 \text{ k}\Omega$ and $R_{0(\text{Device}\#2)}=10.412 \text{ k}\Omega$. Pressure was then applied on the diaphragm by engaging the AFM on its surface, as described in the previous section. The measured resistance value for each trigger voltage was denoted as R_{Loaded} . Then the relative change in resistance due to applied pressure was calculated as:

$$\frac{\Delta R}{R_0} = \frac{|R_{\text{Loaded}} - R_0|}{R_0} \quad (4.8)$$

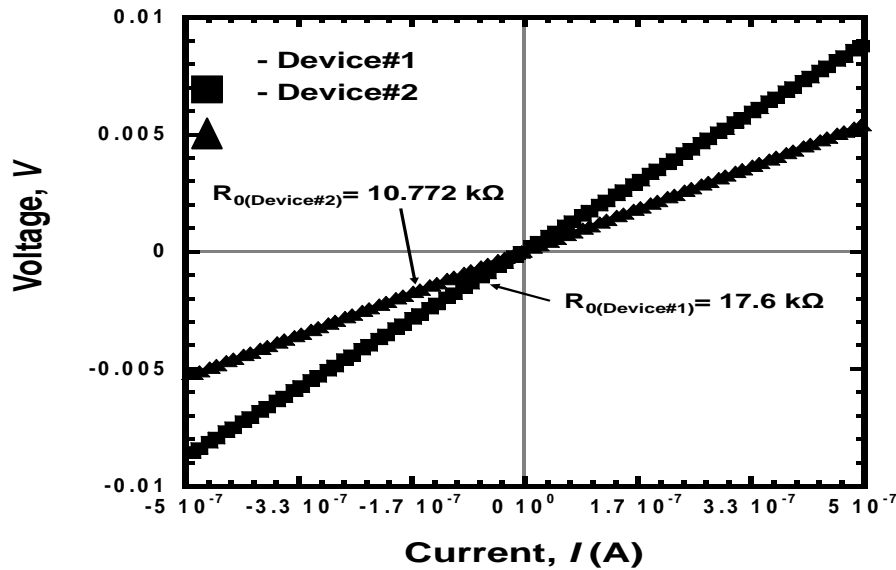


Figure 4.7 IV Characteristics for active resistor R_2 of Device#1 and Device#2 using Agilent 4155C for no applied pressure.

The maximum displacement d for Device#1 and Device #2 were measured to be $0.43 \mu\text{m}$ and $0.183 \mu\text{m}$ corresponding to force values of $4.94 \mu\text{N}$ and $2.12 \mu\text{N}$ respectively. From Eq.

(4.5) we calculated the θ values of 11° and 7° for Device#1 and Device#2, respectively. For A_c calculations, we have assumed that the Si_3N_4 diaphragm surface conforms to the spherical particle during contact.

Corresponding A_c values of $71.45 (\mu\text{m})^2$ and $29.15 (\mu\text{m})^2$ were respectively calculated for Device#1 and Device#2 from Eq. (4.6). Relative change in the resistance % $(\Delta R/R_0)$ was measured and plotted for corresponding pressure values calculated from Eq. (4.7) for each trigger voltage ranging from 1V to 10 V.

The relative change in resistance varied from 0.02% to 0.97% for pressure ranges of 6.3 kPa to 70 kPa as shown in Figure 4.8 for Device#1. Similarly, for Device#2, this change varied from 0.18 % to 1.31 % for pressure ranges of 8.9 kPa to 73 kPa. The sensitivity $[(\Delta R/R_0) / P]$ was $0.162 \times 10^{-3} \text{ kPa}^{-1}$ for Device#1 and $0.185 \times 10^{-3} \text{ kPa}^{-1}$ for Device#2.

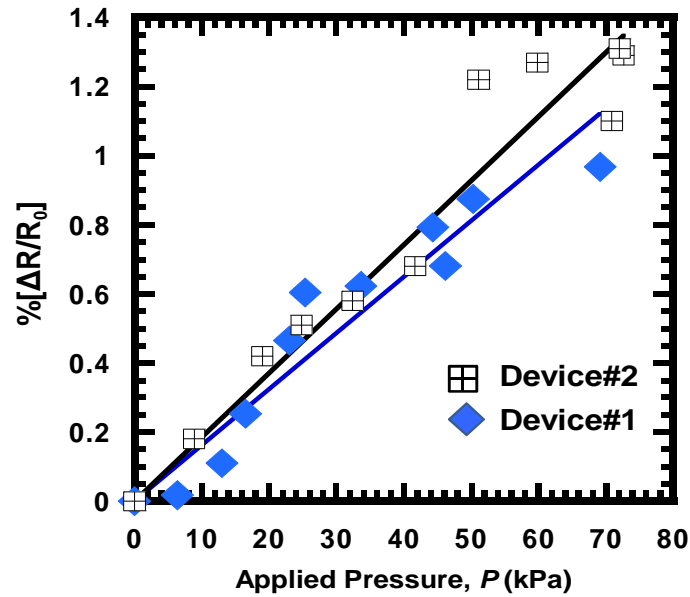


Figure 4.8 Plot of % $[\Delta R/R_0]$ versus applied pressure, P (kPa) for non-continuous engagement case for Device#1 and Device#2.

The piezoresistive GF of the polysilicon film was calculated using the measured $\Delta R/R_0$ and the average strain ϵ_{avg} experienced by the piezoresistors [16]:

$$GF = \frac{1}{\varepsilon_{avg}} \left[\frac{\Delta R}{R_0} \right] \quad (4.9)$$

Three dimensional solid models of Device#1 and Device#2 were virtually “built” in CoventorWare™ with suspended Si₃N₄ diaphragms holding two active polysilicon piezoresistors on the bridge arms. To simulate the AFM tip, a uniform pressure of 70 kPa was applied on a patch of circular area with a 9.6 μm diameter for Device#1 and 6.1 μm diameter for Device#2 respectively, corresponding to their individual A_c at the center of the diaphragm. In order to calculate ε_{avg}, the piezoresistor area was divided into three regions as shown Figure 4.9.

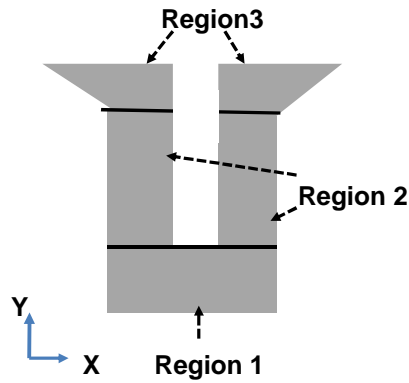


Figure 4.9 Different regions of the piezoresistor used for average strain computation.

Strain induced in these regions was extracted using strain components along X and Y directions. The resultant strain values for each region were integrated to obtain the total strain induced in the piezoresistor. This value was then divided by the total piezoresistor area to obtain ε_{avg} given by:

$$\varepsilon_{avg} = \frac{\iint (\varepsilon_{xx} + \varepsilon_{yy}) dXdY}{\iint dXdY} \quad (4.10)$$

The computed Mises stress distributions are illustrated in Figure 4.10. The ΔR/R₀ values obtained from the fitted lines to the data in Figure 4.8 were used in conjunction with the calculated ε_{avg} to find GF from Eq. (4.9). Corresponding GF values were 6.6 for Device#1 and 11.7 for Device#2, respectively.

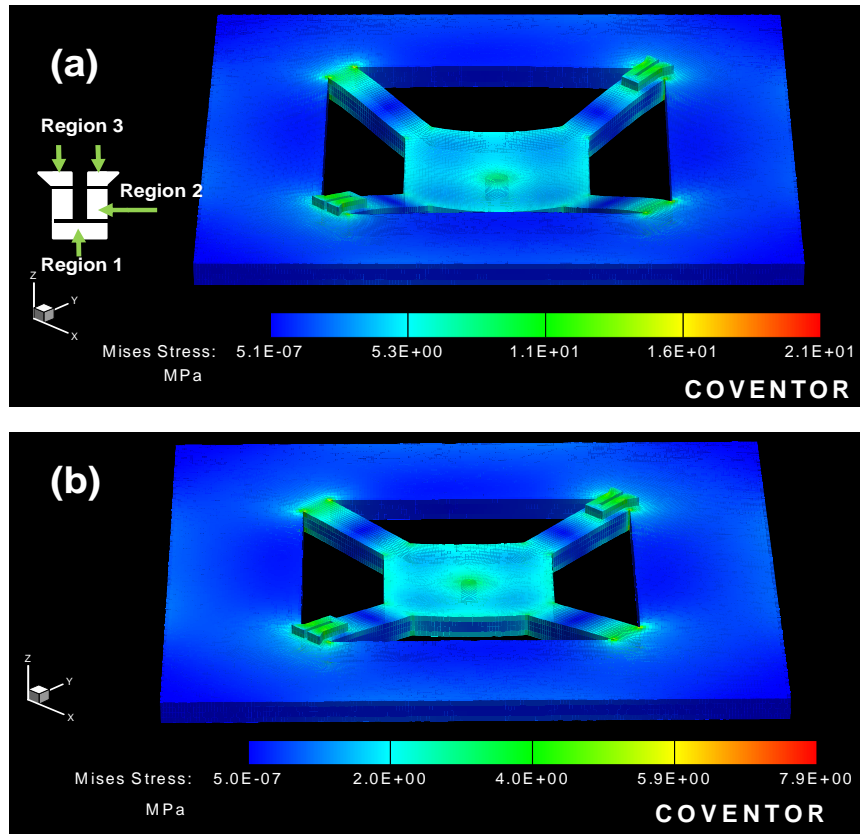


Figure 4.10 COVENTOR™ simulation showing Mises stress distribution for (a) Device#1 and (b) Device#2 when a uniform pressure of 70 kPa is applied at the center of each diaphragm.

It should be noted that this is a rough estimation of the gauge factor. The actual piezoresistive gauge factor of polysilicon depends on the primary crystallographic direction of the grains and as such will change according to the piezoresistor's orientation on the wafer. In addition, the calculation above assumes the placement of the probe-tip to be exactly at the center of the diaphragm, whereas experimentally there might be an offset which would lead to a variation in the actual strain experienced by the piezoresistors. Another reason for observed variations in polysilicon gauge factors was its dependence on the device geometry (the size and thicknesses of the diaphragms and the bridge arms), and material properties of the diaphragm (Young's modulus). For our simulations, we assumed the Young's Modulus, E for rf sputtered Si_3N_4 as 100 GPa [137]. Our simulation results showed that Device#1 with $80 \times 80 \mu\text{m}^2$

diaphragm displaced greater than Device#2 with $70 \times 70 \mu\text{m}^2$ diaphragm for constant applied pressure of 70 kPa as observed experimentally.

From the above simulations ϵ_{avg} values of 1.72×10^{-3} and 1.11×10^{-3} were calculated for piezoresistor R_2 of area $1.04 \times 10^2 (\mu\text{m})^2$ for Device #1 and Device #2 respectively. Both experimental and simulation results showed that Device#2 was more sensitive to change in pressure than Device#1 even though its diaphragm displacement was lower. Since the smaller diaphragm in Device#2 was mechanically stiffer than Device #1 diaphragm, it displaced less and had lesser ϵ_{avg} induced in its piezoresistors, hence higher GF.

4.2.5.2 EXPERIMENT #2 – Modes of Operation

In the second set of experiments, where the probe tip was continuously engaged on the diaphragm, $\%(\Delta R/R_0)$ exhibited a larger spread for R_2 of Device#1 as shown in Figure 4.11, although the general trend was similar to that found in the previous (non-continuous) experiment, where the tip engagement was not continuous.

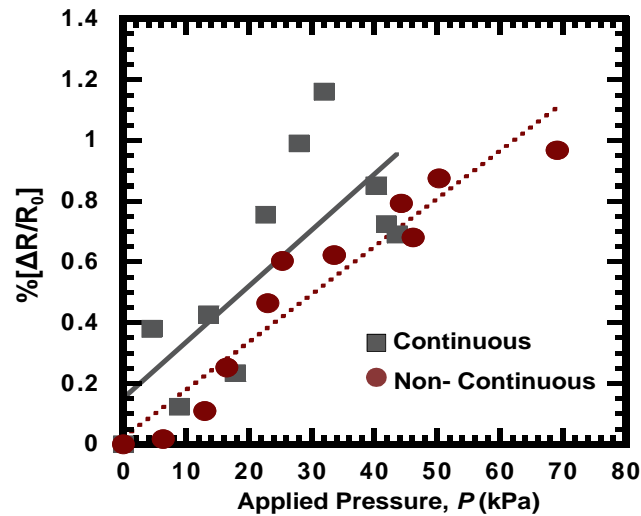


Figure 4.11 Plot comparing $\% [\Delta R/R_0]$ versus applied pressure, P (kPa) for Device#1 for continuous engagement and non-continuous case.

Since k and V_t were constant in both continuous engagement and non-continuous cases, it is possible to compare the S_v values for Device#1 as depicted in Table 4.1. The S values obtained for continuous case were quite close to each other as the probe-tip always

interacted with a particular area of contact on the diaphragm surface. However, for the non-continuous case, during each engagement step there could be the possibility of small offsets in the area of contact. This would cause a small source of error in measuring the pressure.

Table 4.1 Comparison of S_v values for Device#1 for continuous and non- continuous tip engagement

Trigger Voltage V_t (V)	Sensitivity Factor S_v (nm/V)	
	Continuous Engagement	Non-Continuous Engagement
1	28	32.25
2	27.66	27.96
3	28.11	26.5
4	27.67	26.5
5	28.14	23.79
6	28.96	22.74
7	28.35	23.2
8	31.22	23.37
9	28.87	23.16
10	27.07	23.8

As our main goal was to substantiate the use of AFM as a characterization tool for pressure sensors of dimensions less than 100 μm , it was essential to attain measureable $\Delta R/R_0$ values down to few of kPa. Our results showed considerable and linear $\Delta R/R_0$ change at low pressure ranges for both cases of continuous and non-continuous engagement of the AFM probe-tip.

4.2.5.3 EXPERIMENT #3 – Anneal Temperature

For the pressure sensor Device#3 depicted in Figure 4.12, and for a piezoresistor shape similar to Figure 4.1, IV characteristics of R_2 obtained using Agilent 4155C are given in Figure 4.13. The measured resistances were 17.8 k Ω and 21.3 k Ω , respectively, for 500 °C and 400 °C anneal temperatures, both for 90 minutes.

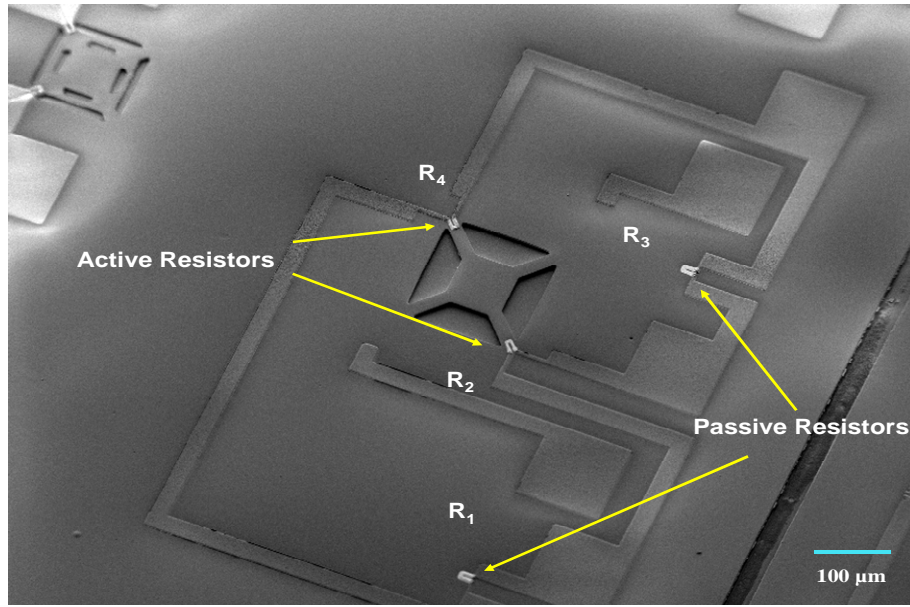


Figure 4.12 SEM image of pressure sensor Device#3 with Si_3N_4 diaphragm size of $80 \times 80 \mu\text{m}^2$.

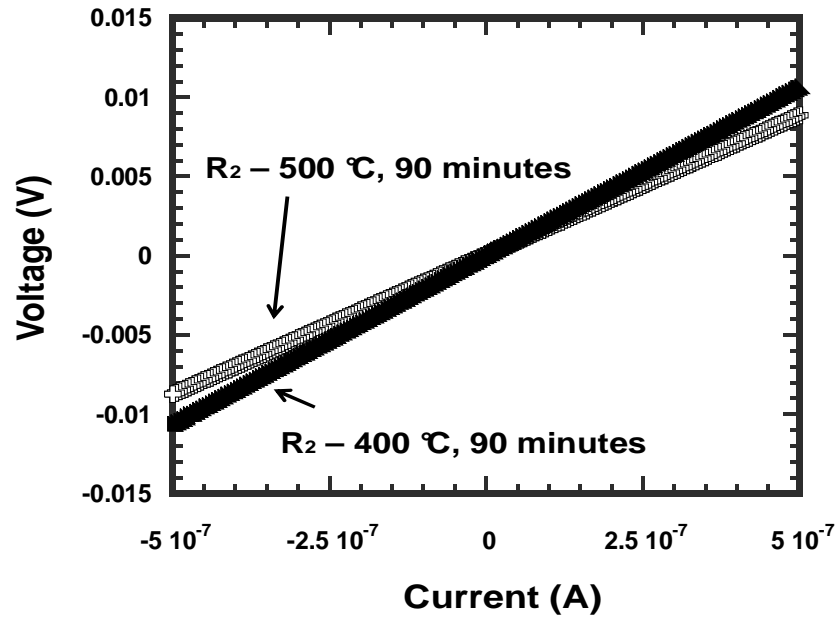


Figure 4.13 IV characteristics for the R₂ polysilicon piezoresistor obtained by annealing for 90 minutes at 400 °C and 500 °C.

An experimental procedure similar to the one described in Section 4.2.4 was carried out. A_c of the spherical particle touching the sample was estimated by assuming a spheroid with an angle θ of 11° . In this case normal pressures ranging from 5 kPa to 45 kPa were obtained for

the diaphragm displacements between 0.03 μm to 0.28 μm . Once the force-plots were acquired for particular V_t values, a constant DC current ranging from -5.0 μA to +5.0 μA was simultaneously sourced through the resistor R_2 . Corresponding change in its resistance was measured using the set-up described in Figure 4.6.

R_0 value for the resistor R_2 measured from the set-up before the application of the force was $R_{02(500\text{ }^\circ\text{C})}$ (= 18.103 k Ω). Figure 4.14 illustrates % $[\Delta R/R_0]$ versus applied pressure, P (kPa) for the active resistor R_2 . Passive resistor R_3 was not affected by the AFM probe tip as it is not on the diaphragm.

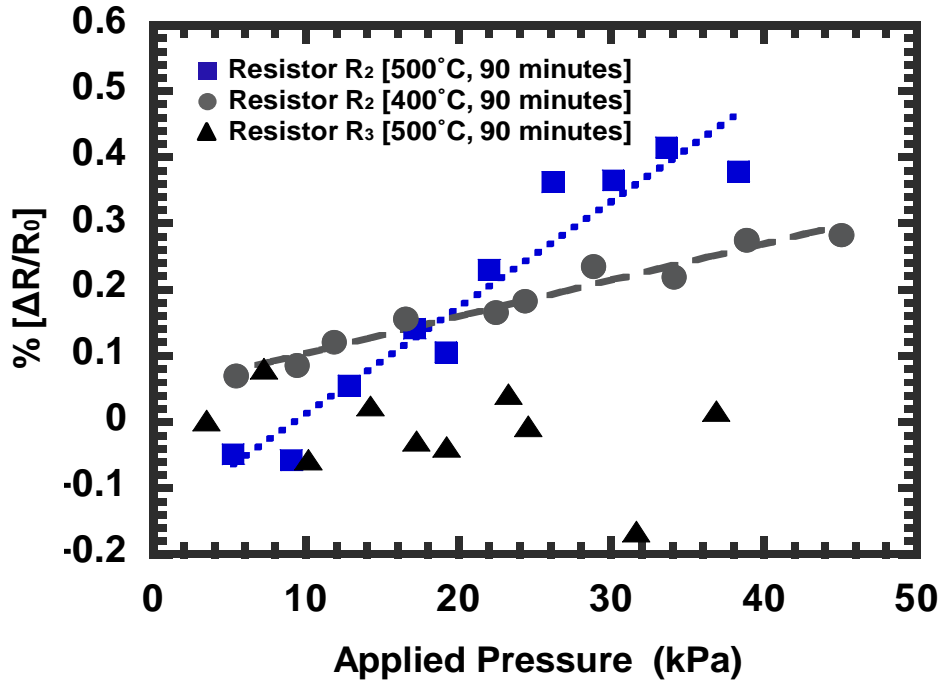


Figure 4.14 % $[\Delta R/R]$ with applied pressure, P (kPa) for R_2 polysilicon films obtained by AIC with annealing temperatures of 400 and 500 $^\circ\text{C}$, compared to the passive resistor R_3 .

The resistance for the active resistor R_2 varied linearly from -0.1 % to 0.5 % with P . Similar analysis was carried out for resistors obtained at 400 $^\circ\text{C}$ for 90 minutes. In this case, R_0 value for the resistor R_2 measured from the set-up before the application of the force was $R_{02(400\text{ }^\circ\text{C})}$ (= 20.782 k Ω). The resistance for the active resistor R_2 varied linearly from 0.07 % to 0.3 % with applied pressure. Since the polysilicon grain size was somewhat larger on the average for

a higher temperature anneal described in Table 2.4, it was reasonable for the 500 °C annealed polysilicon thin film to exhibit a higher piezoresistance compared to the one annealed at 400 °C.

4.2.6 Advantages of Using AFM and Challenges

Above experiments proved the piezoresistive characteristics of polysilicon film obtained by AIC. These experiments used individual resistors R_2 and R_3 which were electrically isolated from each other to obtain an accurate estimation of their GFs and electrical behavior with varied applied pressure, P . Additionally, the use of AFM effectively enabled the application of differential pressures smaller than atmospheric pressures.

Advantages of using the current set-up were applications of very small (μN to mN) and variable forces on a wide variety of test structures. Additionally, a large piezo-scanner can be used for experiments requiring larger displacements (z -travel) and hence enabling larger force applications. Alternatively, probe-tips with different k values and/or attached particles with variable sizes and material can be used to achieve different sensitivities, hence enabling application of variable pressures with the same set-up. This set-up has an added advantage of its usefulness in experiments requiring pressure/force application on structures with smaller active area ranging from few tens to few hundreds of micrometers and smaller displacements (nm range), thus enabling very low forces/pressure applications.

However, these low forces are more sensitive to device geometry and fabrication anomalies occurring during photolithography, deposition and etch steps resulting in reduction or broadening of actual structure dimensions, variation of film thicknesses resulting in varied response from the devices. Also variations in surface morphology of thin films obtained by different deposition process (LPCVD, PECVD, sputtering, evaporation etc.) greatly alters the probe-tip to diaphragm surface interactions. In addition, the exact shape and material of the attached particle affect the contact mechanics between the structure and the particle surfaces, thus changing the probe-tip sensitivity thereby changing the pressure applied. However, by using a large particle in our case, we attempted to eliminate some of the surface interactions

occurring at the microscopic level and thereby achieving our goal of uniform diaphragm displacement with applied pressure.

4.3 Pressure Sensor Characterization

An array of pressure sensor structures were fabricated as illustrated in Figure 4.15 (a). Their fabrication was based on the process flow described earlier in Chapter 3. These sensor structures employed polysilicon film resistors obtained by AIC at 400 °C for anneal times of 90 minutes. These sensors were electrically connected as shown in Figure 4.15 (b).

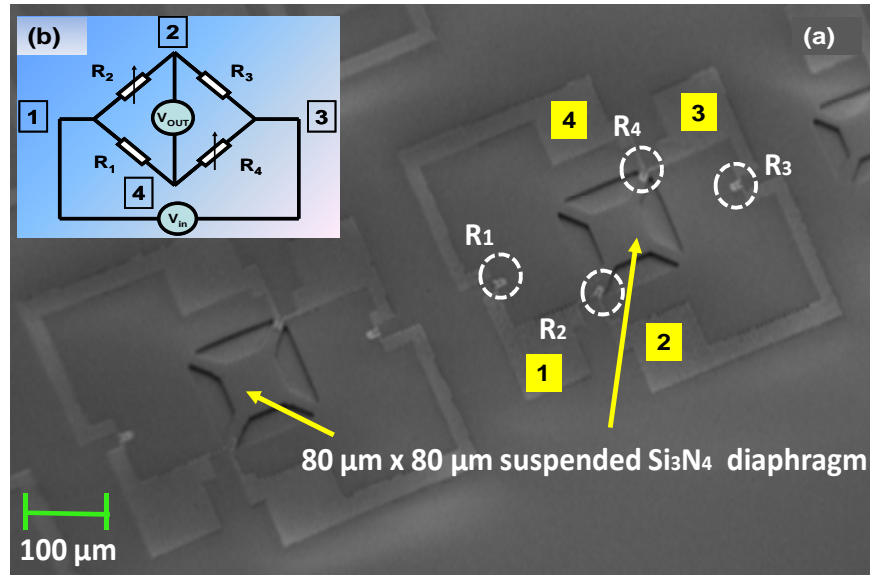


Figure 4.15 (a) An array of pressure sensors with AIC polysilicon resistors on suspended 80 x 80 μm^2 Si_3N_4 diaphragms, (b) a half-Wheatstone bridge electrical circuit for measuring ΔV_{OUT} versus P.

In order to find the S of the pressure sensor, two different methods of characterizations were used. The first method comprised of an AFM with modified probe-tip as described in earlier sections. This method enabled us to apply differential pressures smaller than atmospheric pressure (~ 101 kPa) and measure the ΔV_{OUT} of the sensor. This measurement provided us the low-pressure sensitivity (S_L) of our fabricated sensor. Second method of characterization of the sensor involved using a custom designed load-cell set-up. This measurement facilitated application of much higher differential pressures to the diaphragm and

provided the high- pressure sensitivity (S_H) of our fabricated sensors. Pressure sensor structures with diaphragm size of $80 \times 80 \mu\text{m}^2$ were deliberately chosen to facilitate the use of both AFM and load-cell for characterization purposes, since we were limited by r_p of the probe-tip for load-cell application.

Before we began characterizing our pressure sensors, we performed several VI measurements using Agilent 4155C to determine the values of individual resistors in order to estimate the sensor voltage at no applied pressure also known as sensor offset voltage, V_{OUT0} from Eq. (1.15).

4.3.1 VI Characteristics

The individual sensor devices were wire-bonded as shown in Figure 4.16, and their VI characteristics were measured. Figure 4.17 gives the VI characteristics of the resistors for the same device shown in Figure 4.15 (a). The current was swept from $-0.5 \mu\text{A}$ to $0.5 \mu\text{A}$. The plot shows a linear VI characteristic for the AIC polysilicon resistors with resistance values of $14.0 \text{ k}\Omega$, $19.0 \text{ k}\Omega$, $14.1 \text{ k}\Omega$ and $25.4 \text{ k}\Omega$ for R_1 , R_2 , R_3 and R_4 , respectively. The variation in resistances might be due to lithographic anomalies occurring during the alignment process and/or lift-off of the Al contact layer. Using the calculated resistance values (refer to APPENDIX D), V_{OUT0} (theoretical) was found to be 0.219 V when $V_{in}=1 \text{ V}$ at $P=0 \text{ kPa}$ from Eq. 1.15.

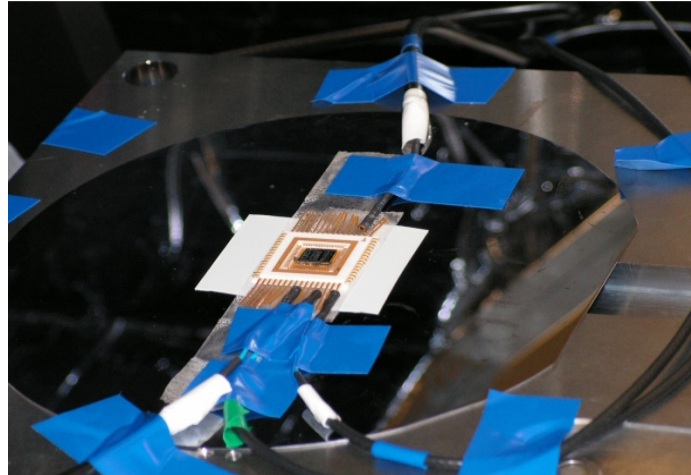


Figure 4.16 Individually wire-bonded pressure sensor device on a package ready to be characterized using AFM and load-cell set-up.

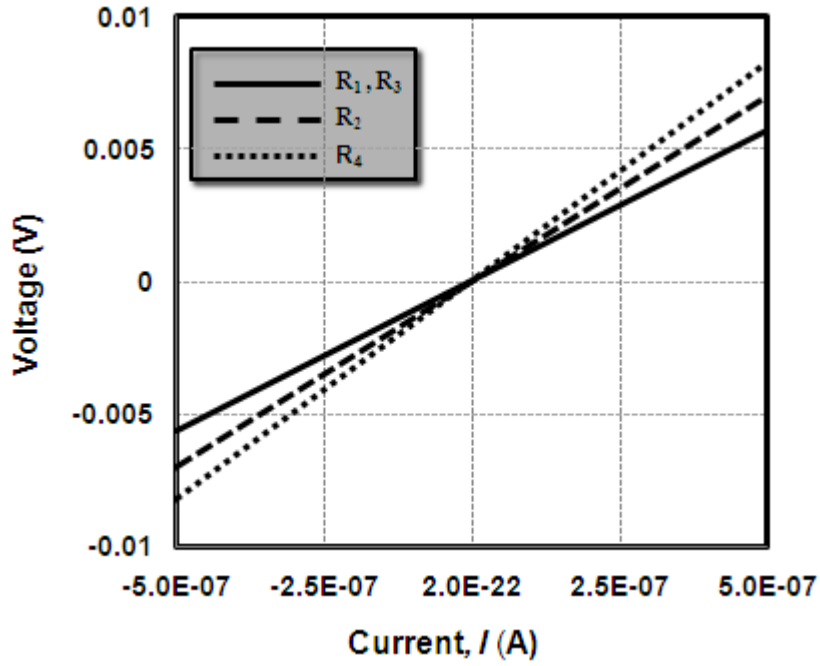


Figure 4.17 VI characteristics for R_1 , R_2 , R_3 and R_4 for the device in Figure 4.15.

4.3.2 Characterization using AFM

Before proceeding to characterize the sensor, the effective spring constant of the modified probe-tip was calculated as described in Section 4.2.1. Using the AFM in tapping mode, the f_{r1} was measured to be 57 kHz with the attached spherical borosilicate glass (density, $\rho_{\text{SiO}_2} = 2230 \text{ kg/m}^3$) particle with mass M . Therefore, the spring constant of the modified tip, k^l was calculated as 3.05 N/m from Eq. (4.2) for $f_{r0} = 315 \text{ kHz}$. Accounting for a correction factor due to the tilt introduced in the tip by the tip holder, the corrected effective spring constant for the modified tip, k_{eff} of 3.2 N/m was calculated from Eq. (4.3).

The sample was then placed under the AFM scan head as illustrated in Figure 4.6 (a). Figure 4.18 gives the schematic of the measurement set-up. It consisted of an Agilent dc voltage source to provide the V_{in} across contact pads 1 and 3 in the half-Wheatstone bridge circuit as described in Figure 4.15 (a).

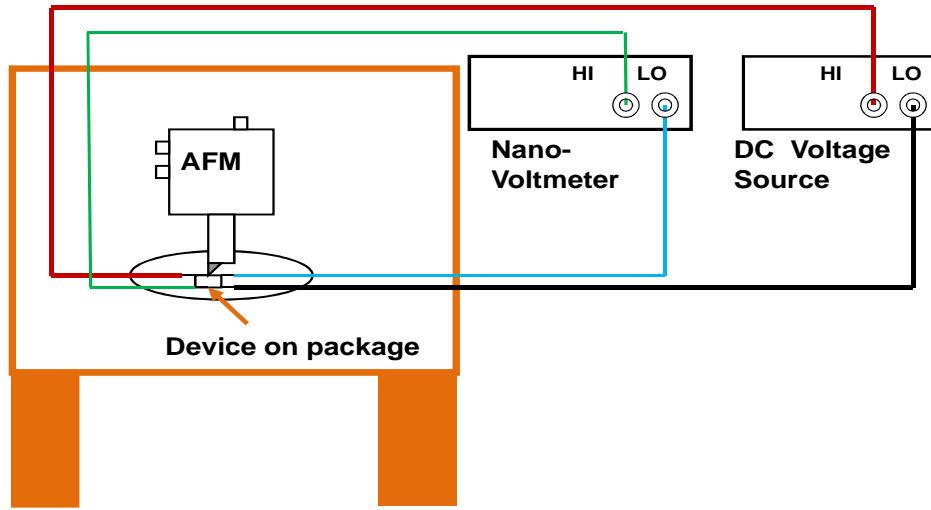


Figure 4.18 Schematic of pressure sensor characterization set-up using AFM.

The V_{OUT} of the sensor was measured across contact pads 2 and 4 using Keithley 2182A Nano-voltmeter. The suspended diaphragm was positioned below the probe-tip and the input bias voltage, V_{in} was set to 1V. Initially the offset voltage was measured with no applied pressure. The probe-tip was then engaged onto the diaphragm surface for V_t ranging from 1 V to 10 V in steps of 1 V. Corresponding S values were obtained from force plots for each increment of V_t , thereby calculating F and P for each case. Simultaneously, the $V_{OUT0} + \Delta V_{OUT}$ values given by Eq. (1.16) were also noted down for each V_t .

Since we only had a part of the spherical particle touching the diaphragm surface we approximated the A_c of the particle with the flat surface as a spheroid making a solid angle of θ . The maximum measured displacement, d of the diaphragm due to applied force, F was $\approx 0.3 \mu\text{m}$. Then θ of 9° was calculated from Eq. (4.5). This gave us A_c from Eq. (4.6). The pressure sensor response was successfully measured using this method for the force ranges of $0.1 \mu\text{N}$ to $1 \mu\text{N}$ corresponding to a low pressure ranging from 2 kPa to 19 kPa.

Figure 4.19 illustrates the pressure sensor response, ΔV_{OUT} with P. In this case, the measured output voltage ΔV_{OUT0} at zero applied pressure was 0.219 V for $V_{in}=1$ V. This enabled us to measure ΔV_{OUT} from $90 \mu\text{V}$ to $775 \mu\text{V}$ for pressures ranging from 2.14 kPa to 18.8 kPa. Pressure sensor sensitivity of 41.12 mV/MPa was calculated for 1 V input voltage.

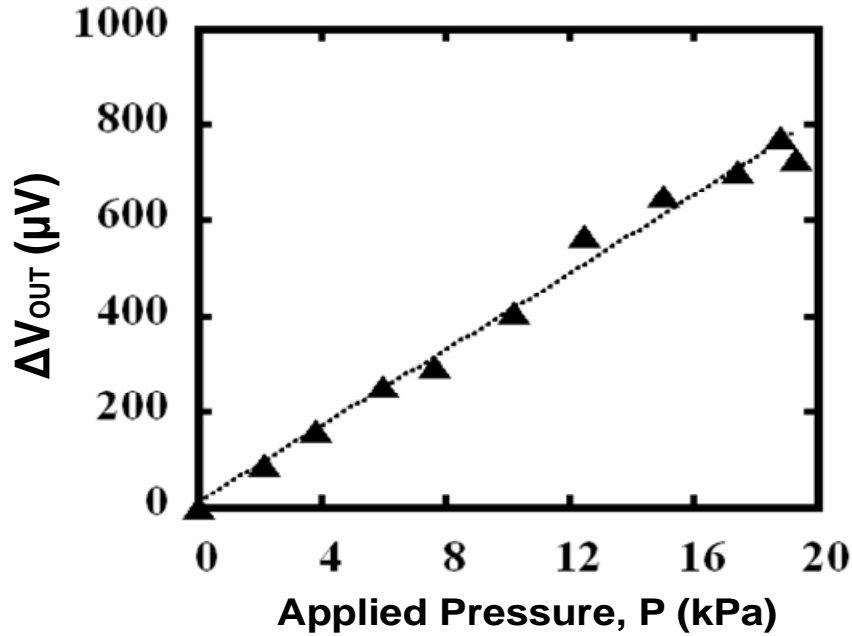


Figure 4.19 Pressure sensor response ΔV_{OUT} versus P using AFM.

4.3.3 Characterization using Load-Cell

A custom-built load-cell setup is illustrated in Figure 4.2. The probe-tip is placed approximately at the center of the diaphragm of the pressure sensor, using the XYZ moving stage and the nano-positioner. APPENDIX E gives the operating procedure for using the load-cell set-up for characterization. The set-up was designed for characterization of individual sensor both for applied normal pressure and had capability to tilt for application of shear pressures on the sensor. The stage on which the sensor was fixed could be tilted from 0° - 45° . However, present work involves with application of normal loads on the sensor.

The response of the individual sensor to a normal load was determined by lowering the probe onto the diaphragm using the nano-positioner controlled by a computer. The nano-positioner reading (in μm) directly gave the displacement of the diaphragm when a load, F was applied. As the diaphragm displaced, it induced strain in the active piezoresistors R_2 and R_4 . This brought about a change in their resistances (ΔR_2 and ΔR_4), which in turn changed the differential output voltage by ΔV_{OUT} , which was measured using the Keithley 2182A nano-

voltmeter. The applied load is measured in grams as a unit from the load cell. The applied load is controlled by the displacement of the diaphragm which in turn, is controlled by the nano-positioner. Therefore, the maximum z-travel of the probe-tip was limited by the PI-2611 sacrificial layer thickness underneath the Si_3N_4 diaphragm layer which was $1.5 \mu\text{m}$ in our case. A probe-tip of r_p of $10 \mu\text{m}$ was used for characterization purposes. The radius, r of the spherical particle in the AFM case was 2.5 times larger than r_p of the probe tip. For the present case of the load-cell, we calculated the pressure exerted by the tip, P on the diaphragm as

$$P = \frac{F}{\pi r_p^2} \quad (4.11)$$

First, the sensor ΔV_{OUT} was measured by increasing applied normal loads from zero to the maximum safe load, F_{max} in incremental displacements. This was for the loading or forward Z-travel case. Next, the applied load was decreased from F_{max} to zero load in the same step size and sensor ΔV_{OUT} was measured. This constituted the unloading or backward z-travel case. The measure of ΔV_{OUT} deviation due to hysteresis was obtained.

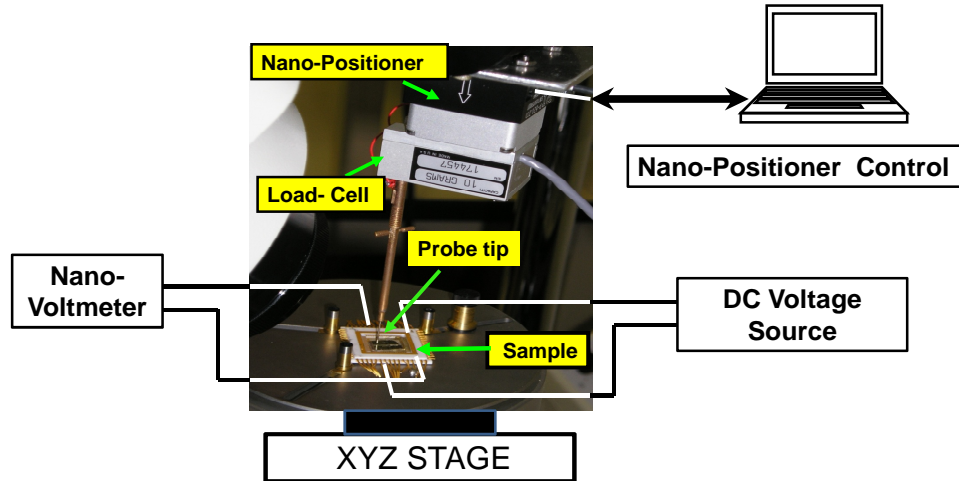


Figure 4.20 Schematic of pressure sensor characterization set-up using load-cell.

The sensor was electrically connected as described in Figure 4.20 and V_{in} of 1V was applied. Again, $\Delta V_{\text{OUT}0}$ of the pressure sensor was measured with no applied pressure. For V_{in} of 1 V, the measured $V_{\text{OUT}0}$ was 0.218 V. The probe-tip was then engaged onto the diaphragm surface by instructing the nano-positioner to move down in steps of $0.2 \mu\text{m}$. The load and

corresponding output voltage ($V_{OUT0} + \Delta V_{OUT}$) value noted for each travel step. Then, the probe-tip was moved up gradually and again the corresponding output voltages were noted down. Sensor response was successfully measured with this technique for force values ranging from 68 μN to 620 μN with corresponding pressures ranging from 0.2 MPa to 2 MPa as depicted in Figure 4.21.

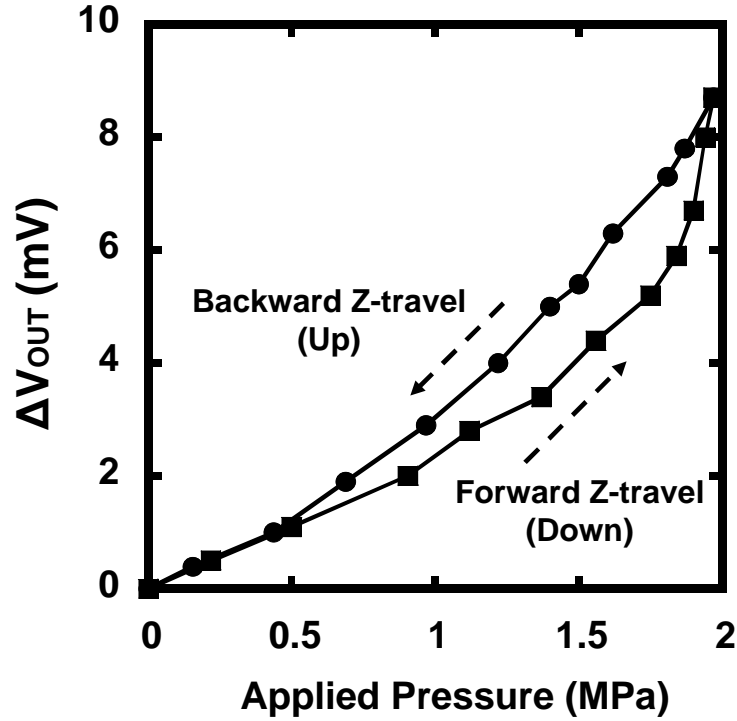


Figure 4.21 Pressure sensor response ΔV_{OUT} versus P using load-cell.

From Figure 4.21, we see that the pressure sensitivity in this case was 5.02 mV/MPa for $V_{in}=1$ V. At higher pressures, it was observed that the change in the output voltage was relatively higher for a corresponding increase in P. At full diaphragm deflection maximum strain was induced on the bridge arms resulting in a higher change in the output voltage.

4.3.3 Non-Linearity

By comparing Figures 4.19 and 4.21, we see that the change in ΔV_{OUT} is much more linear at lower applied pressure than at larger applied pressure. L. Lin et al. [138] showed that the sensor output was linear for small deflections corresponding to lower applied pressure.

However, small percentage of non-linearity in sensor output was observed at higher pressure ranges due to variations in the resistances making up the Wheatstone bridge, thus causing nonlinear response as well as offset voltage at zero pressure because of slightly different ΔR values each piezoresistor exhibits. This is due to process variations leading to mismatch in piezoresistor dimensions, contact resistance and metal interconnects.

4.3.4 Hysteresis

For larger applied pressures, we see a hysteresis as depicted in Figure 4.21. This could be explained by the non-linear deflection behavior of diaphragm when it goes from lower pressure regime to higher pressure regime [25, 138, 139]. In low-pressure regime, the behavior of the suspended diaphragm can be well approximated by thin-plate / small deflection theory. Small deflection theory could be considered when the diaphragm deflection was lesser or equal to 0.2 times the diaphragm thickness [25]. In our case smaller pressures were applied using the AFM which resulted in smaller diaphragm deflections. Higher pressures were successfully applied using the load-cell set-up. In this case, when high pressures acted upon the suspended diaphragm its behavior was in accordance with thick-plate/ large deflection theory [139]. As the measured diaphragm deflections were less than or equal to 3 times the diaphragm thickness, large deflection theory was considered [25].

At low pressures, the maximum deflection of the diaphragm, d was $\approx 0.3 \mu\text{m}$ corresponding to the applied pressure of 19 kPa when compared to deflection of $\approx 1.5 \mu\text{m}$ corresponding to the applied pressure of 2 MPa. At higher applied pressures the diaphragm had deflections comparable to the thickness of the Si_3N_4 diaphragm ($1.5 \mu\text{m}$). This could be the reason for observed hysteresis. This hysteresis could be effectively reduced by slightly increasing the thickness of the diaphragm with a corresponding compromise in sensitivity.

4.4 Summary

Present chapter explained the characterization of nano-crystalline polysilicon films to obtain their piezoresistive properties. This was done by measuring the relative change in resistances $\Delta R/R_0$ with applied pressure and by estimating their gauge factors. For this

purpose, an array of pressure sensors was successfully fabricated on a flexible polyimide substrate using AIC polysilicon piezoresistors as Wheatstone bridge elements.

The use of AFM as a MEMS piezoresistive pressure sensor characterization tool has been described. A sensitive electrical characterization set-up has been demonstrated for an effective measurement of small changes in voltage and current flowing through the piezoresistors during AFM tip engagement and scan steps. The AFM was used in contact mode by means of force-plots to calculate the amount of force exerted by the probe-tip on the surface-micromachined diaphragm surface. Two piezoresistors lying on the diaphragm bridge arms were considered for characterization purposes. These devices differed only in the size of their suspended diaphragm structures. Using a modified probe-tip with an attached 25 μm radius spherical particle, low pressure ranges down to few tens of kPa's were obtained. Another merit of using modified probe-tip was to effectively displace the diaphragm with applied pressure. As the pressure was distributed uniformly over a larger area when compared to conventional AFM probe-tips. A linear change was observed in the piezoresistance up to 70 kPa. The set-up facilitated the dynamic measurement of response from pressure sensors with varying applied force, down to 0.02 % piezoresistance change. Our experiments showed the device with a smaller diaphragm gave a slightly higher % $[\Delta R/R_0]/P$ compared to the device with a larger diaphragm for similar resistor geometry. Additionally, the current set-up demonstrated the flexibility in scaling up or down of the applied forces/pressures on the test structures. This could be effectively achieved by the selection of various cantilevers with varying material, spring constants and attached particle geometries.

Pressure sensor device with a diaphragm size of $80 \times 80 \mu\text{m}^2$ and employing polysilicon film obtained by AIC at 400 °C for an anneal time of 90 minutes was used for characterization. AFM was employed to characterize this sensor for lower pressure ranges of 2 kPa to 19 kPa. A load-cell coupled with a nano-positioner was utilized to characterize the same sensor for the higher pressure ranges between 0.2 MPa to 2 MPa. A maximum output voltage change of 8.7 mV was observed at an applied pressure of 2 MPa for a Wheatstone bridge input voltage of 1 V.

CHAPTER 5

SUMMARY

Pressure sensors on flexible polyimide substrates employing polysilicon as piezoresistive sensing elements were fabricated and tested. A successful surface-micromachined MEMS fabrication process was developed with polyimide as the substrate. This would facilitate integration of numerous sensors and actuators on a single flexible substrate which has important advantages of being light-weight, low profile and less expensive than conventional rigid substrates. They could be conformally deposited or packaged around the test structures of various shapes and sizes. Additionally, the developed process was CMOS compatible so that it would allow ready integration of various digital/ analog electronic circuitry onto a single die.

Polyimide PI-2611 was used to form the substrate as well as the sacrificial layer under the Si_3N_4 diaphragm. This allowed a very clean and dry removal of sacrificial PI-2611 layer by ashing in O_2 plasma. This processing step completely avoided the stiction problem often encountered while suspending the MEMS structures during the final etch step. A successful curing profile for the polyimide was developed. It ensured the integrity of the substrate and sacrificial polyimide layers during the various anneal temperature steps slightly above the T_g of the polyimide.

Pressure sensor fabrication was based on the designs given by Shamanna et al. [16]. Most essential and critical step of the fabrication was the low-temperature deposition of the polysilicon film. Conventional techniques for depositing polysilicon film included low –pressure chemical vapor deposition, atmospheric- pressure chemical vapor deposition, plasma-enhanced chemical vapor deposition, hot-wire chemical vapor deposition, and sputter. However, the above methods often require high temperature deposition and complex equipment modification. Additionally, polysilicon films obtained using some of these techniques often required a post-

deposition doping step, followed by an annealing step for electrical activation. Since we were limited by the T_g (400 °C) of the polyimide, the above methods greatly deterred us from using them for our polysilicon film depositions. Crystallization of amorphous silicon by solid phase crystallization and laser annealing was also considered. However, their disadvantages of being expensive, relatively slow and possible contamination issues out-weighed their advantages for using them as post-deposition film crystallization techniques as described in detail in Chapter 2. Therefore, we were forced to look for options. Aluminum induced crystallization came out as a clear winner due to its relatively simpler approach and advantage of the polysilicon film being simultaneously doped with Al during the annealing step. Since polysilicon film grain size was an important parameter to define its piezoresistive nature. Aluminum induced crystallization gave us greater control over the film morphology such as crystallinity and grain size.

As explained in Chapter 2, annealing of adjacent aluminum and amorphous silicon layers in contact with each other resulted in silicon atoms breaking free from the silicon lattice also termed as free silicon atoms. These free Si-atoms have enough energy to diffuse into aluminum layer and start nucleating at the aluminum layer grain boundaries. As time advances more and more silicon atoms join forming grains of silicon and eventually displacing aluminum from its lattice, thus causing crystallization of amorphous silicon. During this process, some amount of aluminum is incorporated in the crystallized silicon layer making it p-type doped. Researchers believe that aluminum here acts as a substitutional impurity in silicon. The displaced aluminum reaches the surface of crystallized silicon. This excess aluminum is subsequently etched away in standard aluminum etch solution thereby obtaining a low-temperature p-type doped uniform polysilicon film.

Present work demonstrates various annealing profiles for aluminum induced crystallization of amorphous silicon. The resultant polysilicon films were studied for their texture, grain size and electrical characteristics. The polysilicon film grain sizes varied with different anneal profiles such as temperature, time and ambient gases. We obtained polysilicon films with good crystallinity even at temperatures as low as 400 °C for 60 minutes, and for shorter

anneal times of 30 minutes at 500 °C. The resultant polysilicon films gave average grain sizes of around 60-70 nm as estimated from the XRD measurements. However, SEM images showed relatively larger grain sizes of 150-200 nm. Sheet resistance measurements of the polysilicon films placed its sheet resistance between 1.5 -2 k Ω / \square .

Once we validated the feasibility of AIC of a-Si to obtain polysilicon films, we started with fabrication of our pressure sensor structures. Chapter 3 gives a detailed step- by-step process flow for the fabrication of pressure sensors on flexible polyimide substrate. The final fabricated array of pressure sensors in the die were diced and bonded onto commercially available electronic chip packages. Individual pressure sensor structures and resistors were wire-bonded for further electrical and pressure sensitivity characterization.

IV characteristics of individual polysilicon film resistors obtained by aluminum induced crystallization of amorphous silicon were carried out using Agilent 4155C as described in Chapter 4. Resistance values in the range of 12-30 K Ω were typically measured. In order to validate the piezoresistive property of the polysilicon film obtained by amorphous silicon, atomic force microscope with modified probe-tip was used. The use of atomic force microscope facilitated low-pressure application onto our pressure sensor diaphragm. Additionally, we could measure the precise deflection of the diaphragm with applied force. Low pressures in the range of 5 – 70 kPa were successfully applied.

In order to measure the relative change in resistance of the piezoresistors ($\Delta R/R_0$) due to applied pressure, the individual resistors in the sensor structure were isolated from each other by removal of aluminum interconnects between them. This was achieved by scratching off the aluminum metal lines using a micromanipulator probe. The $\Delta R/R_0$ was effectively measured using a 4-wire resistance measurement set-up, employing a Keithley 2182A Nanovoltmeter. This application of force/pressure on the diaphragm resulted in induction of strain on the bridge arms of the diaphragm, which eventually resulted in a change in resistance of the polysilicon piezoresistors due to their internal energy band bending and physical deformation. From this set-up, we measured very small $\Delta R/R_0$ changes from 0.02 % upto 1.4 %. This proved the

piezoresistive property of our polysilicon film obtained by aluminum induced crystallization of amorphous silicon. Chapter 4 gives the experimental procedure of pressure sensor characterization using atomic force microscope and the corresponding results.

The next stage of research comprised of estimating the gauge factor of our piezoresistive polysilicon films. The measured $(\Delta R/R_0)$ obtained from atomic force microscope measurements were used in conjugation with finite element analysis based mechanical simulations using CoventorWare. The 3-D simulation model consisted of suspended silicon nitride diaphragm of sizes $80 \times 80 \mu\text{m}^2$ and $70 \times 70 \mu\text{m}^2$ with polysilicon resistors (active resistors) embedded on their bridge arms. Pressure values obtained previously from the atomic force microscopy experiments were applied onto these diaphragms. The simulation results of the diaphragm deflection were cross-checked and matched with measured deflection of the diaphragm measured by the atomic force microscope, to estimate the gauge factor accurately. From numerical calculations as described in Chapter 4 we obtained typical gauge factor values between 7 to 12. However, this value was only a rough estimation as gauge factor greatly depended on the changes in measured resistance due to actual variations of any device geometries such as that of the bridge arms, resistor dimensions, and thicknesses associated with them. Additionally, strain distribution on the diaphragm due to pressure application would vary with the probe-tip placement. Nevertheless, the polysilicon films obtained by aluminum induced crystallization of amorphous silicon showed considerably good piezoresistive property.

Subsequently, to measure the sensitivity of our fabricated pressure sensors they were individually diced and wire-bonded onto a chip package. Input bias voltage, V_{in} of 1 V was applied and the half-Wheatstone bridge's output voltage, V_{OUT0} was measured. When pressure was applied on the diaphragm, this brought about a certain change in its output voltage $V_{OUT0} + \Delta V_{OUT}$, which was measured by the nanovoltmeter. The relative change in output voltage, ΔV_{OUT} versus pressure was plotted and the pressure sensor sensitivity was determined. We obtained excellent low-pressure sensitivity value of 41 mV/V/MPa. In order to characterize the sensor at higher pressures, a load-cell setup was used as described in Chapter 4. Here, the load-cell

coupled to the nanopositioner was utilized to exert pressure onto the diaphragm. By controlling the displacement of the probe, the amount of pressure was varied. The pressure sensor diaphragm was able to withstand high pressures upto 2 MPa. This displayed the versatility of our fabricated pressure sensor and enabled us to characterize the pressure sensor at high pressures. As expected, at the higher applied pressure regime, the sensitivity of the pressure sensor dropped to 5 mV/V/MPa. There was some non-linearity and hysteresis observed which could be effectively explained by the deflection-plate theory given in [138]. Thus, our fabricated sensor behaved well within the realms of the mechanical behavior theory for suspended diaphragms. Additionally, we compared the performance of our present work with some of the other recent works on pressure sensor designs. From the Table 5.1, we can clearly point out the obvious improvement in sensitivity of our pressure sensor with respect to its size of the sensing area. Even though our sensor design and working was based on a half-Wheatstone bridge principle, we can clearly see the superiority of our fabricated sensor to full-Wheatstone bridge designs.

Table 5.1 Comparisons of some recent pressure sensor designs with present work

Authors [Ref. #]	Substrate (Micromachining)	Polysilicon Deposition Method	Thickness of Polysilicon Film (nm)	Sensing Area (mm x mm)	Max. P (MPa)	S (Kind of Wheatstone bridge)
L. Lin et al. [139]	Si (Surface)	LPCVD with P doping	100	0.1 x 0.1	0.69	21.74 mV/V/MPa (Half)
C. Malhaire et. al. [58]	Si (Bulk)	LPCVD at 620 °C followed by B doping, followed by crystallization step at 1100°C	460	3 x 3	0.02	500 mV/mA/MPa (Full)
H. C. Lim et al. [140]	Kapton (Surface)	a-Si:H PECVD followed by annealing at 350 °C for 30 min	200 nm α- Si:H + 65 nm n+ α- Si:H	10 x 10	0.014	23.54 mV/(MPa) ^{1/2} (Full)
Y. Zhang et al. [141]	Si (Bulk)	LPCVD with B doping followed by annealing step at 1050°C	-	0.37 x 0.37	1	15.5 mV/V/MPa (Full)
S. Chen et al. [142]	Si (Bulk)	LPCVD with B doping	240	1.15 x 1.15	0.15	230 mV/V/MPa (Full)
K. Saejok et al. [143]	Si (Surface)	LPCVD followed by B doping and annealing at 800 °C for 15 hours	400	0.1 x 0.1	0.7	68.7 mΩ/Ω/MPa

Table 5.1 - continued

X. Liu et al. [144]	Si (Bulk)	LPCVD at 625 °C followed by B doping at 1100°C	80	2:1 (Ratio)	0.6	15.5 mV/V/MPa (Full)
<i>Present Work</i>	Polyimide (Surface)	AIC at 400 °C , 90 minutes	500	0.08 x 0.08	0.02 (AFM)	41.12 mV/V/MPa (Half)
					2 (Load- Cell)	5.02 mV/V/MPa (Half)

CHAPTER 6

CONCLUSIONS

The work presented here is a low temperature method for obtaining polysilicon piezoresistive thin films using aluminum-induced crystallization (AIC) of amorphous silicon (a-Si) film. We have obtained nanocrystalline polysilicon films with average grain sizes of 45-55 nm at temperatures ranging from 400 °C to 500 °C with an annealing time of 60 minutes, and an average grain size of 50 nm at 500 °C for a shorter annealing time of 30 minutes. An additional advantage of this process is that the polysilicon films are simultaneously doped p-type, thereby eliminating any additional doping step. By varying the aluminum (Al) and a-Si layer thicknesses, annealing temperature and duration, the growth of polysilicon grains ranging from few tens of nanometers to tens of microns in diameter can be effectively obtained. Exploring the piezoresistive properties of the above mentioned low temperature nanocrystalline polysilicon thin films deposited on plastic substrates for pressure sensing applications was an additional focus of this research. To test the piezoresistive properties of the AIC obtained polysilicon films, prototype MEMS based pressure sensors were fabricated on flexible polyimide substrate. The sensors comprised of a surface-micromachined silicon nitride diaphragms with polysilicon resistors as pressure sensing elements connected in a half-Wheatstone bridge configuration. The polysilicon resistors showed linear IV characteristics with typical resistance values between 15 – 30 kΩ. Atomic Force Microscope was used in contact mode to study the response of the pressure sensor with applied pressure in the 2 kPa to 19 kPa range. For the higher range of 450 kPa to 2 MPa, a load-cell with a nanopositioner was utilized. The pressure sensor sensitivity was measured to be 41.12 mV/MPa and 5.02 mV/MPa, respectively, for these ranges, when the Wheatstone bridge was biased at 1 V.

APPENDIX A

GRAIN SIZE ESTIMATION FROM XRD MEASUREMENTS

XRD data using (θ - 2θ) configuration was obtained for polysilicon films obtained by aluminum induced crystallization of amorphous silicon at various anneal temperatures and times. For simplicity only $\langle 111 \rangle$ peak was considered for grain size calculations. Figure A.1 gives the $\langle 111 \rangle$ plot for polysilicon film obtained at anneal temperature of 475 °C and anneal time of 60 minutes.

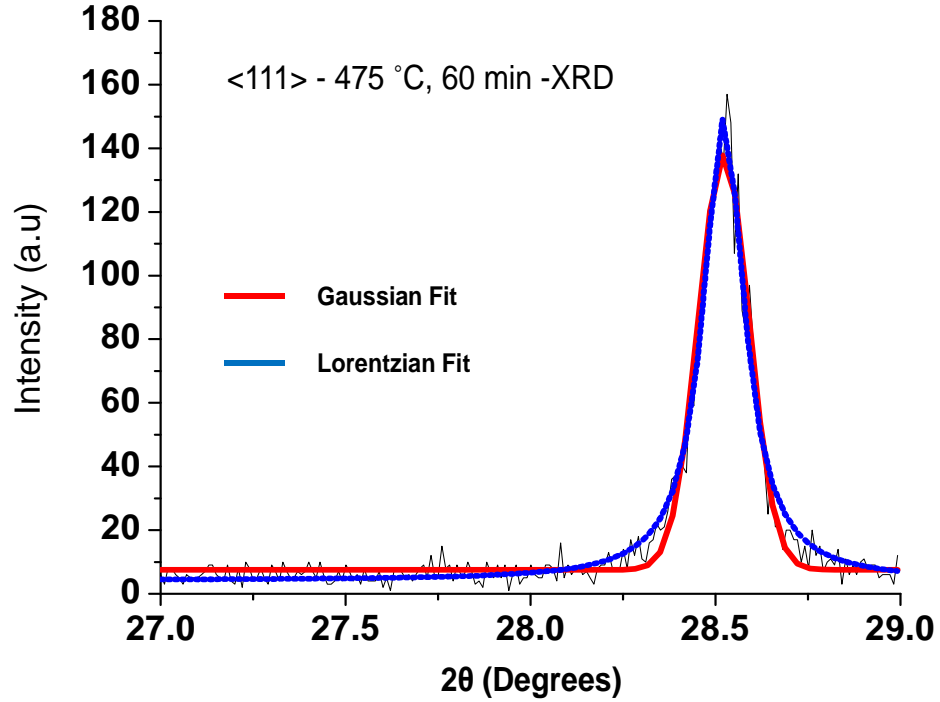


Figure A.1 $\langle 111 \rangle$ plot from θ - 2θ measurements for polysilicon film obtained by AIC of a-Si at 475 °C and 60 minutes.

The data points were fitted using Gaussian and Lorentzian fit using ORIGIN™ software.

For the above curve fit we obtained the following fit information:

1. Gaussian Fit

Equation:

$$y = y_0 + \left(\frac{A}{w \cdot \sqrt{\frac{\pi}{2}}}} \right) \cdot e^{-2 \left(\frac{x - x_c}{w} \right)^2} \quad (\text{A.1})$$

We obtain the following parameters from the fit:

$$\begin{aligned}
 R^2 & 0.97198 \\
 y_0 & 7.53661 \pm 0.40335 \\
 x_c & 28.52243 \pm 0.0011 - 2\theta \text{ angle of measured the } \langle 111 \rangle \text{ peak} \\
 w & 0.13679 \pm 0.00228 \\
 A & 22.35912 \pm 0.34416
 \end{aligned}$$

For Gaussian Fit, Full Width Half Maximum was approximated as:

$$B = \sqrt{2 \cdot \ln 2} \cdot w \quad (\text{A.2})$$

where w is the width of the curve fit, with K = 0.9 (Shape Factor)

$$\begin{aligned}
 \lambda_{\text{Cu-K}\alpha} & 1.54 \text{ \AA} \\
 \text{Grain size, } L_C & = 0.9 \cdot \lambda_{\text{Cu-K}\alpha} / (B \cdot \cos \theta) \text{ (m)} \quad (\text{A.3})
 \end{aligned}$$

Table A.1 Gaussian fit parameters obtained from ORIGIN™ software for <111> peak using θ -2 θ measurements for polysilicon film obtained by AIC of a-Si at 475 °C, 60 minutes

Center Frequency 2 θ (°)	θ (°)	cos θ	w (°)	w (radians)	FWHM = B (radians)	Grain Size (L_C) (m)
28.5224	14.2612	0.9692	0.1368	0.0024	0.002811	50.9 x10 ⁻⁹

2. Lorentzian Fit

$$\text{Equation: } y = y_0 + \frac{2A}{\pi} \cdot \left(\frac{w}{4 \cdot (x - x_c)^2 + w^2} \right) \quad (\text{A.4})$$

We obtain the following parameters from the fit:

$$\begin{aligned}
 R^2 & 0.97367 \\
 y_0 & 4.22575 \pm 0.43316
 \end{aligned}$$

x_c 28.5226 \pm 0.00101 - 2θ angle of measured the <111> peak

w 0.13508 \pm 0.00316

A 30.80748 \pm 0.56557

For Lorentzian Fit, Full Width Half Maximum was approximated as:

$$B = w \quad (A.5)$$

where w is the width of the curve fit, with $K = 0.9$ (Shape Factor)

$\lambda_{Cu-K\alpha}$ 1.54 Å

$$\text{Grain size, } L_C = 0.9 \cdot \lambda_{Cu-K\alpha} / (B \cdot \cos\theta) \text{ (m)} \quad (A.3)$$

Table A.2 Lorentzian fit parameters obtained from ORIGIN™ software for <111> peak using θ - 2θ measurements for polysilicon film obtained by AIC of a-Si at 475 °C, 60 minutes

Center Frequency 2θ (°)	θ (°)	$\cos\theta$	w (°)	w (radians)	FWHM = w B (radians)	Grain Size (L_C) (m)
28.5226	14.2613	0.9692	0.1351	0.00236	0.00236	60.7 $\times 10^{-9}$

APPENDIX B
PRESSURE SENSOR DESIGNS

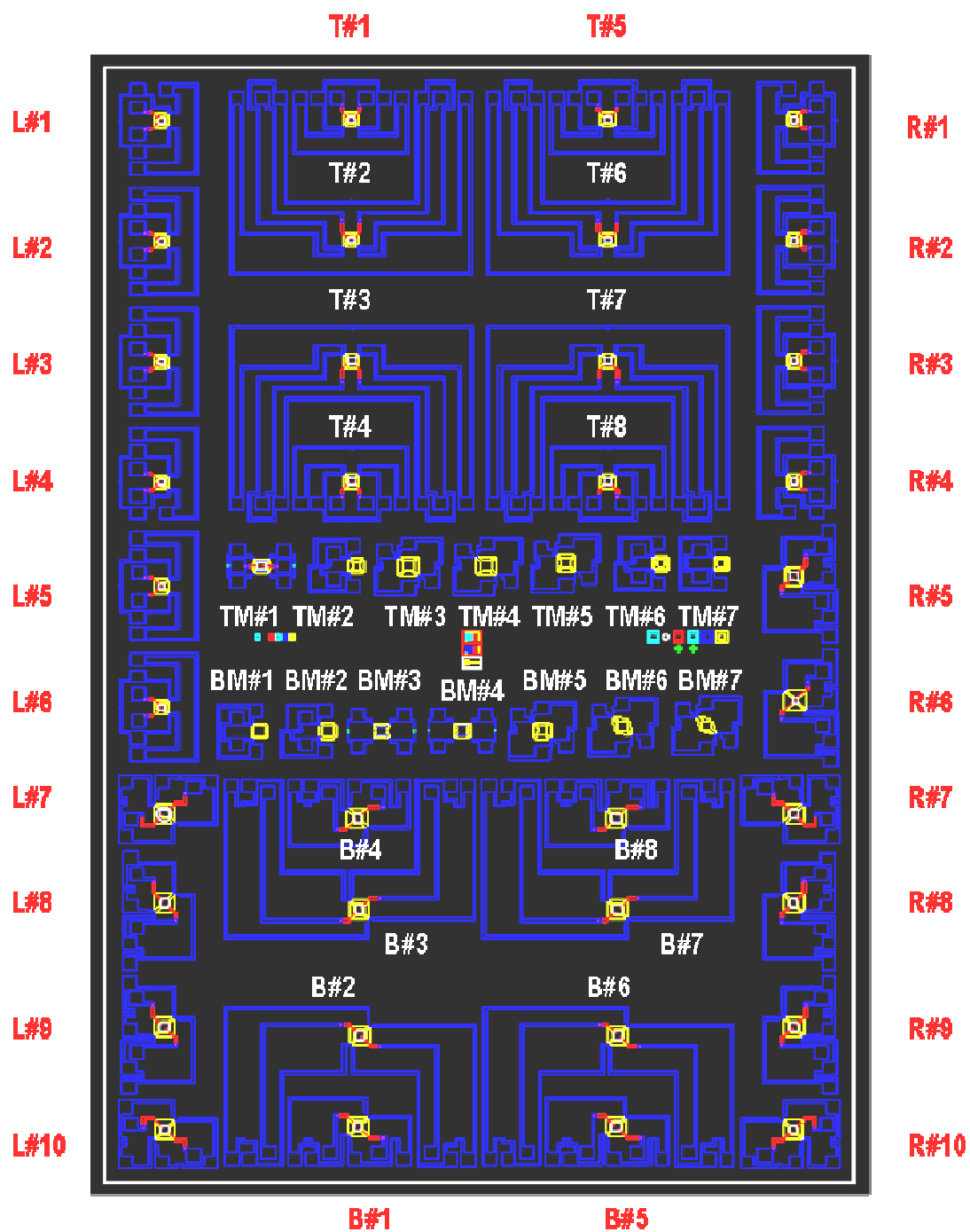


Figure B.1 Mask layout for various pressure sensors.

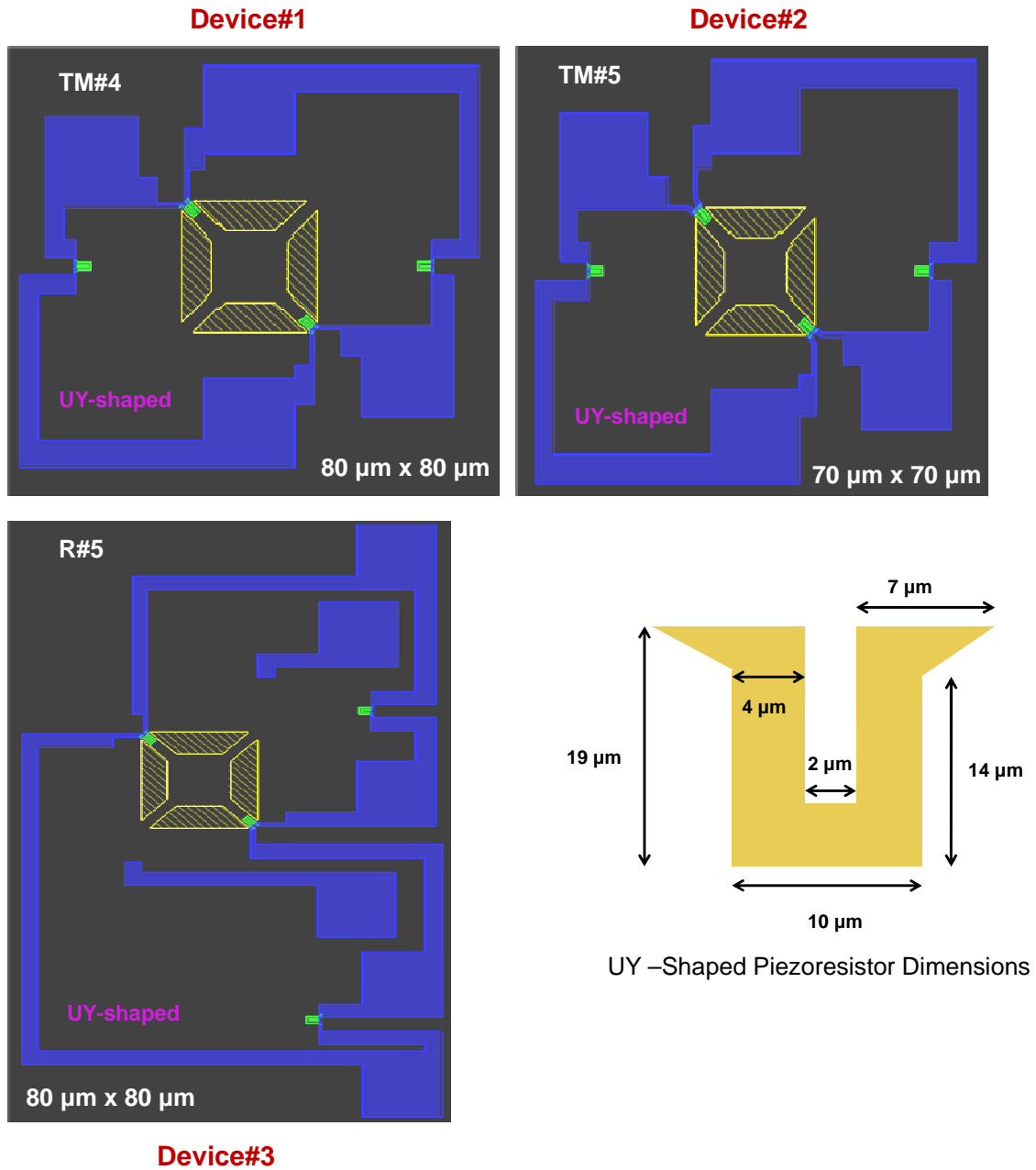


Figure B.2 Pressure sensors TM#4, TM#5 and R#5 corresponding to Device#1, Device#2 and Device#3 respectively (Not to scale).

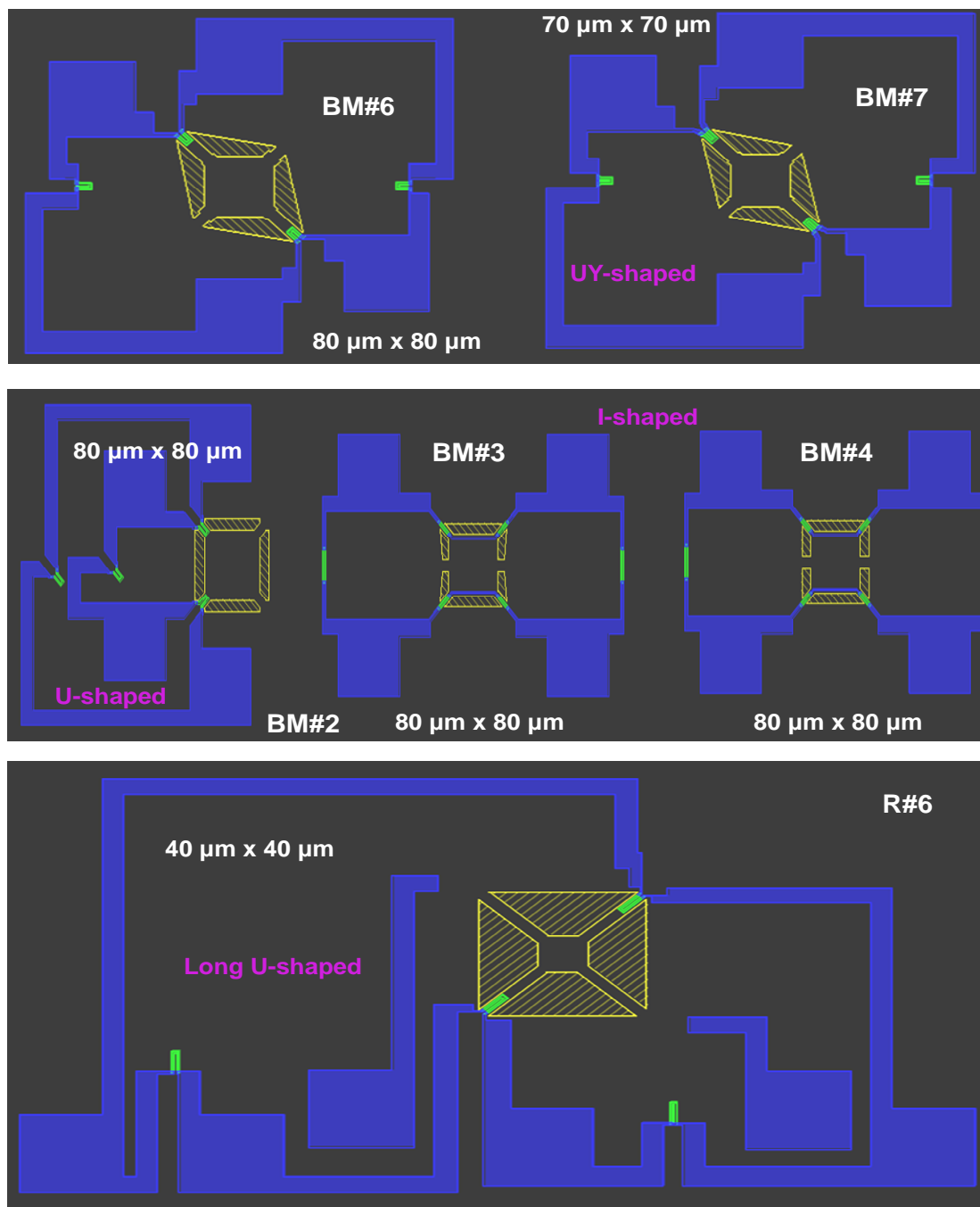
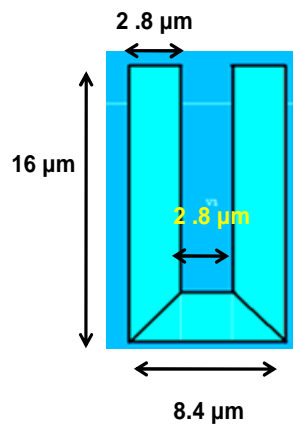
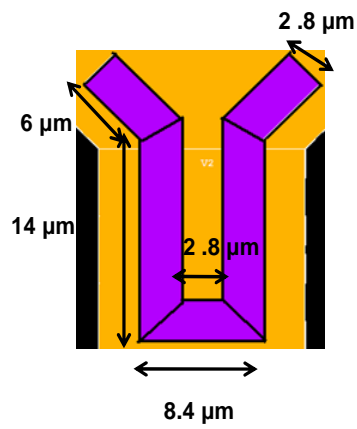


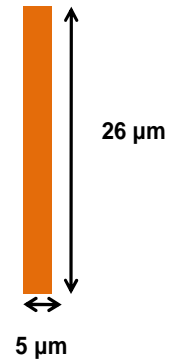
Figure B.3 Various pressure sensors structures with different diaphragm shapes, sizes and piezoresistors (Not to scale).



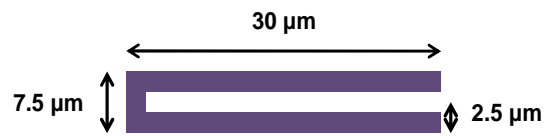
U-shaped



Y - shaped



I- shaped



Long U- shaped

Figure B.4 Piezoresistors with different shapes and sizes (Not to scale).

APPENDIX C

PROCEDURE FOR PRESSURE SENSOR CHARACTERIZATION USING
ATOMIC FORCE MICROSCOPE
(DEVELOPED BY: SURAJ KUMAR PATIL)

Below is the procedure for pressure sensor characterization using AFM in Advanced Contact Mode. After the probe-tip was placed in the tip-holder. First step involved with finding the resonant frequency (f_{r1}) of the probe-tip. This was done by the following:

1. Select the mode of operation as TAPPING Mode.
2. Align the laser: Sum signal should be 4-6 Volts.
3. Adjust the photo-detector voltages:

Horizontal deflection voltage (Horiz. Defl.) = 0.0 V

Vertical deflection voltage (Vert. Defl.) = 0.0 V

4. Cantilever Tuning: Using auto-tune option, find the resonant frequency. This step also serves as a check to determine whether the laser beam spot was incidenting on the edge of the cantilever probe-tip or not.

Next stage involves with placing the sample under the AFM scan head and performing preliminary IV measurements and electrical continuity check of the pressure sensor using a dc voltage/current source and nano-voltmeter. After these measurements the sample on the stage was brought closer to the AFM scan head and the following steps were followed:

5. Select the mode of operation as CONTACT Mode.
6. Adjust the photo-detector voltages:

Horizontal deflection voltage (Horiz. Defl.) = 0.0 V

Vertical deflection voltage (Vert. Defl.) = - 2.0 V

This value may vary depending on the probe-tip. A DNP/MLCT tip will do fine with this value, however for the FESP tip, for instance, you will use something lower, ~ -0.5 V. For the TESP tip, Vert Defl.: ~ -0.3 V.

7. Locate the tip and focus on the probe-tip.
8. Next focus on the sample surface.
9. Set Initial Scan Parameters as follows:

In Scan Controls panel:

Scan Size: 1 μm , X Offset: 0 μm , Y Offset: 0 μm , Scan Angle: 0

10. In Feedback Controls panel:

Setpoint: 0 Volts, Integral Gain: 3.0, Proportional Gain: 3.0, Scan Rate: 2 Hz.

11. Engage the SPM head onto the sample surface and we see that the scanning of the surface had started. Observe the Z-center and make sure that probe-tip is neither in extended nor in retracted region.
12. Go to View -> Force Mode -> Advanced

Under Main Controls panel (Ramp Controls)

Setting the Units: Metric

Ramp Channel: Z

Ramp Size: 1 - 1.5 microns

Scan rate: 0.996 Hz

13. In Channel 1 panel, select the following:

Data Type: Deflection

Data Scale: 20.00 V and set the Data Center = 0

14. In the Feed-back Controls Panel, set the following:

Integral Gain: 2.0

Proportional Gain: 3.0

Deflection Setpoint: 0 V

Deflection Limit: 2.5 V

15. In the Scan Mode Panel, set the following:

Trigger Mode: Relative

Trigger Channel: Deflection

Trigger Direction: Positive

Start Mode: Calibrate

End Mode: Retracted

Z step Size: 0V. Set the threshold trigger voltage between 0 V to 10 V.

16. Engage the probe-tip again onto the sample surface and simultaneously measure the corresponding change in output voltage of the sensor. The slope of the force plot gives the S_v .

The above process was repeated for the required number of input trigger voltages and corresponding S_v were noted down. This gave us the force exerted by the probe-tip on the suspended Si_3N_4 diaphragm.

APPENDIX D
RESISTANCE CALCULATIONS FROM WHEATSTONE BRIDGE

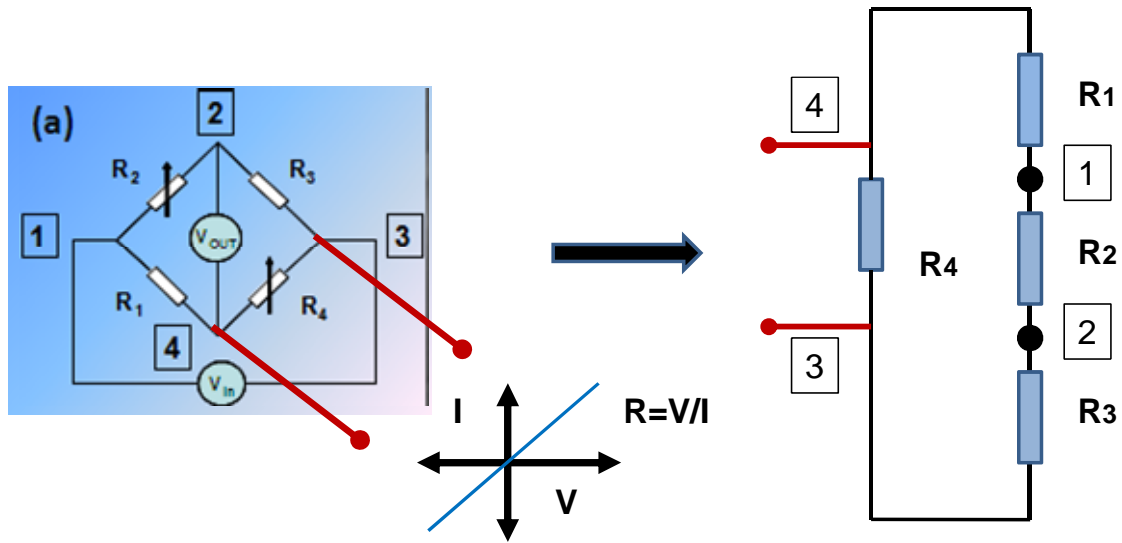


Figure D.1 Wheatstone bridge circuit and corresponding equivalent circuit for measurement of individual resistance R_4 .

If we measure IV across contact pads/ terminals 3 and 4, we get $R_{4(\text{Measured})}$ which is equivalent resistance, $R_{4(\text{Eq.})}$ given by:

$$\begin{aligned} R_{4(\text{Measured})} &= R_{4(\text{Eq.})} = R_4 \parallel (R_1 + R_2 + R_3) \\ R_{2(\text{Measured})} &= R_{2(\text{Eq.})} = R_2 \parallel (R_1 + R_3 + R_4) \\ R_{1(\text{Measured})} &= R_{1(\text{Eq.})} = R_1 \parallel (R_2 + R_3 + R_4) \\ R_{3(\text{Measured})} &= R_{3(\text{Eq.})} = R_3 \parallel (R_1 + R_2 + R_4) \end{aligned}$$

Similarly, we obtain $R_{2(\text{Measured})}$, $R_{3(\text{Measured})}$ and $R_{1(\text{Measured})}$. By using a simple MATHCAD program, we can solve for individual resistances as follows:

Here $R_{4(\text{Measured})}$, $R_{2(\text{Measured})}$, $R_{3(\text{Measured})}$ and $R_{1(\text{Measured})}$ corresponds to $R_{4\text{total}}$, $R_{2\text{total}}$, $R_{3\text{total}}$, and $R_{1\text{total}}$ respectively. For example if experimentally measured values of $R_{4\text{total}} = 15.494 \text{ K}\Omega$, $R_{2\text{total}} = 10.73 \text{ K}\Omega$, $R_{3\text{total}} = 11.43 \text{ K}\Omega$, and $R_{1\text{total}} = 8.7 \text{ K}\Omega$ are considered we need to solve the above simultaneous equations for obtaining actual values of individual resistors R_1 , R_2 , R_3 and R_4 .

In order to solve the simultaneous equations we assumed the initial true values of resistances of R_1 , R_2 , R_3 and R_4 as $R_1 = 1$, $R_2 = 1$, $R_3 = 1$, and $R_4 = 1$ respectively.

Therefore, we can write (in MathCAD):

$$\frac{1}{R_1} + \frac{1}{(R_2 + R_3 + R_4)} - \frac{1}{8.7 \cdot 1000} = 0$$

$$\frac{1}{R_2} + \frac{1}{R_1 + R_3 + R_4} - \frac{1}{10.73 \cdot 1000} = 0$$

$$\frac{1}{R_3} + \frac{1}{R_1 + R_2 + R_4} - \frac{1}{11.43 \cdot 1000} = 0$$

$$\frac{1}{R_4} + \frac{1}{R_1 + R_2 + R_3} - \frac{1}{15.494 \cdot 1000} = 0$$

Solving for these equations by (in MathCAD):

$$\begin{pmatrix} R_{1val} \\ R_{2val} \\ R_{3val} \\ R_{4val} \end{pmatrix} := \text{Find}(R_1, R_2, R_3, R_4)$$

We obtain the true resistance values of R_1 , R_2 , R_3 and R_4 as follows:

$$\begin{pmatrix} R_{1val} \\ R_{2val} \\ R_{3val} \\ R_{4val} \end{pmatrix} = \begin{pmatrix} 1.036 \times 10^4 \\ 1.359 \times 10^4 \\ 1.484 \times 10^4 \\ 2.58 \times 10^4 \end{pmatrix} \quad \Omega$$

APPENDIX E

PROCEDURE FOR PRESSURE SENSOR CHARACTERIZATION USING
LOAD-CELL
(DEVELOPED BY: SURAJ KUMAR PATIL)

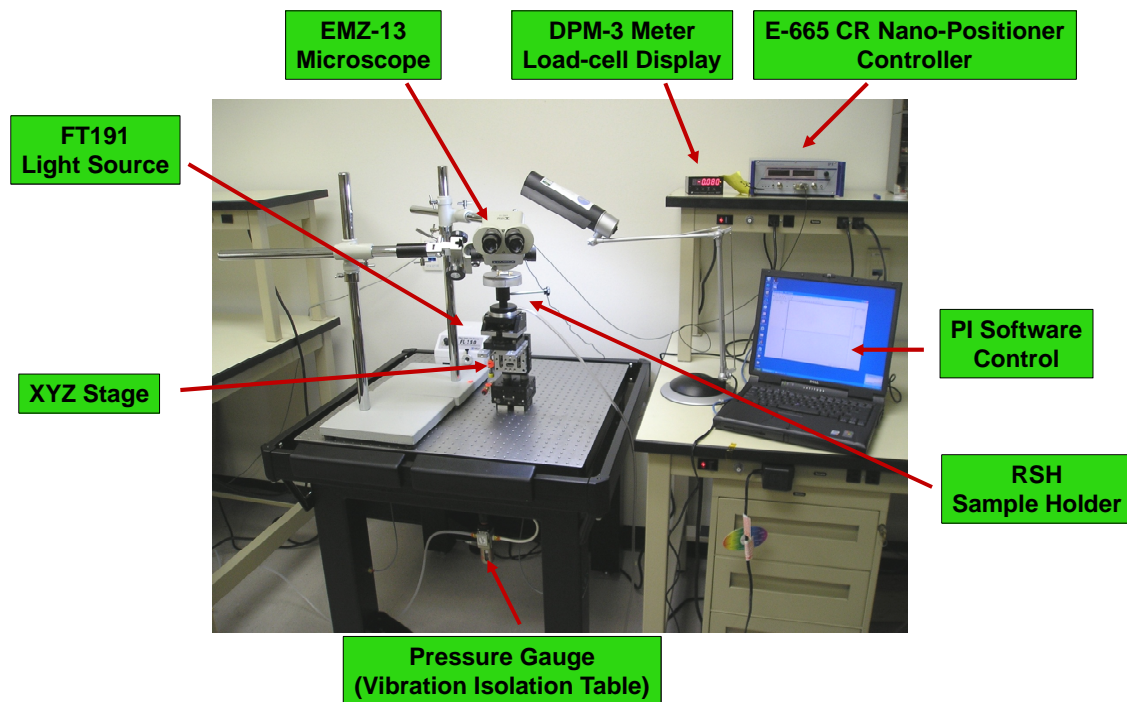


Figure E.1 Load-cell pressure sensor characterization set-up.

Operating Procedure

1. Check if the Jun-Air Pump is on AUTO mode. If not, turn the pump ON.
2. Check for pressure on the pressure gauge of the Vibration Isolation Table to be around 30-50 psi.
3. Check the probe if it is touching the sample. (* Lower the Z-stage if the probe is touching the sample). Move the probe to the safe distance, so the substrate chuck can be mounted on the MXT stage.
4. Turn ON the RSH (Substrate Holder) vacuum pump.
5. Power up the Load Cell, the DPM-3 meter should show some value when it turns ON. Let the Load cell stabilize for 2-5 minutes.
6. Press TARE/RST key on the front panel of the DPM-3. The reading should read 0.000/0.001. Wait for 15 minutes for the load cell to fully power up and stabilize.

7. Turn ON the E-665.CR Controller. Interface the controller with the host computer. By selecting the RS-232 interface.
8. PI Control software window pops up. Turn the SERVO-ON. Enter the command MOV A0.0.
9. Turn ON FT191, the light facilitates easy vision of the probe tip.
10. Move the TPI screws connected to the XYZ stage in order to make the sample closer to the probe tip and in required location.
11. Focus the EMZ-13 (microscope) till you see the sample and the probe tip in one plane.
12. Bring the sample closer to the probe tip. But **do not** let the probe tip touch the sample.
13. TARE/RST the DPM-3 meter. It displays 0.000/0.001.
14. Move slowly the Z-stage upwards and note for any reading change in the DPM-3 meter. (Do not move the stage too fast; it could overload the load cell). Remember to enter MOV A0.0, in order to obtain correct reading.
15. Once the probe tip is closer to sample, using Nanopositioner, make the tip touch the sample (as the probe tip touches the sample, there is sudden increase in load-cell reading). Note down the reading. The reading in DPM-3 meter is in grams.
16. Enter the MOV AX.X command as required for displacement. Note the change in load reading.
17. After the measurements are done. Enter command MOV A0.0.
18. Lower the sample, by lowering the XYZ stage.
19. Turn OFF the load cell. Turn OFF the E-665.CR.
20. Turn OFF the vacuum pump connected to RSH. Dismount the RSH from the XYZ stage and remove the sample.

Table E.1 Various components and their resolutions for load-cell set-up

Component	Model #	Company	Range	Resolution
<i>Load cell</i>	GS0-10	Transducer Techniques	0-10 gm (~0.098 N)	0.005 g (~0.00005 N)
Plug and Option with Connectors	Cal-TEDS	Transducer Techniques	Calibrated in grams	
Plug and Play meter	DPM-3	Transducer Techniques		
9-Pin Connector Adapter	DPM-3-AD9	Transducer Techniques		
Power Cord Assembly	DPM-3-PC6	Transducer Techniques		
<i>XYZ Micromanipulator Stage</i>				
Aluminum Plate Assembly	MX-PC	Siskiyou Design Instruments	1 inch	
Cross Roller Stage	100CR	Siskiyou Design Instruments		
Adjusting Screws	80TPI-1.0	Siskiyou Design Instruments		2.5 μ m
Adapter Block	MX-AB	Siskiyou Design Instruments		
Aluminum Spacer	AS-.500	Siskiyou Design Instruments		
Aluminum Base	AB-U	Siskiyou Design Instruments		
Building Block	BB-5.0	Siskiyou Design Instruments		
Rotary Platform Stage	RSX-2.0	Siskiyou Design Instruments	Full 360°	0.5°
Tilt Stage	MXT	Siskiyou Design Instruments	0-45°	0.008°
<i>Nano-Positioner</i>				
Positioner	P-620.ZCD	PI	50 μ m	0.2 nm (Closed Loop)
Adapter Plate	P-622K016	PI		
Controller	E-665.CR	PI	-20V to -120V	
<i>Probe Assembly</i>				
Probe Holder	74-600-0-xx	Micromanipulator		
Vacuum Pump	0322-v1	Micromanipulator		Noise 55 dBa
Wafer Holder	RSH/356V M-2	Micromanipulator		
<i>Microscope Assembly</i>				
Microscope	EMZ-13	Meiji Microscopes		

Table E.1 - continued

Component	Model #	Company	Range	Resolution
Auxiliary lens	MA507	Meiji Microscopes	1.5X	
Stand	S-4400	Meiji Microscopes		
Focusing Block	FS	Meiji Microscopes	150 W	
Dual pipe Light	FL191	Meiji Microscopes		
<i>Vibration Isolation Table</i>				
Vibration Isolation Table	LW3030B-250101NN0	Newport		

REFERENCES

- [1] R. L. Crabb, F. C. Treble, *Nature* (1967) 1223
- [2] C.R. Wronski, D.E. Carlson, R.E. Daniel, *Appl. Phys. Letts.* 29 (1976) 602
- [3] P.D. Plattner, W. W. Kruhler, W. Juergens, M. Moller, '80 Photovoltaic Solar Energy Conf. (1980) 121
- [4] H. Okinawa, K. Nakatani, M. Yano, M. Asano, K. Suzuki, *Jpn J appl. Phys.* 21 (1982) 239
- [5] T. P. Brody, *IEEE Trans. Electron Devices* 31 (1984) 1614
- [6] A. Constant, S. G. Burns, H. Shanks, C. Gruber, A. Landin, D. Schmidt, D. Thielen, F. Olympie, T. Schumacher, J. Cobbs, *Electrochem. Soc. Proc.* 94 (1995) 392
- [7] S. D. Theiss, S. Wagner, *IEEE Electron Dev. Lett.* 17 (1996) 578
- [8] N.D. Yang, G. Harkin, R. M. Bun, D. J. McCulloch, R. W. Wilks, A. G. Knapp, *IEEE Electron Dev. Lett.* 18 (1997) 19
- [9] P.M. Smith, P.G. Carey, T. W. Sigmon, *Appl. Phys. Lett.* 70 (1997) 342
- [10] W. S. Wong, A. Salleo, *Flexible Electronics: Materials & Applications*, Springer Science+Business Media, LLC, New York, NY -10013, USA, 2009
- [11] V. Cannella, M. Izu, S. Jones, S. Wagner, I.C. Cheng, *Inf. Display* (2005) 24
- [12] A. Plichta, A. Weber, A. Habek, S. Glas, *Mat. Res. Soc. Symp. Proc.* 769 (2003) H9.1
- [13] E.Y. Ma, S. Wagner, *Appl. Phys. Letts.* 74 (1999) 2661
- [4] T. Afentakis, M. Hatalis, A. T. Voutsas, J. Hartzell, *IEEE Trans. Electron. Dev.* 53 (2006) 815
- [5] A. Mahmood, Z. Çelik-Butler, D. P. Butler, *Sens. Actuators A* 132 (2006) 452
- [6] V. Shamanna, S. Das, Z. Çelik-Butler, D. P. Butler, K.L. Lawrence, *J. Micromech. Microengg.* 16 (2006) 1984

- [17] S. K. Patil, Z. Çelik-Butler, D. P. Butler, IEEE Trans. Nanotechnol. 9 (2010) 640
- [18] S. K. Clark, K. D. Wise, IEEE Trans. Electron. Dev. 12 (1979) 1187
- [19] J. Bergqvist, J. Gobert, J. Microelectromech. Sys. 3 (1994) 69
- [20] M. Royer, P. Holmen, M. Wurm, P. Aadland, M. Glenn, Sens. Actuat. A 4 (1983) 357
- [2] E. S. Kolesar, C. S. Dyson, J. Microelectromech. Sys. 4 (1995) 87
- [22] P. Schiller, D. L. Polla, M. Ghezzi, Tech. Digest IEEE Solid State Sens. Actuat. Workshop, Hilton head, SC USA (1990) 187.
- [23] D. Wagner, J. Frankenberger, P.P. Deimel, J. Micromech. Microeng. 4 (1994) 35
- [24] M. A. Chan, S. D. Collins, R. L. Smith, Sens. Actuat. A 43 (1994) 196
- [25] W. P. Eaton, "Surface Micromachined Pressure Sensors"- *Ph.D Dissertation*-University of New Mexico, Albuquerque, New Mexico, USA, May 1997
- [26] K. E. Petersen, F. Pourahmadi, J. Brown, P. Parsons, M. Skinner, J. Tudor, Dig. Tech. Papers , 1991 Intl. Conf. Solid State Sens. Actuators, Transducers (1991) 664
- [27] R. Schellin, G. Hess, Sens. Actuators A 32 (1992) 555
- [28] G. Li, "Piezoresistive Pressure Sensor With Integrated Amplifier Realized Using Metal-Induced Laterally Crystallized Polycrystalline Silicon" – *Ph.D Dissertation*- Hong Kong University of Science and Technology, Nov. 2004
- [29] S. M. Sze, Semiconductor Sensors, John Wiley & Sons, Inc., New York, USA 1994
- [30] O. J. Gregory, T. You, Proc. 2nd IEEE Sens. 2 (2003) 801
- [31] J. Thaysen, A.D. Yalcinkaya, R. K. Vestergaard, S. Jensen, M. W. Mortensen, P. Vettiger, A. Menon, Proc. 15th IEEE Intl. Conf. MEMS, Jan. 20-24, Las Vegas, NV, USA (2002) 320
- [32] M. Tamborin, S. Piccinini, M. Prudenziati, B. Morten, Sens. Actuators A 58 (1997) 159
- [33] H. Chiriac, M. Urse, F. Rusu, C. Hison, M. Neagu, Sens. Actuators A 76 (1999) 376
- [34] J. Engel, J. Chen, C. Liu, J. Micromech. Microengg. 13 (2003) 359
- [35] C. M. Wang, J. H. Hsieh, C. Li, Thin Solid Films 469/470 (2004) 455

- [36] J. Richter, O. Hansen, A. Nylandsted Larsen, J. Lundsgaard Hansen, G.F. Eriksen, E.V. Thomsen, *Sens. Actuators A* 123-124 (2005) 388
- [37] M. Yamamoto, N. Nawachi, T. Tsutsumoto, A. Terayama, *Diamond Relat. Mater.* 14 (2005) 657
- [38] W. D. Edwards, R. P. Beaulieu, *J. Sci. Instrum.* 2 (1969) 613
- [39] E. Peiner, A. Tibrewala, R. Bandorf, S. Biehl, H. Luthje, L. Doering, *Sens. Actuators A* 130-131 (2006) 75
- [40] R. He, P. Yang, *Nat. Nanotechnol. Letts.* 1 (2006) 42
- [41] C. S. Smith, *Phys. Review* 94 (1954) 42
- [42] P. J. French, A. G. R. Evans, *Solid State Electronics* 32 (1989) 1
- [43] M. Madou, *Fundamentals of Microfabrication: The Science of Miniaturization*, 2nd edition, CRC Press, March 2002.
- [44] S. K. Patil, Z. Çelik-Butler, D. P. Butler, *Ultramicroscopy* 110 (2010) 1154
- [45] http://www.ferroceramic.com/silicon_nitride.htm
- [46] Class Notes, MSE5345 – Ceramic Materials – University of Texas at Arlington, Fall 2010
- [47] P. Stiffert, E. Krimmel (Eds.), *Silicon – Evolution and Future of a Technology*, Springer-Verlag, Berlin, Heidelberg 2004
- [48] P. Reinig, B. Selle, F. Fenske, W. Fuhs, V. Alex, M. Birkholz, *J. Vac. Sci. Technol. A* 20 (2002) 2004
- [49] K. Xu, S. I. Shah, D. Guerin, *J. Vac. Sci. Technol. A* 19 (2001) 1078
- [50] K. Xu, M. M. Waite, S. I. Shah, *Mater. Sci. Eng. B* 108 (2004) 281
- [51] J. Shirafuji, H. Matsui, A. Narukawa, Y. Inuishi, *Appl. Phys. Lett.* 41 (1982) 535
- [52] Y. Mishima, M. Takei, T. Uematsu, N. Matsumoto, T. Kakehi, U. Wakino, M.Okabe, *J. Appl. Phys.* 78 (1995) 217
- [53] T. Ichikawa, US Patent No. 6022458, 8 Feb. 2000

- [54] Y. H. Jang, W. S. Park, M. Takeya, G. S. Jong, T. Ohmi, J. Electrochemical. Soc. 144 (1997) 3973
- [55] J. Joo, J. Vac. Sci. Technol. A 18 (2000) 2006
- [56] Y. Ishikawa, Y. Yamamoto, T. Hatayama, Y. Uraoka, T. Fuyuki, Solar Energy Matls. & Solar Cells 74 (2002) 255
- [57] A. van Zutphen, Ph.D Dissertation, Technische Universiteit Delft, The Netherlands (2001)
- [58] C. Malhaire, D. Barbier, Thin Solid Films 427 (2003) 362.
- [59] L. Cao, T. S. Kim, S. C. Mantell, D.L. Polla, Sens. Actuators A 80 (2000) 273
- [60] K. H. -L. Chau, C. D. Fung, P. R. Harris, G. A. Dahrooge, Electron Dev. Meet. Intl. Tech. Dig., Dec. 8-11, Washington, DC, USA (1991) 761
- [61] E. Obermeir, P. Kopystnski, Sens. Actuators A 30 (1992) 149
- [62] B. Caussat, J. P. couderec, A. Figueras, A. Vander Lee, J. Durand, V. Paillard, E. Shied, J. R. Morante, Solid State Phenomenon 67 (1999) 125
- [63] S. Veprek, V. Marecek, Solid State Electron. 11 (1998) 683
- [64] M. Le Berre, M. Lemiti, D. Barbier, P. Pinard, J. Cali, E. Bustarret, J. Sicart, J. L. Robert, Sens. Actuators A 46/47 (1995) 166
- [65] A. Stoffel, A. Kovács, W. Kronast, B. Müller, J. Micromech. Microeng. 6 (1996) 1
- [66] J. D. Gu, P. L. Chen, Thin Solid Films 498 (2006) 2
- [67] S. Ferrero, P. Mandracci, G. Cicero, F. Giorgis, C. F. Pirri, G. Barucca, Thin Solid Films 383 (2001) 181
- [68] J. K. Rath, A. J. Hardeman, C.H. M. van der Werf, P. A. T. T. van Veenendaal, M. Y. S. Rusche, R. E. I. Schropp, Thin Solid Films (2003) 67
- [69] N. S. Kale, S. Nag, R. Pinto, V. R. Rao, Proc. 8th IEEE NANO Conf. (2008) 460
- [70] S.-C. Yang, H. Suematsu, W. Jiang, K. Yatsui, IEEE Trans. Plasma Sci. 30 (2002) 1816

- [71] W. Jiang, S. Kitayama, T. Suzuki, K. Yatsui, Pulsed Power Plasma Sci. (2001) 376
- [72] V. Shamanna, "Design, Simulation and Fabrication of Piezoresistive Pressure Sensors on Flexible Substrates"- *M.S Thesis* - University of Texas at Arlington, Arlington, Texas USA, December 2005
- [73] Y. Komem, I. W. Hall, J. Appl. Phys. 52 (1981) 6655
- [74] D. Sands, G. Williams, P. H. Key, Semicond. Sci. Technol. 12 (1997) 750
- [75] P. M. Smith, P. G. Carey, T. W. Sigmon, Appl. Phys. Letts. 70 (1997) 342
- [76] C. Yi, S. -W. Rhee, J. -H Ju, S.- K. Yim, H. Min, J. Mater. Sci.: Mater. Electron. 12 (2001) 697
- [77] Y. C. Peng, G.S. Fu, W. Yu, S. Q. Li, Y. L. Wang, Semicond. Sci. Technol. 19 (2004) 759
- [78] R. S. Sposili, J. S. Im, Appl. Phys. Letts. 69 (1996) 2864
- [79] T. Voustas, Low Temp. Polysilicon Tech. for Advanced Display Systems, 51, Sharp Microelec. Tech. Inc., 1997
- [80] G. Ekanayake, H.S. Reehal, Vacuum 81 (2006) 272
- [81] O. Nast, A. J. Hartmann, J. Appl. Phys. 88 (2000) 716
- [82] M. S. Haque, H. A. Naseem, W. D. Brown, J. Appl. Phys. 75 (1994) 3928
- [83] <http://learningandteaching.unsw.edu.au/content/creative/cdp/matSci/phase6a.htm>
- [84] L. Hultman, A. Robertsson, H. T. G. Hentzell, I. Engstrom, P. A. Psaras, J. Appl. Phys. 62 (1987) 3647
- [85] J. S. Maa, S.J. Lin, Thin Solid Films, 64 (1979) 63
- [86] B. Bian, J. Yie, B. Li, Z. Wu, J. Appl. Phys. 73 (1993) 7402
- [87] S. F. Gong, H. T. G. Hentzell, A. E. Robertsson, L. Hultman, S. E. Hornstrom, G. Radnoczi, J. Appl. Phys. 62 (1987) 3726
- [88] S. W. Russell, L. Jian, J. W. Mayer, J. Appl. Phys. 70 (1991) 5153

- [89] S. Y. Yoon, K. Ki Hyung, K. Chae Ok, O. Jae Young, J. Jin, J. Appl. Phys. 82 (1997) 5865
- [90] O. Nast, *Ph.D Dissertation*, Philipps – Universitat Marburg, 2000
- [91] M.S. Ashtikar, G. L. Sharma, J. Appl. Phys. 78 (1995) 913
- [92] C. Hayzelden, J. L. Batstone, J. Appl. Phys. 73 (1993) 8279
- [93] L. H. Allen, J. W. Mayer, K. N. Tu, L. C. Feldman, Phys. Rev. B 41 (1990) 8213
- [94] T. J. Konno, R. Sinclair, Matl. Sci. Engg. A 179 (1994) 426
- [95] F. A. Trumbore, J. Bell Sys. Tech. 39 (1960) 205
- [96] S.M. Sze, Physics of Semiconductor Devices, 2 ed. Wiley & Sons, New York, USA 1981
- [97] K. N. Tu, Appl. Phys. Lett. 27 (1975) 221
- [98] Z. M. Zhang, J. Y. Wang, L. P. H. Jeurgens, E. J. Mittemeijer, Phys. Rev. B 77 (2008) 045424-1
- [99] A. Hiraki, J. Electrochem. Soc. 127 (1980) 2662
- [100] Z. M. Zhang, J. Y. Wang, L. P. H. Jeurgens, E. J. Mittemeijer, Phys. Rev. Letts. 100 (2008) 125503-1.
- [101] D. He, J. Y. Wang, E. J. Mittemeijer, J. Appl. Phys. A 80 (2005) 501
- [102] J.O. McCaldin, H. Sankur, Appl. Phys. Letts. 19 (1971) 524
- [103] D. A. Porter, K. E. Easterling, M. H. Sherif, Phase Transformations in Metals and Alloys, 3rd ed., CRC press, 2009
- [104] E. P. Donovan, F. Spaepen, D. Turnbull, J. M. Pate, D. C. Jacobson, Appl. Phys. Lett. 42 (1983) 698
- [105] F. Spaepen, Philos. Mag. 30 (1974)
- [106] G. J. van Grup, J. Appl. Phys. 44 (1973) 2040

- [107] S. Gall, J. Schneider, J. Klein, K. Hubener, M. Muske, B. Rau, E. Conrad, I. Seiber, K. Petter, K. Lips, M. Stoger-Pollach, P. Schattschneider, W. Fuhs, Thin Solid Films 511-512 (2006) 7
- [108] D. Dimova-Malinovska, O. Angelov, M. Sendova-Vassileva, M. Kamenova, J.-C. Pivin, Thin Solid Films 451-452 (2004) 303
- [109] O. Nast, S. R. Wenham, J Appl. Phys 88 (1) (2000) 124
- [110] J. Klein, J. Schneider, M. Muske, S. Gall, W. Fuhs, 19th European PVSE Conf. (2004) Paris, France.
- [111] G. Ekanayake, T. Quinn, H. S. Reehal, J Crystl. Grwth. 293 (2006) 351.
- [112] J. Schneider, A. Schneider, A. Sarikov, J. Klein, M. Muske, S. Gall, W. Fuhs, J Non-Crystl. Solids 352 (2006) 972
- [113] D. Dimova-Malinovska, V. Grigorov, M. Nikolaeva-Dimitrova, O. Angelov, N. Peev, Thin Solid Films 501 (2006) 358
- [114] B.D. Cullity, S. R. Stock, Elements of X-ray Diffraction, 3rd ed. Prentice Hall (2001)
- [115] Y. Matsumoto, Z. Yu, Jpn. J. Appl. Phys. 40 (2001) 2110
- [116] A. Sarikov, J. Schneider, J. Klein, M. Muske, S. Gall, W. Fuhs, Silicon Photovoltaics, Annual Report 2005- Hahn-Meitner- Institut, 68
- [117] S. K. Patil, Z. Çelik-Butler, D. P. Butler, Thin Solid Films 519 (2010) 479
- [118] B. J. Kane, M. R. Cutkosky, G. T. A. Kovacs, Sens. Actuators A 54 (1996) 511
- [119] B. J. Kane, M. R. Cutkosky, G. T. A. Kovacs, J. Microelectromech. Sys. 9 (4) (2000) 425
- [120] L. Wang, D. J. Beebe, IEEE Trans. Biomed. Engg. 49 (11) (2002) 1340
- [121] P. Valdastri, S. Roccella, L. Beccai, E. Cattin, A. Menciassi, M. C. Carrozza, P. Dario, Sensors Actuators A 123-124 (2005) 249
- [122] A. Wisitsoraat, V. Patthanasetakul, T. Lomas, A. Tuantranont, Sensors Actuators A 139 (2007) 17

- [123] C. -S. Park, J. Park, D.-W. Lee, *Microelectron. Engg.* 86 (2009) 1250
- [124] G. Kaupp, *Atomic Force Microscopy, Scanning Nearfield Optical Microscopy and Nanoscratching: Application to Rough and Natural Surfaces*, Springer, Berlin, 2006
- [125] M. Sakai, *Principles and Applications of Indentation*, in: F. Yang, J.C. M. Li (Eds.), *Micro and Nano Mechanical Testing of Materials and Devices*, Springer, New York, 2008, 1-47
- [126] C. B. Prater, P. G. Maivald, K. J. Kjoller, M. G. Heaton, *Probing Nano-Scale Forces with Atomic Force Microscope: Application Note*, www.veeco.com
- [127] C.S. Hodges, *Adv. Colloid. And Interf. Sci.* 99 (2002) 13
- [128] M. Torotonese, *IEEE Engg. in Med. and Biol. Mag.* 16 (2) (1997) 28
- [129] <http://www.veecoprobes.com/c-29-contact.aspx>
- [130] NovaScan Technologies Inc., 131 Main Street, Ames, Iowa 50010, U.S.A, Tel: 1 800-303-1265, www.novascan.com
- [131] J. P. Cleveland, S. Manne, D. Bocek, P.K. Hansma, *Rev. Sci. Instrum.* 64(2) (1993) 403
- [132] B. Ohler, *Practical Advice on the Determination of Cantilever Spring Constants: Application Note*, www.veeco.com
- [133] M. R. Vanlandingham, S. H. McKnight, G. R. Palmese, R. F. Eduljee, J. W. Gillespie, Jr., R. L. McCulough, *J. Mat. Sci. Letts.* 16 (1997) 117
- [134] R. Proksch, *Nondestructive Added Mass Spring Calibration with the MFD-3D™: Technical Note*, www.asylumresearch.com
- [135] W. Han, *Force Spectroscopy with the Atomic Force Microscope: Application Note*, www.agilent.com
- [136] A. Daire, *Low-Voltage Measurement Techniques: Application Note*, www.keithley.com
- [137] M. Vila, D. Cáceres, C. Prieto, *J. Appl. Phys.* 94 (2003) 7868
- [138] L. Lin, H. -C. Chu, Y. -W. Lu, *IEEE/ASME J. MEMS* 8 (1999) 514
- [139] L. Lin, W. Yun, *IEEE Aerospace Conf.* (1998) 429

- [140] H. C. Lim, B. Schulkin, M. J. Pulickal, S. Liu, R. Petrova, G. Thomas, S. Wagner, K. Sidhu, J. F. Federici, *Sens. Actuators A* 119 (2005) 332
- [141] Y. Zhang, B. Liu, L. Liu, Z. Tan, Z. Zhang, H. Lin, T. Ren, *IEEE Asian Solid State Ckts. Conf.* (2006) 443
- [142] S. Chen, M. -Q. Zhu, B. -H. Ma, W. -Z. Yuan, *3rd IEEE Intl. Conf. Nano/Micro Engineered and Molecular Sys.* (2008) 351
- [143] K. Saejok, B. P. E. Chaowicharat, E. Ratanaudomphisut, O. Treethaveesak, C. Hruanun, A. Poyai, *5th IEEE Intl. Conf. ECTI-CON* (2008) 813
- [144] X. Liu, X. Lu, R. Chuai, C. Shi, C. Suo, *Sens. Actuators A* 154 (2009) 42

BIOGRAPHICAL INFORMATION

Suraj Kumar Patil received his B.E in electronics and communication engineering from Bangalore University, India, in 2000 and M.S degree in electrical engineering from University of Texas at Arlington, Texas, U.S.A in December 2003. He received his Ph.D degree in materials science and engineering from University of Texas at Arlington, Texas, U.S.A in December 2010. He has been associated with Microsensors Lab and NanoFAB Research and Teaching Facility Center at University of Texas at Arlington, Texas since Fall 2004. During the course of his research he has first-authored 3 Journal Publications, and 1 Conference Proceeding including 3 Conference Presentations. He has one U.S Patent (Pending). His current research interests include design and fabrication of sensors and actuators on flexible substrates, novel semiconductor device development, fuel cells, nanomaterials and their characterization techniques.